TRACING ON-AXIS DIFFUSE FLUIDS BY CHALCOPHILE ELEMENTS DISTRIBUTION IN UPPER OCEANIC CRUST AT PITO DEEP, EAST PACIFIC RISE

by

Zhu Tian

M.Sc., China University of Geosciences (Beijing), 2013
B.Sc., China University of Geosciences (Beijing), 2006

A Thesis Submitted in Partial Fulfillment
of the Requirements for the Degree of

MASTER OF SCIENCE

in the School of Earth and Ocean Sciences

© Zhu Tian, 2016
University of Victoria

All rights reserved. This thesis may not be reproduced in whole or in part, by photocopy or other means, without the permission of the author.

Supervisory Committee

TRACING ON-AXIS DIFFUSE FLUIDS BY CHALCOPHILE ELEMENTS DISTRIBUTION IN UPPER OCEANIC CRUST AT PITO DEEP, EAST PACIFIC RISE

by

Zhu Tian
M.Sc., China University of Geosciences (Beijing), 2013
B.Sc., China University of Geosciences (Beijing), 2006

Supervisory Committee

Dr. Laurence Coogan, (School of Earth and Ocean Sciences)
Supervisor

Dr. Dante Canil, (School of Earth and Ocean Sciences)
Departmental Member

Dr. Kathryn Gillis, (School of Earth and Ocean Sciences)
Departmental Member

Dr. Frank van Veggel, (Department of Chemistry)
Outside Member

Abstract

Supervisory Committee
Dr. Laurence Coogan, (School of Earth and Ocean Sciences)
Supervisor
Dr. Dante Canil, (School of Earth and Ocean Sciences)
Departmental Member
Dr. Kathryn Gillis, (School of Earth and Ocean Sciences)
Departmental Member
Dr. Frank van Veggel, (Department of Chemistry)
Outside Member

Mid-ocean ridge hydrothermal systems play an important role in the cycling of energy and mass between the solid earth and oceans. The on-axis low-temperature diffuse fluids (temperature lower than ~100 °C) carry ~90% of the on-axis heat fluxes, but diffuse fluids generation is poorly constrained. This study uses the abundance of the chalcophile elements, which form metal-sulphides in the rock record, to test models for diffuse fluids generation. These include mixing between seawater and high-temperature hydrothermal fluids and conductive cooling of high-temperature hydrothermal fluids.

This thesis determined the concentrations of the elements of interest (As, Mo, Ag, Cd, Sn, and Tl) in geological reference materials using standard addition method in ICP-MS. These values were used to calibrate the analysis of samples from Pito Deep to trace the abundance of these elements within the upper oceanic crust. The results show that the Zn, Cu, As, Ag, Cd, Tl, and Pb are generally depleted in sheeted dikes and enriched in the lava unit and/or the transition zone, which is consistent with previous studies on fast-spreading EPR crust at Hole 504B, Hess Deep and Hole 1256D. The enrichment of these elements in the lava unit and/or the transition zone suggests that cooling high-temperature hydrothermal fluids to form diffuse fluids occurred in this

area of the oceanic crust. Molybdenum and Sb are added into all units of the crust by recharging seawater. The concentrations of chalcophile elements in diffuse fluids were calculated by a mass balance. The results of this study favored a diffuse fluids generation model that involves mixing of seawater and high-temperature hydrothermal fluids. Results also show that the observed concentrations of Mo and Sb requires extra input source besides recharging seawater and oceanic crust, possibly particulates in seawater.

Table of Contents

Supervisory Committee ..... **ii**
Abstract ..... **iii**
Table of Contents ..... **v**
List of Tables ..... **vii**
List of Figures ..... **viii**
Acknowledgments ..... **xiv**
Dedication ..... **xv**
1. INTRODUCTION **1**
1.1. Mid-Ocean Ridge Hydrothermal Systems 1
1.2. On-axis Diffuse Hydrothermal Circulation 3
1.2.1. Fluid mixing model 4
1.2.2. Conductive heating model 5
1.2.3. Conductive cooling model 6
1.3. The Geological Record of the Generation of Diffuse fluids 6
1.4. Geochemistry of Chalcophile Elements in Metal-Sulphides in Hydrothermal Systems 9
1.4.1. Solubility of metal-sulphide minerals in hydrothermal systems 9
1.4.2. Tracing the chalcophile elements in metal-sulphides 13
1.4.3. Tracing diffuse fluids generation using the chalcophile elements 17
1.5. Thesis Objectives and Structure 19
2. ANALYTICAL METHOD DEVELOPMENT **21**
2.1. Isotopes and Potential Interferences for the Elements to be Analyzed in the Reference Materials **22**
2.2. Standard Addition Method **24**
2.2.1. Principles of analysis using standard addition 24
2.2.2. Single element solutions preparation 26
2.2.3. Spike solution preparation 26
2.3. Instrument Settings and Analytical Run Conditions **28**
2.3.1. Basic Principles of Collision/Reaction Cell 28
2.4. Data Reduction **29**
2.5. Concentration of Selected Chalcophile Elements in Reference Materials 34
2.5.1. Interference correction factors from analysis of single element solutions 34
2.5.2. Chalcophile element compositions in the reference materials 38
2.5.3. Detection limits 50
3. STUDY AREA AND SAMPLE SUITE **51**
3.1. Tectonic Setting and Previous Studies at Pito Deep **51**
3.1.1. Previous studies metal sulphides and the distribution of Cu, Zn and Pb in Pito Deep 55
3.1.2. Previous studies on the fault zone in Area A 56
3.2. Sample Selection and Description **58**

4. RESULTS AND DISCUSSION 62
4.1. Sample Analysis and Data Reduction 63
4.2. The Bulk Rock Compositions of Interest 65
4.2.1. Assessment of fresh basalt composition and the change of concentration in Pito Deep samples 65
4.2.2. The distribution of the elements of interest in Pito Deep 66
4.3. Sulphide Precipitation in a Fault Zone 87
4.4. Summary 92
5. CONCLUSIONS AND FUTURE WORK 94
5.1. Distribution Profiles of the Elements of Interest in the Upper Crust of the Pito Deep 95
5.2. Diffuse Fluid Generation in the Upper Crust of Pito Deep 100
5.2.1. A plausible model of diffuse fluid generation in the Pito Deep crust 100
5.2.2. Calculating the concentrations of the elements of interest in diffuse fluids 104
5.2.3. Model robustness and uncertainties 110
5.3. Conclusion 111
5.4. Future Work 113
Bibliography 117
Appendix A: Analysis Sequence for Standard Addition Method 140
Appendix B: Analytical Raw Data and Data Reduction of Standard Addition Method 141
Appendix C: Description of Samples and Reference Materials Preparation 142
Appendix D: Data Reduction Processes of the Pito Deep Samples 143
Appendix E: Assessment of ICP-MS Data Accuracy 146
Appendix F: Analytical Results of Pito Deep Samples and Previous Data on Other Fast-Spreading Ridges 148

List of Tables

Table 1.1. Published concentrations of elements of interest in diffuse fluids at EPR 21°N and Guaymas Basin. 8
Table 1.2. Concentration (ppm) of the elements of interest in chalcopyrite, pyrite, sphalerite and galena from sulphide ore deposits (Fleischer, 1955). Data from all types of ore deposits, not limited to mafic-hosted deposits. 15
Table 1.3. Median concentration (ppm) of the elements of interest in chalcopyrite, pyrite, sphalerite from oceanic crust at ODP Hole 1256D (Patten et al., 2016). 15
Table 2.1. Reference materials used in this study 21
Table 2.2. Element abundance chart showing the isotopes of interest in this study. Orange cells: atomic mass; green cells: elements of interest; numbers in white cells: isotopic abundance (%). 23
Table 2.3. Polyatomic interferences on the isotopes of interest 24
Table 2.4. Concentrations of single element solutions used to identify interferences and develop corrections. 26
Table 2.5. Concentration of stock solution. 27
Table 2.6. Concentration of working spike solutions. 28
Table 2.7. Operating parameters used during ICPMS analyses in this study 28
Table 2.8. Interference correction factor (in percentage) for Ag in reference material 35
Table 2.9. Selected chalcophile elements composition (ppm) in reference materials achieved by spike calibration. 49
Table 4.1. Precision (2σ) and limit of detection (LOD) in this study. 64
Table 4.2. Concentrations of the elements of interest in seawater and hydrothermal fluids. 73
Table 4.3. Enrichment and depletion of the elements of interest in lavas, transition zone samples, fault zone samples (wall-rock dikes and fault breccias). Empty cells represent no change comparing the MORB glasses with uncertainties. 77
Table 5.1. Median values* of the elements of interest changes in the upper crust of Pito Deep. 97
Table 5.2. Calculation of the concentrations of the elements of interest in high-temperature hydrothermal fluids (C^X_{HF}) and diffuse fluids (C^X_{DS}) generated by fluid mixing in Pito Deep. 108
Table 5.3. Calculation of the concentrations of the elements of interest in high-temperature hydrothermal fluids (C^X_{DF}) and diffuse fluids (C^X_{DS}) generated by conductive cooling of high-temperature hydrothermal fluids in Pito Deep. 109

List of Figures

Figure 1.1. Schematic model for hydrothermal circulation within the upper crust at intermediate- to fast-spreading ridges. Seawater percolates downward to the oceanic crust, where seawater is heated by an underlying magma body (heat source) near the base of sheeted complex. The fluid undergoes chemical modifications through reaction with the host rock as temperature elevated. At the maximum temperature (> 400 °C), the fluids become buoyant and rise back to the seafloor forming "black smoker" and/or diffuse fluids. Modified from Alt (1995) and Coogan (2008). 3
Figure 1.2. Two models of seafloor hydrothermal circulation generating diffuse fluids. (A) Mixing of high-temperature fluids with shallow recharged seawater. (B) Mineral precipitation forming an impermeable barrier resulting in no, or only partial, mixing of high-temperature fluids, conductively heated seawater and cooling high-temperature fluids. Some changes in the fluid composition are depicted in (A). For example, seawater brings Mg, K, and SO_4^{2-} into the crust, and takes in Ca, Si and some trace metals (e.g. Cu, Zn, Ag and Pb, etc.) from rocks while evolving at elevated temperature. Modified from Lowell et al., 2003. 5
Figure 1.3. Spidergram of the composition of the high-temperature hydrothermal fluid (HF) (n=9) from fast-spreading ridges normalized to seawater (SW). The compiled concentrations of the elements of interest range from different vents, with the blue lines represent the range of the HF/SW ratio. The orange line represents the mean value of HF/SW. The concentrations of Pb, Zn, Cu, Co, Ge, Ga, Ag, Cd, Tl, As, and Sb in hydrothermal fluids are higher than in seawater, and the concentration Mo in hydrothermal fluids are lower than in seawater. Data of the composition of hydrothermal fluids end member are from Von Damm et al. (1985), Von Damm (1990 and 1995), Edmond et al. (1979b), Trefry et al. (1994), and Metz and Trefry (2000). Data of the composition of seawater are from Bruland (1983) and Donat and Bruland (1995).....8
Figure 1.4. (A) Experimentally determined solubilities of chalcopyrite (near horizontal contours) and sphalerite (near vertical contours) in 1 M Cl fluids with their oxygen fugacity buffered by pyrite-pyrrhotite-magnetite (a moderately reducing environment) as a function of pH (in-situ) and temperature. The green and pink paths represent the paths followed during fluid mixing and conductive cooling respectively (Janecky and Seyfried, 1984). The red solid circle represents the concentrations of Cu and Zn in high-temperature hydrothermal fluids (Von Damm, 1990 and 1995; Edmond et al., 1979b; Trefry et al., 1994). (B) Different temperature windows for chalcopyrite ($CuFeS_2$) and sphalerite (ZnS) precipitation from the fluids. The fluids conditions (pH, Cl content, S content, and SO_4/H_2S ratio) used in the experiment are given in the figure. Solubilities of chalcopyrite decrease from 100 ppm to below 1 ppm when the temperature of fluids drops from about 350 °C to 270°C. The solubility of sphalerite decrease from 100 ppm to 1 ppm when the temperature of fluids decreases from 250 °C to about 175 °C. (C) The solubilities of chalcopyrite and sphalerite controlled by pH of the fluids at a temperature of 300 °C. The sharper decreasing of solubility of sphalerite than that of chalcopyrite with pH value increase indicates that

the solubility of sphalerite is more dependent on pH than that of chalcopyrite. The dashed lines indicate the precipitation windows for chalcopyrite and sphalerite. Modified from Large (1992) and Janecky and Seyfried (1984). 12
Figure 1.5. Calculated stoichiometric solubilities of copper sulphides together with various common sulphides in a 3 molal sodium chloride solution with a pH of 5 at elevated temperatures. The solubilities depicted above are regarded as minimal approximations of the true mineral solubilities. Modified from Helgeson (1969).....13
Figure 1.6. Cartoons of predicted chalcophile elements distribution in upper oceanic crust for end-member models. Purple-coloured bars represent bulk permeabilities (in log scale) within upper oceanic crust determined for Hole 504B (Fisher, 1998). Assuming high-temperature hydrothermal fluids mobilize certain amount (-Δ) of a chalcophile element, these amount of element will all be carried to the seafloor forming high-temperature fluid vents if no diffuse fluids were generated during the upwelling (Profile A). Profile B, C, and D show the distribution of chalcophile elements while forming diffuse fluids and precipitating all of the element within the crust. Profile B represents the chalcophile elements that precipitate in both the lava unit and the transition zone. For chalcophile elements like Cu, of which the solubility is highly temperature sensitive, the precipitation zone will be largely in the transition zone if this is where mixing starts (Profile C). Profile D represents the chalcophile elements with solubilities that are less temperature sensitive, which only start precipitating in the lava section. 19
Figure 2.1. An example of the standard addition method showing experimental data points and the extrapolated linear regression line, which intercepts the y-axis at C_0. The concentration in the standard solution (C_{std}) = -C_0.....25
Figure 2.2. A typical collision cell instrument. Adapted from Thomas, 2001.....29
Figure 2.3. Regression line for the signals at ^{91}Zr (represent the interference source $^{91}Zr^{16}O^+$ on ^{107}Ag) and ^{107}Ag analyzed in Zr single element solutions. The interference corrected ^{107}Ag signal is subtracting 0.0061 times of the ^{91}Zr signal (x in the plot) from the signal of mass 107. 33
Figure 2.4. Histograms showing interference corrections as a proportion of the total count rate on the elements of interest in CRC and standard mode. (A): signal at mass 107 in standard mode; (B): signal at mass 107 in CRC mode; (C): signal at mass 109 in standard mode; (D): signal at mass 109 in CRC mode; (E): signal at mass 95 in standard mode; (F): signal at mass 95 in CRC mode; (G): signal at mass 110 in standard mode; (H): signal at mass 110 in CRC mode; (I): signal at mass 111 in standard mode; (J): signal at mass 111 in CRC mode; (K): signal at mass 75 in standard mode (note the compressed scale in this part). Negative values in (G), (I), and (J) represent that effectively all of the signal from the element of interest is coming from the interferences. Note variable y-axis scales. See text for details.....37
Figure 2.5. Standard addition calibration curves of ^{75}As in standard mode of the standards: (A) AGV-1; (B) BHVO-2; (C) BIR-1; (D) DNC-1; (E) JG-2; (F) JGb-1; (G) BCR-2.....39
Figure 2.6. Standard addition calibration curves of ^{95}Mo in standard mode in the six reference materials. (A) AGV-1 in standard mode; (B) BHVO-2 in standard mode; (C) BIR-1 in standard mode; (D) DNC-1 in standard mode; (E) JG-2 in standard mode; (F) JGb-1 in standard mode. 40

Figure 2.7. Standard addition calibration curves of ^{109}Ag in CRC mode of the standards: (a) AGV-1; (b) BHVO-2; (c) BIR-1; (d) DNC-1; (e) JG-2; (f) JGb-1; (g) BCR-2.....41
Figure 2.8. Standard addition calibration curves of ^{111}Cd in CRC mode of the standards: (A) AGV-1; (B) BHVO-2; (C) BIR-1; (D) DNC-1; (E) JG-2; (F) JGb-1; (G) BCR-2.....42
Figure 2.9. Standard addition calibration curves of ^{117}Sn and ^{118}Sn in both CRC and standard modes. (A) ^{117}Sn of AGV-1 in standard mode; (B) ^{117}Sn of AGV-1 in CRC mode; (C) ^{118}Sn of AGV-1 in standard mode; (D) ^{118}Sn of AGV-1 in CRC mode; (e) ^{117}Sn of BHVO-2 in standard mode; (F) ^{117}Sn of BHVO-2 in CRC mode; (G) ^{118}Sn of BHVO-2 in standard mode; (H) ^{118}Sn of BHVO-2 in CRC mode; (I) ^{117}Sn of BIR-1 in standard mode; (J) ^{117}Sn of BIR-1 in CRC mode; (K) ^{118}Sn of BIR-1 in standard mode; (L) ^{118}Sn of BIR-1 in CRC mode; (M) ^{117}Sn of DNC-1 in standard mode; (N) ^{117}Sn of DNC-1 in CRC mode; (O) ^{118}Sn of DNC-1 in standard mode; (P) ^{118}Sn of DNC-1 in CRC mode; (Q) ^{117}Sn of JG-2 in standard mode; (R) ^{117}Sn of JG-2 in CRC mode; (S) ^{118}Sn of JG-2 in standard mode; (T) ^{118}Sn of JG-2 in CRC mode; (U) ^{117}Sn of JGb-1 in standard mode; (V) ^{117}Sn of JGb-1 in CRC mode; (W) ^{118}Sn of JGb-1 in standard mode; (X) ^{118}Sn of JGb-1 in CRC mode; (Y) ^{117}Sn of BCR-2 in standard mode; (Z) ^{117}Sn of BCR-2 in CRC mode; (AA) ^{118}Sn of BCR-2 in standard mode; (AB) ^{118}Sn of BCR-2 in CRC mode. The calibration curves for JG-2 (Q-T) all show the offset of the sample without spike from the curves, which is probably resulted from contamination during sample preparation.....46
Figure 2.10. Standard addition calibration curves of ^{205}Tl in both CRC and standard modes in the seven reference materials. (A) AGV-1 in standard mode; (B) AGV-1 in CRC mode; (C) BHVO-2 in standard mode; (D) BHVO-2 in CRC mode; (E) BIR-1 in standard mode; (F) BIR-1 in CRC mode; (G) DNC-1 in standard mode; (H) DNC-1 in CRC mode; (I) JG-2 in standard mode; (J) JG-2 in CRC mode; (K) JGb-1 in standard mode; (L) JGb-1 in CRC mode; (M) BCR-2 in standard mode; (N) BCR-2 in CRC mode. The inset plots in (I) and (J) are the zoom-in plots for the calibration lines. Even though the extrapolation of the intercepts of AGV-1, standard mode and CRC gave the results of 1860 ppb and 1859 ppb, which means that the result is precise for calibrating the unknown samples. 48
Figure 3.1. (A) The Pito Deep Rift (PDR) is located close to the Southern East Pacific Rise (SEPR). (B) 3-D bathymetry of the PDR showing the locations of the two sampling regions Area A and B. The Pito Deep (deep blue area in centre) is more than 6 km deep, and bounded by rift walls. Modified after Hayman and Karson (2009). .52
Figure 3.2. Jason II and Alvin dive tracks from research cruise AT11-23 of the R/V Atlantis in February 2005 in study areas Area A (A) and Area B (B) showing colour coded lithologic boundaries (Karson et al., 2005). Jason II dives begin with J2, followed by the lowering number and transect number. Alvin dives are numbered sequentially as only one transect was completed for each dive. Depths are meters below sea level (mbsl); contour intervals are 200m. Adapted from Heft et al., 2008. 53
Figure 3.3. Geologic map and side scan sonar image of the Alvin Dive 4078 area in X and Y axis (modified from Hayman and Karson, 2009). The fault zone represented by the shaded area has a prominent "main fault" (red line). The fault zone cuts across the

sheeted dike complex (SDC, blue) and the transition zone (TZ, green) at a depth of between ~3500 mbsl and ~3700 mbsl. 58
Figure 3.4. (A)-(C): Zn, Cu, and Pb concentrations (ppm) versus Y (ppm) for fresh MORB glasses (Jenner and O'Neil, 2012; solid blue squares) and Pito Deep samples (samples selected for this study: solid red circles; not selected: solid grey circles). The data for Zn, Cu, Pb are from Pollock et al. (2009), Heft et al. (2008), Barker et al. (2008), and Barker et al. (2010a). In fresh MORB glasses, Pb and Zn have positive correlation with Y, whereas Cu shows negative correlation with Y. This is because that Cu is more incompatible than Pb and Zn (Wang and Becker, 2015). (D) $^{87}Sr/^{86}Sr$ versus the depth below the lava-dike transition (m) for Pito Deep samples in the fault zone studied (samples selected for this study: red solid diamonds are wall-rock dikes from the fault zone, and red open diamonds are the fault breccias; not selected: grey solid diamonds are wall-rock dikes from the fault zone, and black open diamonds are the fault breccias). Note that there are nine fault zone samples selected for this study but only seven of them have previously been analyzed for $^{87}Sr/^{86}Sr$. The green shaded area in (D) represents the $^{87}Sr/^{86}Sr$ for the background dikes in Pito Deep. Sr-isotope data are from Barker et al. (2010a). 61
Figure 4.1. A-D: Cobalt, gallium, germanium, and tin concentrations (ppm) versus Yb (ppm) in Pito Deep samples (this study) compared with basalt glasses (Jenner and O'Neil, 2012; grey squares). Magmatic differentiation trends are defined by the element versus Yb trends in the glass that are fit to a power law curve (line and equation shown in each plot). Cobalt (A), germanium (C), gallium (B), and tin (D) show either no change or a slight depletion compared with MORB glass. Blue shaded area represents the previously published Pito Deep data from Heft et al. (2008), Barker et al. (2008), and Barker et al. (2010a). 69
Figure 4.2. Bulk rock Ge concentration (ppm) versus Ga (ppm) in glass samples (Jenner and O'Neill, 2012; grey open squares) and the Pito Deep samples. These two elements behave similarly and do not partitioning into sulphide minerals during in hydrothermal processes. 70
Figure 4.3. Correlations between the elements of interest and sulphur content in Pito Deep samples. None of the element concentration correlates with sulphur content. Sulphur content data is from Barker et al., 2010b. 72
Figure 4.4. A-G: Zinc, copper, arsenic, silver, cadmium, lead, and thallium concentrations (ppm) versus Yb (ppm) in Pito Deep samples (this study) compared with MORB glasses (Jenner and O'Neill, 2012; grey squares). Magmatic differentiation trends are defined by the element versus Yb trends in the glass that are fit to a power law curve (line and equation shown in each plot). The blue shaded areas are the data reported by previous studies (Heft et al., 2008; Barker et al., 2008; Barker et al., 2010a). H is a zoom-in of G. 76
Figure 4.5. The concentrations of Zn, Cu, Ga, and Pb change with depth below lava-dike transition zone in Pito Deep (this study; Heft et al., 2008; Barker et al., 2008; and Barker et al., 2010a), 504B (Alt and Emmermann, 1985; Alt et al., 1989; and Bach et al., 2003), Hess Deep (Gillis et al., 2001; and Stewart et al., 2002), and 1256D (Cooper, 2007; Gao et al., 2009). Due to the lack of full element suite, the changing of the concentrations of Zn, Cu, Ga and Pb comparing with fresh MORB glasses is not calculated for 504B, Hess Deep, and 1256D. All data could be found in Appendix F. All

four areas show Zn and Cu depletion in dikes and enrichment in the transition zone, and also show Pb depletion in dikes and enrichment in the lavas and the transition zone. There is little change of Ga concentration with depth in four areas. 78
Figure 4.6. A-G: Change of the concentrations of Zn, Cu, As, Ag, Cd, and Pb as a function of depth relative to the lava-dike transition zone. The grey shaded area in each plot is the uncertainty in the MORB glass composition (Jenner and O'Neill, 2012). The changes with depths show all enrichments occur in the transition zone and lava unit, whereas the concentrations of these elements in the sheeted dike complex shows no systematic change with depth.....81
Figure 4.7. Concentration of Tl in the samples from the Pito Deep (red solid circles) and samples from Hole 504B (empty squares; Nielsen et al., 2006) as a function of depth relative to the lava-dike transition zone. Figure B is a zoom-in plot of figure A. Both locations show the same profile of depletion in dikes and enrichment of Tl in lavas.....82
Figure 4.8. A and B: Thallium concentrations versus Cs concentrations of samples from Hole 504B (Nielsen et al., 2006), and the Pito Deep (this study). B is a zoom-in plot for A. Thallium show little correlations with Cs, indicating thallium uptake is not a result of low-temperature alteration. 82
Figure 4.9. Cadmium concentration versus Tl concentration of samples (exclude one lava sample with high Tl concentration from Area A and samples from the fault zone) from the Pito Deep. Solid blue line represents the Cd/Tl ratio of seawater. Thallium and Cd have a fair correlation, which indicates the abundance of Tl is controlled by the same parameters control Cd abundance in the Pito Deep.....83
Figure 4.10. Molybdenum (A) and antimony (B) concentrations in Pito Deep compared with MORB glasses. The change of the concentrations of Mo and Sb as a function of depth beneath the lava-dike transition zone (C and D). The grey shaded area is the uncertainty in the MORB glass composition (Jenner and O'Neill, 2012)..85
Figure 4.11. Plot of Mo and Sb in Pito Deep samples and MORB glass (Jenner and O'Neill, 2012). The dike samples show strong positive correlation between the concentration (ppm) of Mo and Sb, indicating the area of seawater alteration process. 86
Figure 4.12. A: strong positive correlation between Sb and Mo concentrations in the Pito Deep dike samples. B: positive correlation between the concentrations of Sb and As in the Pito Deep lavas, transition zone samples, two samples of the dikes, and fault zone samples. 86
Figure 4.13. Concentrations of Mo (A) and Sb (C) versus Rb. Molybdenum and Sb show no linear correlations with Rb in the Pito Deep. Plot B is zoom-in for plot A, and D is zoom-in for plot C.....87
Figure 4.14. Composition changes versus lateral distance cross fault zone in Area A. The distances cross fault zone are represented by the lateral coordinates of samples. Grey shaded areas are the uncertainties in the MORB glasses composition. Green shaded area represents for the $^{87}Sr/^{86}Sr$ values of the background dikes from Pito Deep. "FZ" represents fault zone. Arrows in B and D represent a fault breccia sample with higher values of enrichment in Cu and Zn than the scale. A: $^{87}Sr/^{86}Sr$ in fault breccia samples are higher than in the wall-rock dike samples; B-K: changes of Zn, As, Cu, Cd, Ag, Pb, Tl, Mo, Sb and Sn concentration compared with MORB glass across the

fault zone. $^{87}Sr/^{86}Sr$ values of Pito Deep background dikes are from Barker et al. (2008), and the $^{87}Sr/^{86}Sr$ values of fault breccias from Pito Deep are from Barker et al. (2010a).....90

Figure 5.1. Cartoon profiles of the changes of the elements of interest against depths comparing to MORB glasses in Pito Deep. The thickness of sheeted dike complex (2h) is twice as the lava unit and the transition zone (h). Zero value in all profiles means no change. Pink- and blue-shaded areas represent enrichment and depletion of the element compared to MORB glass respectively. A: enrichment in the lavas ($+ \mathbf{2}\Delta$) is about twice of the depletion in dikes ($- \Delta$), representing no net loss from the crust. B: enrichment over two times ($+> \mathbf{2}\Delta$) in lavas and transition zone of the depletion in dikes ($- \Delta$). C: enrichment in the transition zone. D: enrichment in almost all the samples in the upper crust, and the enrichment of the element reaches a peak at a certain depth in the dikes. E: enrichment in almost all the samples in the upper crust. Enrichment in dikes at a certain depth, and equally enriched in lavas and the transition zone.....99

Figure 5.2. Schematic diagram of models for the generation of diffuse fluid. The deep-recharged seawater is heated up during hydrothermal circulation forming high-temperature hydrothermal fluids. A: fluid mixing model for diffuse fluids generation. The dashed line represents the un-mixed part of the high-temperature hydrothermal fluids. If the high-temperature hydrothermal fluids were thoroughly mixed into diffuse fluids, the model would only follow the solid lines. B: conductive cooling of high-temperature hydrothermal fluids for diffuse fluids generation. The dashed line represents the part of high-temperature hydrothermal fluids that are not cooled into diffuse fluids. If all high-temperature hydrothermal fluids were all conductively cooled to form diffuse fluids, the model would only follow the solid lines. 101

Acknowledgments

I sincerely thank my supervisor Dr. Laurence Coogan who gave me this research opportunity and continuous support. In our countless useful discussions, Laurence's patient guidance and valuable advice have helped me throughout the duration of my studies. I could not have complete this thesis without him.

Special thanks go to Dr. Jody Spence for all the help in conducting ICP-MS analyses and for all the advice on analytical method development. Jody makes the lab a safe place to operate with all the hazardous acids, and he makes it a delightful experience for me.

I also thank Armaghan Attar and Mina Seyedali for being such trusted colleagues and generous friends. They have kept me sane during my master's studies, or at least as sane as they are.

My thanks to Yue Fang for standing by me and giving me the most needed support to my life. He makes it possible for me to work late and has dinner already on the table when I get home, not to mention his sacrifices of numerous vacations because he refuses to go without me at his side. To Yue, thank you.

Being away from home, the unconditional support from my parents matters more than ever to me. They are the source of my joy and motivation, and no words could express my gratitude to them.

Dedication

For my parents,

Jialing Xu and Xinhua Tian

Chapter 1

1. INTRODUCTION

1.1. Mid-Ocean Ridge Hydrothermal Systems

Approximately 60% of the Earth's surface is covered by oceanic crust (Cogley, 1984) that is created at divergent plate boundaries called mid-ocean ridges or spreading centers. Hydrothermal circulation occurs along these global spreading-centers that extend over ~60,000 km. These mid-ocean ridge hydrothermal systems play an important role in the cycling of energy and mass between the solid earth and the oceans (e.g. German and Seyfried, 2014; Alt, 1995; Edmond et al., 1979a). Seawater penetrates through permeable and porous oceanic crust along mid-ocean ridges, and it flows downward into the crust (Fig. 1.1). The downwelling fluids evolve with their temperature elevated by an underlying heat source and they undergo chemical modifications through reaction with the crust as they move downward (Mottl, 1983a). The fluids achieve a condition of maximum buoyancy and rise up to the seafloor as high-temperature hydrothermal fluids (Fig. 1.1).

The buoyant high-temperature (>400 °C) fluids generated deep in the crust rise to the seafloor and some fraction of the fluid exits into the ocean with little modification (Seyfried et al., 1991; Cann et al., 1985). When these high-temperature fluids meet with the cold (~2°C) bottom seawater, phases such as iron oxides and sulphides are precipitated, generating columns of black smoke, which gives the name "black smoker" to these vents (Haymon, 1983; Fig. 1.1). Some metal precipitation occurs close to the seafloor building sulphide-rich chimney structures.

Studies on the chemistry of the focused high-temperature hydrothermal fluids

show that many elements are exchanged between the fluids and basaltic rocks during hydrothermal circulation (e.g., Von Damm, 1995). For example, Mg and sulfate are removed from fluids, whereas elements such as Ca, Si, Fe and Mn are extracted from rock through dissolution and exchange reactions (e.g., Butterfield et al., 1997; Mottl, 1983a; Seyfried et al., 1988; Seyfried and Bischoff, 1979; Von Damm et al., 1985). Vent fluids are moderately reducing, with the presence of H_2S, H_2, CH_4, and significant amounts of Fe^{2+} and Mn^{2+}. Compared to seawater, high-temperature fluids are enriched in many elements such as Cu, Zn, As, Ag, Cd, Sb, Tl, and Pb and are generally depleted in elements like Mg, Mo and U (e.g., Seyfried et al., 2003; Von Damm et al., 1985; Von Damm, 1995 and 2000; Nielson et al., 2006; Metz and Trefry, 2000; Trefry et al., 1994).

Heat flux measurements suggest that only a small fraction of the total hydrothermal heat flux close to ridge axis is discharged through high-temperature vents; the larger fraction of the heat flux is released by much lower temperature (up to ~100°C) diffuse flow exiting the seafloor (Rona and Trivett, 1992; Schultz et al., 1992; Baker et al., 1993; Ramondenc et al., 2006; Nielsen et al., 2006; Mittelstaedt et al., 2012; Larson et al., 2015; Germanovich et al., 2015). With the on-axis (crust age less than 1 Ma) heat fluxes dominated by diffuse fluids, the quantification of chemical fluxes from diffuse vents is important for estimating global hydrothermal fluxes, and in turn, understanding the controls on ocean composition.

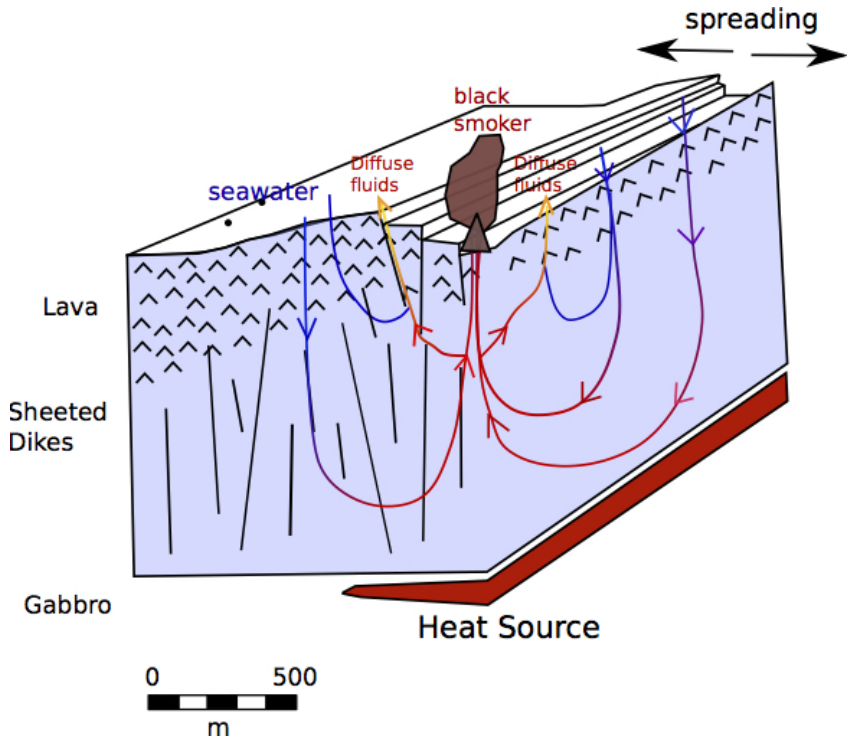

Figure 1.1. Schematic model for hydrothermal circulation within the upper crust at intermediate- to fast-spreading ridges. Seawater percolates downward to the oceanic crust, where seawater is heated by an underlying magma body (heat source) near the base of sheeted complex. The fluid undergoes chemical modifications through reaction with the host rock as temperature elevated. At the maximum temperature (> 400 ℃), the fluids become buoyant and rise back to the seafloor forming "black smoker" and/or diffuse fluids. Modified from Alt (1995) and Coogan (2008).

1.2. On-axis Diffuse Hydrothermal Circulation

Diffuse flow vents, discovered at the Galapagos Spreading Center in 1977, were the first type of hydrothermal activity studied along the global mid-ocean ridge system (Edmond et al., 1979a, 1979b). Because of the moderate temperature and chemical composition providing energy sources for chemosynthesis (they contain hydrogen sulphide and other reduced chemical compounds), diffuse flow sites support a great variety of fauna and microbial mats (e.g., Tunnicliffe, 1991; Shank et al., 1998; Shock and Holland, 2004; Bach et al., 2004). Diffuse fluids are formed by either the mixing of high-temperature fluids with seawater in the subsurface, and/or

conductive heating of seawater, and/or conductive cooling of hydrothermal fluids (Cooper et al., 2000; Kelley et al., 2002; Lowell et al., 2008; Foustoukos et al., 2009). These processes and the interactions of these fluids with the upper oceanic crust control the chemistry of diffuse fluids (Crowell et al., 2008; Foustoukos et al., 2009).

1.2.1. Fluid mixing model

A theoretical fluid mixing model for the generation of diffuse fluids was proposed by Lowell et al. (2003) (Fig. 1.2 A). The model suggests that the mixing of hot fluids and "shallow recharged" seawater generates the diffuse fluids. Diffuse fluids generated by subseafloor mixing of seawater and hydrothermal fluids can be thought of as dilution of high-temperature fluids, with mixing leading to a decreasing temperature, increasing pH, and commonly changes in chloride content. With these parameters changing, the solubilities of metal-sulphides in hydrothermal fluids decrease, thus metal-sulphides are expected to precipitate in the mixing zone (Fig. 1.2 A).

Diffuse fluids generated by fluid mixing have a different compositional character to high-temperature fluids. For example, Mg and sulfate concentrations are increased by mixing high-temperature hydrothermal fluids with seawater, and the concentrations of Mn, Fe, Cu, Zn are decreased due to both a dilution effect and the precipitation of sulfide and/or oxide minerals (Edmond et al., 1979a; Bowers et al., 1985). Some elements (e.g., Cu, U, and REE excluding Ce) even show depletions in diffuse fluids relative to ambient seawater due to subseafloor precipitation (Edmond et al., 1979b; Wheat et al., 2002).

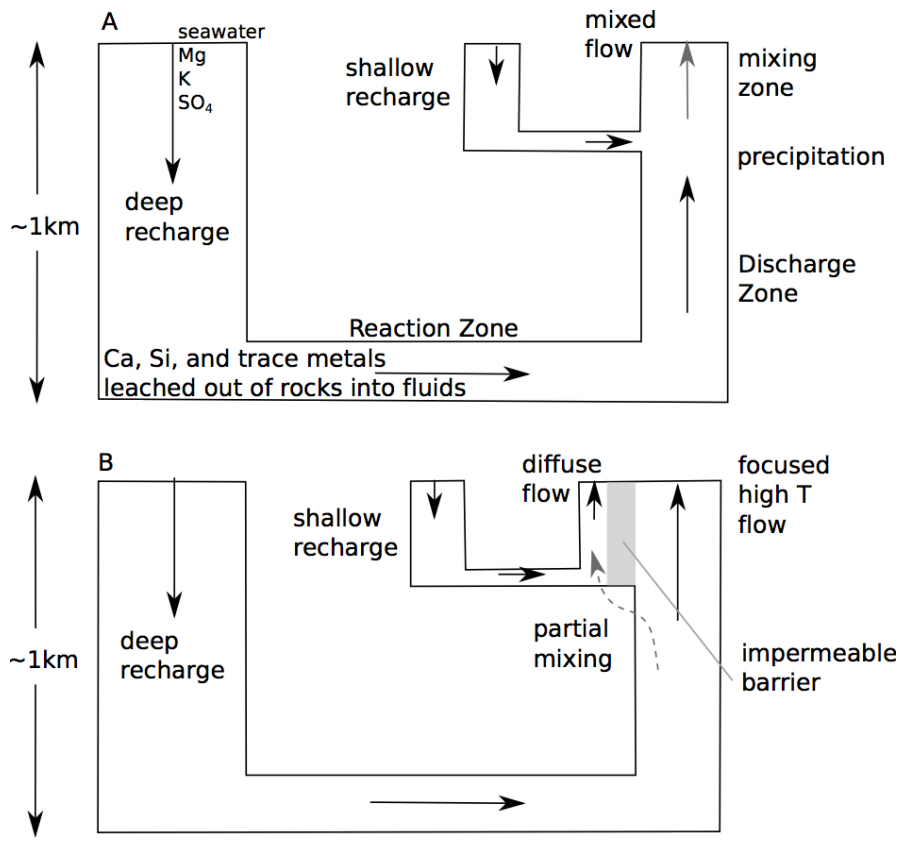

Figure 1.2. Two models of seafloor hydrothermal circulation generating diffuse fluids. (A) Mixing of high-temperature fluids with shallow recharged seawater. (B) Mineral precipitation forming an impermeable barrier resulting in no, or only partial, mixing of high-temperature fluids, conductively heated seawater and cooling high-temperature fluids. Some changes in the fluid composition are depicted in (A). For example, seawater brings Mg, K, and SO_4^{2-} into the crust, and takes in Ca, Si and some trace metals (e.g. Cu, Zn, Ag and Pb, etc.) from rocks while evolving at elevated temperature. Modified from Lowell et al., 2003.

1.2.2. Conductive heating model

The conductive heating model for generating diffuse fluids is shown in Figure 1.2 B, where high-temperature fluids conductively heat seawater within the crust near the axis (Cooper et al., 2000; Lowell et al., 2003). The minerals precipitated (e.g., silica precipitated from high-temperature fluids, anhydrite precipitated when seawater heated to >120 °C) change the permeability of the crust by forming impermeable

barriers (Fig. 1.2 B; Fournier, 1985; Martin and Lowell, 2000; Sleep, 1991; Lowell and Yao, 2002; Lowell et al., 2003). In the study by Cooper et al. (2000), they used $^{87}Sr/^{86}Sr$ and Li to trace the formation of diffuse fluids at the Lucky Strike. Cooper et al. (2000) concluded that the conductive heating of seawater is the dominant mechanism of generating diffuse fluids at the Lucky Strike site, and the conductively heated seawater does not make a significant contribution to the chemical fluxes. Conductive heating of seawater does not directly influence hydrothermal chemical fluxes into the ocean. However, conductive heating of seawater requires conductive cooling of high-temperature hydrothermal fluids, and during cooling process, mineral precipitation may occur changing the composition of hydrothermal fluids.

1.2.3. Conductive cooling model

Evidence for conductive cooling of hydrothermal fluids was presented by Foustoukos et al. (2009), where they discussed the compositional differences between the conductive cooling hydrothermal fluids and high-temperature fluids at the Main Endeavour Field (MEF; on the Juan de Fuca Ridge). They discovered that the relatively lower temperature fluids possess compositional characteristics, such as low Mg concentration, and SiO_2 virtually identical to the high-temperature fluids. The results indicated that the fluids underwent conductive cooling processed to generate diffuse fluids.

1.3. The Geological Record of the Generation of Diffuse fluids

Just as the composition of diffuse fluid should record the processes involved in

their generation so should the geochemistry of the upper oceanic crust. To trace the formation of diffuse fluids, this study uses the approach of investigating the chemistry of the oceanic crust. Previous studies of hydrothermal sulphide mineralization showed that as hydrothermal fluids cool, sulphide precipitation occurs initially in the subsurface forming a network of sulphide veins (e.g. the "stockwork zone" at the Trans-Atlantic Geotraverse (TAG) sulphide mound or "stockwork-like zone" in Hole 504B; e.g., Honnorez et al., 1983; Fouquet et al., 1998; Hannington et al., 1998). Stockwork zones consist of minerals like pyrite, sphalerite, chalcopyrite, and galena (Honnorez et al., 1983; Hannington et al., 1998). Studies of the chemistry of stockwork zones show enrichment of Cu, Zn, As, Mo, and $\delta^{34}S$ (Honnorez et al., 1983; Hannington et al., 1998).

According to the difference in the composition of the elements of interest in high-temperature hydrothermal fluids and that of seawater (Fig. 1.3), Pb, Zn, Cu, Ge, Ga, Ag, Co, Cd, Tl, As, and Sb are leached from the crust into the hydrothermal fluids, and Mo is expected to be added to the crust. Therefore, the source of the metals precipitated in stockwork (or stockwork-like) zones is from deeper in the crust. Previous studies of hydrothermal systems showed that Cu, Zn, Pb, and S are leached from sheeted dikes and carried by hydrothermal fluids into the transition zone and lavas forming sulphide precipitation zones (e.g., Alt et al., 1995; Gillis et al., 2001; Zoeller, 2014). However, there is limited data of the concentrations of these elements in diffuse fluids (Table 1.1). Diffuse fluids are generated during mixing that can lead to the precipitation of sulphides, therefore, tracing the chemistry of sulphide precipitation in the crust will help us to understand the generation of diffuse fluids.

Table 1.1. Published concentrations of elements of interest in diffuse fluids at EPR 21°N and Guaymas Basin.

Location	Sample ID	T °C	Zn µ	Ag n	Cd n	Pb n	As n
SW	ALV0980-05-06	30	11	-	-	-	-
	ALV0980-07-08	84	289	-	-	-	-
	ALV0980-07-08	84	289	-	-	-	-
	ALV0980-09-10	112	-	-	-	-	-
	ALV0981-03-04	110	31	-	-	-	-
GEH9	ALV1177-09	100	3	-	-	-	-
	ALV1177-15	100	11	3	27	448	146
	LLU0111-008-GEH9-1982	100	21	-	-	-	-

Note: data from Von Damm, 1983. µ: micromoles/kg; n: nanomoles/kg; the elements not analyzed are shown as dashed lines (-).
SW: EPR 21°N Southwest; GEH9: Guaymas East Hill vent area 9.

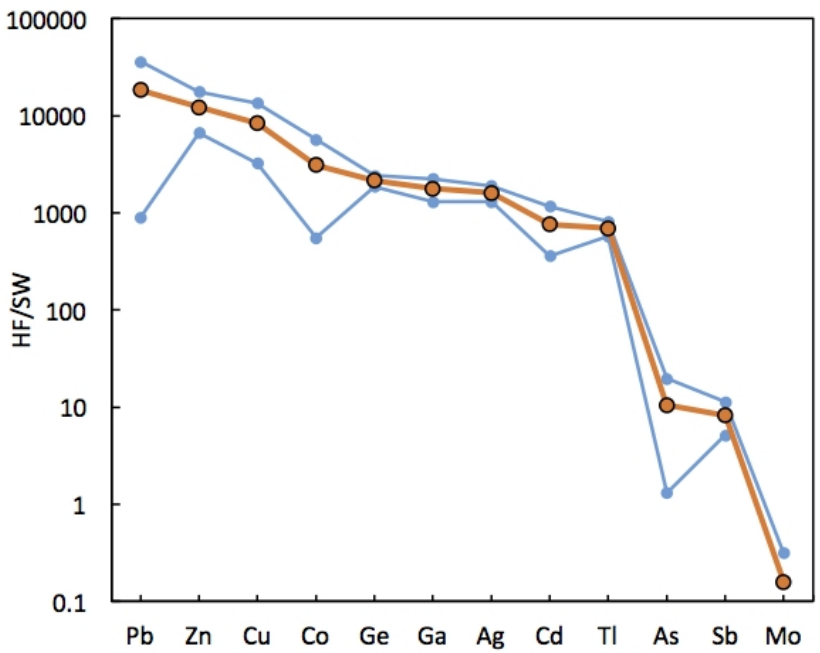

Figure 1.3. Spidergram of the composition of the high-temperature hydrothermal fluid (HF) (n=9) from fast-spreading ridges normalized to seawater (SW). The compiled concentrations of the elements of interest range from different vents, with the blue lines represent the range of the HF/SW ratio. The orange line represents the mean value of HF/SW. The concentrations of Pb, Zn, Cu, Co, Ge, Ga, Ag, Cd, Tl, As, and Sb in hydrothermal fluids are higher than in seawater, and the concentration Mo in hydrothermal fluids are lower than in seawater. Data of the composition of hydrothermal fluids end member are from Von Damm et al. (1985), Von Damm (1990 and 1995), Edmond et al. (1979b), Trefry et al. (1994), and Metz and Trefry (2000). Data of the composition of seawater are from Bruland (1983) and Donat and Bruland (1995).

1.4. Geochemistry of Chalcophile Elements in Metal-Sulphides in Hydrothermal Systems

Chalcophile elements Cu, Zn, As, Ag, Cd, Tl, and Pb precipitate as sulphides, and/or substitute into metal-sulphides, because of the change in fluid's temperature, pH values, and chloride content. Perhaps the most important difference between diffuse and high-temperature hydrothermal fluids in controlling their geochemistry is temperature. The temperature of diffuse fluids is typically lower than 100°C. Temperature is a key factor controlling the solubility of Cu, Zn, and Fe sulphides and associated trace metals in hydrothermal systems (Seewald and Seyfried, 1990; Seyfried and Ding, 1993; Mottl et al., 1979; Haymon and Kastner, 1981). The most common metal-sulphide minerals in mid-ocean ridge hydrothermal deposits are pyrite (FeS_2), chalcopyrite ($CuFeS_2$), and sphalerite (ZnS), together with minor amount of galena (PbS), marcasite (FeS_2), covellite (CuS), chalcocite (Cu_2S) and pyrrhotite ($Fe_{1-x}S$) (Hayman, 1983; Mosier et al., 1983; Hannington, 2014). Understanding the controlling parameters on the solubility of metal-sulphide minerals in hydrothermal fluids is important if the distribution of chalcophile elements in upper oceanic crust is to be used to track diffuse fluid formation.

1.4.1. Solubility of metal-sulphide minerals in hydrothermal systems

Experimental results indicated that as hydrothermal fluids cool, Cu and Fe will precipitate out of the fluid before Zn (e.g., Seewald and Seyfried, 1990). This agrees with other laboratory and field studies, which show that the solubility of chalcopyrite

decreases sharply at temperature below 350°C (e.g., Seyfried and Ding, 1995), whereas the precipitation of sphalerite is normally observed below 250°C (Janecky and Seyfried, 1984) (Fig. 1.4). Sphalerite precipitation is driven dominantly by an increase in pH (Fig. 1.4) (e.g., Bourcier and Barnes, 1987). High-temperature (> 300 °C) hydrothermal fluids commonly contain 0.6-2.6 ppm Cu and 9.7-37 ppm Zn (Von Damm, 1990 and 1995; Edmond et al., 1979b; Trefry et al., 1994), which is more consistent with the composition predicted by a fluid mixing model than a conductive cooling model (Fig. 1.4 A). The hydrothermal fluids from natural system may have different fluid conditions (e.g., Cl content, oxygen fugacity) from the experimental studies (Fig 1.4), which is the reason that the high-temperature hydrothermal fluids concentrations of Cu and Zn fall within the area of > 200°C rather than > 300°C in Figure 1.4 A.

If high-temperature hydrothermal fluids mix with seawater, the temperature of hydrothermal fluids will decrease and the pH will increase, which causes chalcopyrite and sphalerite precipitation together (Fig. 1.4 A). However, if hydrothermal fluids conductively cool, the temperature of fluids will decrease but the pH value will not increase. Instead, the precipitation of metal-sulphide (e.g., chalcopyrite) will generate H^+ which causes the pH to decrease (Equation 1.1).

$$M^{2+} + H_2S = MS + 2H^+ \qquad \textit{Equation 1.1}$$

where M is the metal-element of interest which precipitates as a metal-sulphide. In this conductive cooling model, the lower pH of the fluids may inhibit sphalerite while chalcopyrite will precipitate due to cooling (Hannington, 2014). This study does not consider the thermodynamic process of reducing H^+ activity when fluid temperature

decreases.

The reducing degree of acidity by decreasing fluid temperature due to thermodynamic effect is much lower than the increasing degree of acidity generated by metal-sulphide precipitation.

Calculated solubilities of various individual sulfides showed that chalcocite, covellite, pyrite, sphalerite and galena solubilities are all temperature dependent up to 300°C in a 3 molal NaCl fluids at a pH of 5 (Fig. 1.5, Helgeson,1969). However, the solubility of pyrrhotite (labeled FeS in Fig. 1.5) shows little or no variation with temperature in this solution. The solubilities of these metal-sulphides indicate that if high-temperature hydrothermal fluids carry Cu, Fe, Zn, and Pb, and the temperature decreases into the range of 0-200°C, co-precipitation of metal-sulphides (chalcopyrite, pyrite, sphalerite, galena, chalcocite and covellite) will occur.

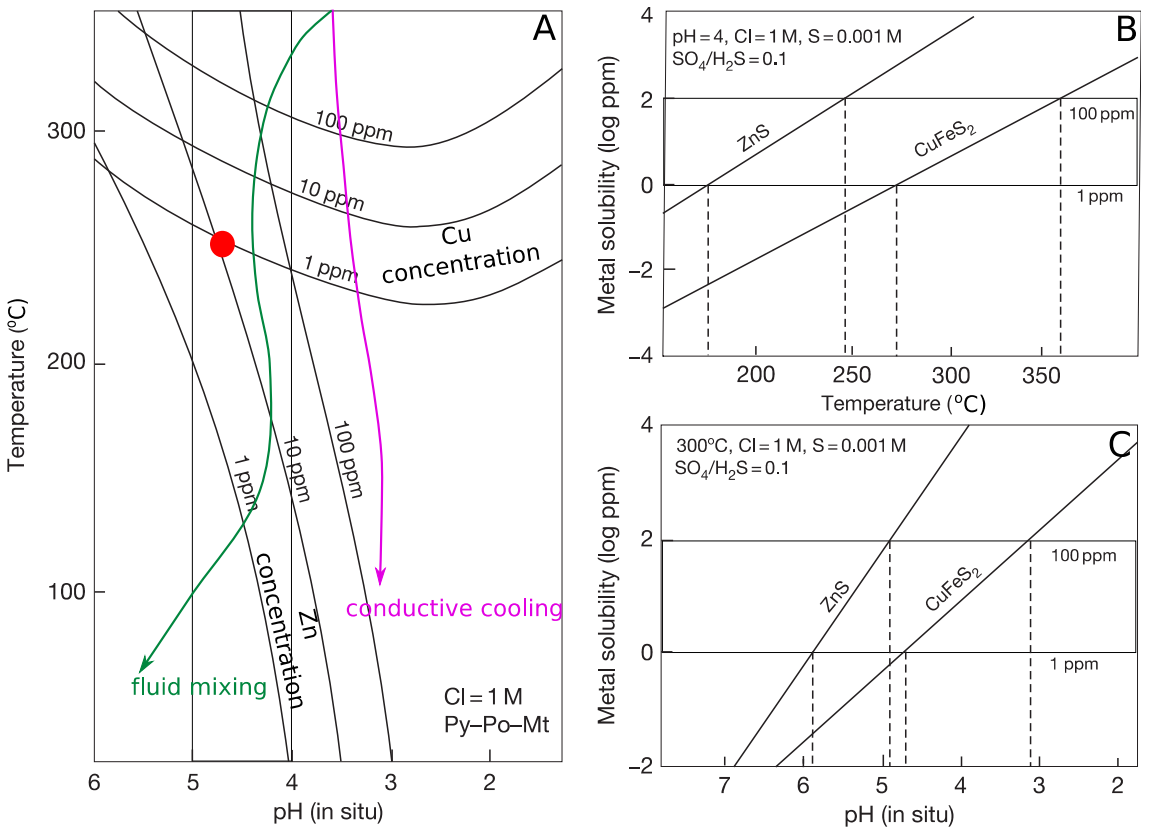

Figure 1.4. (A) Experimentally determined solubilities of chalcopyrite (near horizontal contours) and sphalerite (near vertical contours) in 1 M Cl fluids with their oxygen fugacity buffered by pyrite-pyrrhotite-magnetite (a moderately reducing environment) as a function of pH (in-situ) and temperature. The green and pink paths represent the paths followed during fluid mixing and conductive cooling respectively (Janecky and Seyfried, 1984). The red solid circle represents the concentrations of Cu and Zn in high-temperature hydrothermal fluids (Von Damm, 1990 and 1995; Edmond et al., 1979b; Trefry et al., 1994). (B) Different temperature windows for chalcopyrite ($CuFeS_2$) and sphalerite (ZnS) precipitation from the fluids. The fluids conditions (pH, Cl content, S content, and SO_4/H_2S ratio) used in the experiment are given in the figure. Solubilities of chalcopyrite decrease from 100 ppm to below 1 ppm when the temperature of fluids drops from about 350 °C to 270°C. The solubility of sphalerite decrease from 100 ppm to 1 ppm when the temperature of fluids decreases from 250 °C to about 175 °C. (C) The solubilities of chalcopyrite and sphalerite controlled by pH of the fluids at a temperature of 300 °C. The sharper decreasing of solubility of sphalerite than that of chalcopyrite with pH value increase indicates that the solubility of sphalerite is more dependent on pH than that of chalcopyrite. The dashed lines indicate the precipitation windows for chalcopyrite and sphalerite. Modified from Large (1992) and Janecky and Seyfried (1984).

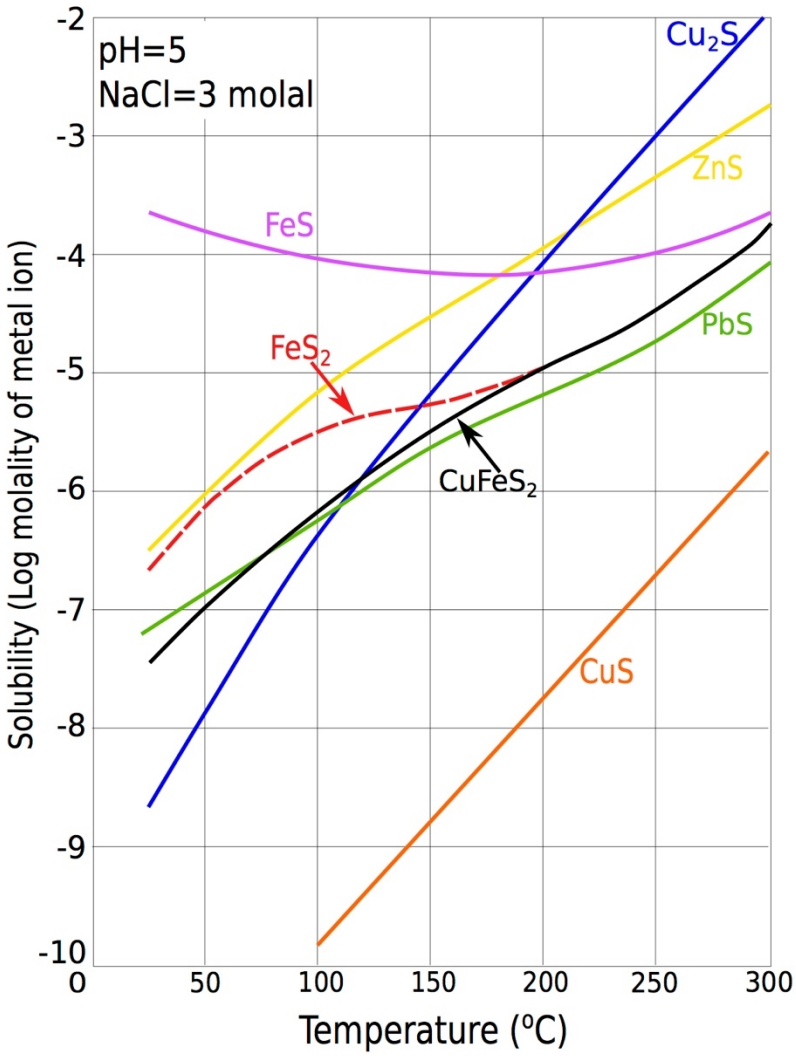

Figure 1.5. Calculated stoichiometric solubilities of copper sulphides together with various common sulphides in a 3 molal sodium chloride solution with a pH of 5 at elevated temperatures. The solubilities depicted above are regarded as minimal approximations of the true mineral solubilities. Modified from Helgeson (1969).

1.4.2. Tracing the chalcophile elements in metal-sulphides

This study uses the chalcophile elements (together with Mo and Co) to investigate the geological record of the generation of diffuse fluids within the crust. In the Goldschmidt classification, chalcophile elements are the elements with a low affinity for oxygen and which preferentially bond with sulphur to form sulphides (Goldschmidt, 1937). This group comprises some transition elements (Cu, Zn, Cd, Ag,

Hg), heavy metals (Ga, In, Sn, Pb, Po, Bi, Tl), and metalloids (Ge, S, Sb, Se, Te, As) (Goldschmidt, 1937). This study will not discuss the behaviour of Hg, In, Po, Bi, Se, or Te due to the very low concentrations in oceanic crust and/or analytical difficulties. Molybdenum and Co are also investigated because of their similar behaviours to Cu during hydrothermal sulphide precipitation. (Fouquet et al., 1988; Fouquet et al., 1993; Hannington et al., 1991; Trefry et al., 1994).

Previous laboratory and field studies generally separate element partitioning into metal-sulphides into two groups: (1) Co and Mo partition into chalcopyrite and thus tend to be removed from fluids along with Cu at a temperature below 350°C (Fouquet et al., 1988, 1993; Hannington et al., 1991; Tivey et al., 1995), and (2) Ag, As, Cd, Ga, Ge, Pb, and Sb partition into sphalerite precipitated generally at lower temperatures (Goldschmidt and Peters, 1933; Zierenberg et al., 1984; Brewers et al., 1955; Fouquet et al., 1988; Tivey et al., 1995; Metz and Trefry, 2000). Published chalcophile element and Co concentration ranges in metal-sulphide minerals ore deposits and oceanic hydrothermal system are listed in Table 1.2 (Fleischer, 1955) and Table 1.3 (Patten et al., 2016), respectively. Fleischer (1955) compiled the data on minor elements in metal-sulphides based on concentration ranges published. Table 1.2 contains the data range of at least one sample reported, including the data of not found (as 0 ppm in Table 1.2) and the maximum concentrations reported. For the data of concentrations of minor elements in sphalerite, Table 1.2 compiled the concentration ranges of two or more than two samples reported in Fleischer (1955).

Table 1.2. Concentration (ppm) of the elements of interest in chalcopyrite, pyrite, sphalerite and galena from sulphide ore deposits (Fleischer, 1955). Data from all types of ore deposits, not limited to mafic-hosted deposits.

	Co	Cu	As	Ag	Cd	Mo	Pb	Sb	Sn	Tl	Zn
Chalcopyrite ($CuFeS_2$)[a]	0-2000			10-2300	180	70-900		20	0-770	0.03	0-10000
Galena (PbS)[a]		10-3000	0-10000	0-30000	0-1000			0-30000	0-1300	0-1000	
Sphalerite (ZnS)[b]	0-3000	0-50000	0-10000	0-10000	50-44000		0-100000	0-1000	0-4999	0-4999	
Pyrite (FeS_2)[a]	0->25000	0-~60000	0-50000	0-200	10	0-20	0-5000	0-700	0-400	0-100	0-~45000

a: at least one sample was reported in each concentration range
b: 2 or more than 2 samples were reported in the concentration range

Table 1.3. Median concentration (ppm) of the elements of interest in chalcopyrite, pyrite, sphalerite from oceanic crust at ODP Hole 1256D (Patten et al., 2016).

	Co	Cu	Zn	As	Ag	Sb	Pb
Chalcopyrite ($CuFeS_2$)		33.7	714	1.9	6.2	0.17	8.97
Sphalerite (ZnS)	300	1650	54.2	11.5	1.73	20.9	52.55
Pyrite (FeS_2)	900	25.9	5.9	23.7	2.39	0.33	14.6

Sphalerite and galena often coexist in massive sulphide deposits. Fleischer (1955) concluded that Pb and Sb occurred only in galena; Ag is commonly present in galena and only rarely found in small amounts in sphalerite free from galena inclusions; and Tl is present in galena, but not in pure sphalerites. Elements that partitioned into sphalerite and galena are often coupled together because of the possible co-precipitation of these two metal-sulphides (Table 1.2).

Copper, As, Ag, Cd, Sb, Sn, and Tl can partition into galena (Table 1.2). The content of Sb and Ag in galena decreases with decreasing temperature of galena formation (Fleischer, 1955). The content of Ag in galena correlates strongly with Sb (Wu and Petersen, 1977; Miller and Craig, 1983; Hackbarth and Petersen, 1984;

Johnson et al., 1986; Smith and Huston, 1992; Huston et al., 1992). This is interpreted to be controlled by the coupled substitution of Ag^{+} with Sb^{3+} in galena (i.e., $AgSbS_2$ for Pb_2S_2; Sharp and Buseck, 1993). Substitution into galena is thought to control the distribution of Ag in massive sulphide deposits (Amcoff, 1984). There is no galena observed in samples from Hole 1256D (Patten et al., 2016).

Copper, Sb and Pb are higher in sphalerite than other metal sulphides (Fleischer, 1955; Patten et al., 2016). Sphalerite often contains 50 to 44000 ppm Cd (Table 1.2). The content of Cd is higher in sphalerites from low-temperature deposits than those from mesothermal or high-temperature deposits (Fleischer, 1955). Cobalt is always present in sphalerite and its concentration does not correlate with the sphalerite formation temperature. In general, Sn concentrations are higher in sphalerite deposits formed at high to intermediate temperature than at low temperatures (Stoiber, 1940; Warren and Thompson, 1945).

Pyrite contains more As than the other metal-sulphides discussed in this section (Table 1.2 and 1.3). Arsenic correlates more strongly with Fe than with Cu in pyrite (Smith and Huston, 1992), which may result from As^{-} replacing S^{-} in pyrite to form arsenopyrite (FeAsS) as a solid solution component in pyrite. Therefore, among all the elements studied here, As may act as a tracer for pyrite precipitation. Arsenic and Ag contents of pyrite are higher in pyrite formed at low-temperatures than high-temperatures (Hawley, 1952). Cobalt concentrations are generally higher in pyrite from high-temperature than low-temperature deposits (Fleischer, 1955). Molybdenum is absent in pyrite from massive-sulphide deposits, but contained in vein-pyrite type deposits (Fleischer, 1955).

Chalcopyrite contains trace amounts of Co, Ag, Mo, and Sn in sulphide ore deposits (Table 1.2; Fleischer, 1955). In oceanic hydrothermal systems (Hole 1256D; Table 1.3), Zn and Ag concentrations are the highest in chalcopyrite of all listed metal sulphides (Patten et al., 2016).

In summary, hydrothermal fluids carry the metals leached from dikes, and the metal-sulphide precipitation in oceanic crust result from cooling the hydrothermal fluid and generating diffuse fluids. The two processes of fluids cooling, fluid mixing and conductive cooling, change the fluid conditions which affect the metal-sulphide solubility in different ways. Chalcopyrite is the first sulphide mineral precipitated when fluids cool down to lower than 350°C, which makes the enrichment of Cu in the crust a best tracer for a temperature decrease in the fluids, whereas the solubility of sphalerite is more dependent on pH changes. During conductive cooling of hydrothermal fluids, the decrease of pH may inhibit sphalerite. Thus, the enrichment of Zn in the crust is a good tracer for fluid mixing. Most of the common hydrothermal sulphide-minerals solubilities are sensitive to fluid temperature changes, which can cause the enrichment of the elements partitioning into these sulphides (e.g., Cu, Zn, As, Ag, Cd, Sb, Tl and Pb) in the crust. Therefore, the abundance of these elements in the upper crust is the tracer for diffuse fluids generation in geologic record.

1.4.3. Tracing diffuse fluids generation using the chalcophile elements

The distribution of chalcophile elements in the oceanic upper crust can be used to trace diffuse fluid generation. Cartoon models of the predicted distribution of chalcophile elements within the upper oceanic crust under different diffuse fluid

generation models are shown in Fig. 1.6. When high-temperature hydrothermal fluids reach the seafloor without cooling significantly, the chalcophile elements carried by these fluids will not precipitate in the lavas or the transition zone (Fig. 1.6 A). In contrast, if high-temperature fluids cool and generate diffuse fluids, the abundance of chalcophile elements is predicted to indicate the locations where fluid cooling occurs and the amount of diffuse fluids generated.

Different mechanisms and locations of diffuse fluid generation will lead to the chalcophile elements precipitating in the lava unit and the transition zone (Fig. 1.6 B), only in the transition zone (Fig. 1.6 C), and only in lava unit (Fig. 1.6 D). For example, if mixing of high-temperature fluids occurs immediately high-temperature fluid crosses leaves the sheeted dike complex where an element will be precipitated in the crust will depend on elements behaviour. If the solubility of the chalcophile element reacts slowly to temperature change (e.g., Pb; Fig. 1.5), the element will precipitate in both the lava unit and the transition zone (Fig. 1.6 A). If the solubility of the chalcophile element is highly sensitive to temperature change (e.g., Cu; Fig. 1.4), precipitation will take place almost entirely in the transition zone (Fig. 1.6 C). In contrast, if the temperature of the fluids decreases more slowly, the precipitation of the chalcophile elements may not start until the bottom of lava section, such elements will only be precipitated only in the lava unit (Fig. 1.6 D).

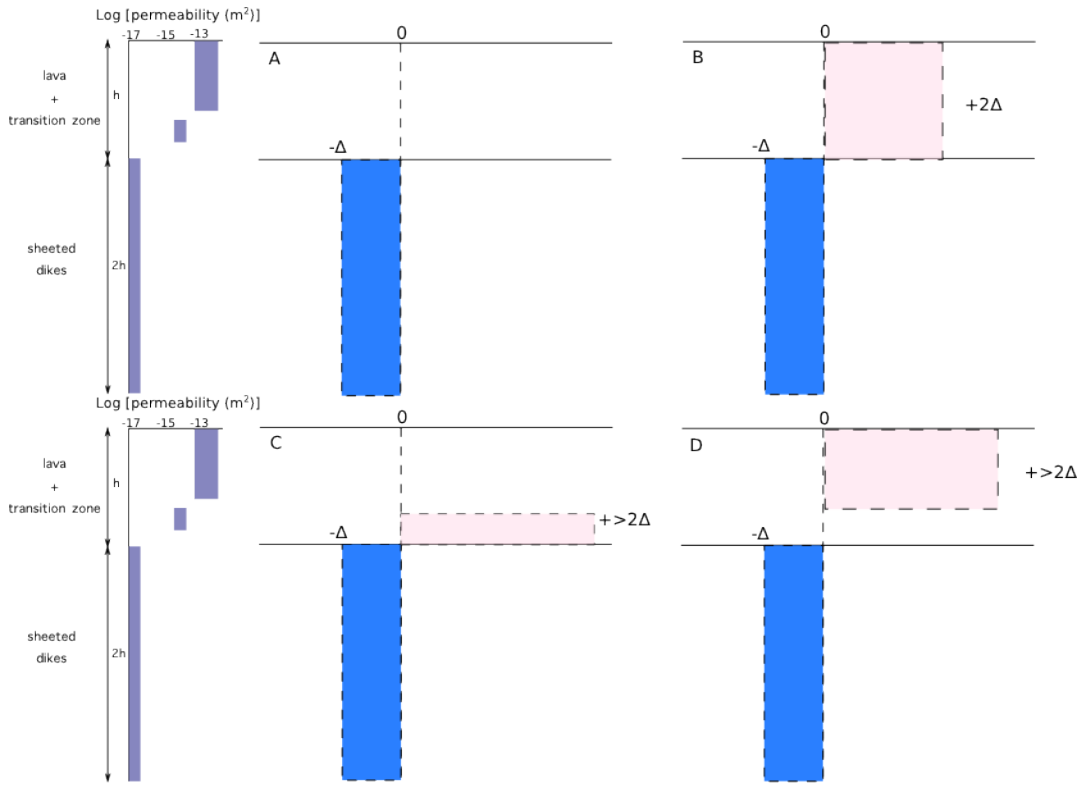

Figure 1.6. Cartoons of predicted chalcophile elements distribution in upper oceanic crust for end-member models. Purple-coloured bars represent bulk permeabilities (in log scale) within upper oceanic crust determined for Hole 504B (Fisher, 1998). Assuming high-temperature hydrothermal fluids mobilize certain amount (-Δ) of a chalcophile element, these amount of element will all be carried to the seafloor forming high-temperature fluid vents if no diffuse fluids were generated during the upwelling (Profile A). Profile B, C, and D show the distribution of chalcophile elements while forming diffuse fluids and precipitating all of the element within the crust. Profile B represents the chalcophile elements that precipitate in both the lava unit and the transition zone. For chalcophile elements like Cu, of which the solubility is highly temperature sensitive, the precipitation zone will be largely in the transition zone if this is where mixing starts (Profile C). Profile D represents the chalcophile elements with solubilities that are less temperature sensitive, which only start precipitating in the lava section.

1.5. Thesis Objectives and Structure

The primary objective of this study is to determine whether the distribution of chalcophile elements in the upper oceanic crust can be used to track the formation mechanism and location of diffuse fluids within the crust.

This thesis first develops a method for analyzing selected chalcophile elements (Ga, Ge, As, Ag, Cd, Sn, Sb, and Pb) in geological reference materials and rock samples in ICP-MS, using a standard addition method and estimating possible interferences (Chapter 2). The analytical method is applied to samples from Pito Deep, where crust formed on the fast spreading ridge East Pacific Rise (EPR) is exposed, to test whether both leaching and precipitation of these elements within the crust can be observed (Chapters 3 and 4). This thesis then discussed the plausible models for generating diffuse fluids that are consistent with the Pito Deep data and other constraints (e.g. thermal and vent fluid chemistry) and calculated the concentrations of the elements of interest in diffuse fluids (Chapter 5).

Chapter 2

2. ANALYTICAL METHOD DEVELOPMENT

Trace element analysis of materials by Inductively Coupled Plasma Mass Spectrometry (ICP-MS) can be performed because there is generally a linear relationship between the concentration of a given element in solution and the signal (counts per second) measured by the instrument. Standard reference materials of similar compositions to the unknowns are commonly used to calibrate such analyses. Knowledge of the composition of reference materials allows us to build calibration curves to determine the composition of unknown rock samples. Institutions like the United States Geological Survey (USGS) and the Geological Survey of Japan (GSJ) provide standard rock materials that have been analyzed in a wide range of laboratories and basaltic samples from these collections are used for calibration in this study (Table 2.1).

Table 2.1. Reference materials used in this study

Name	Type	Provenance
AGV-1	Andesite, Guano Valley	USGS
BCR-2	Basalt, Columbia River	USGS
BHVO-2	Basalt, Hawaiian Volcanic Observatory	USGS
BIR-1	Basalt, Reykjavlk	USGS
DNC-1	Dolerite, North Carolina	USGS
JG-2	Granite, Naegi granite, Japan	GSJ
JGb-1	Gabbro, Utsushigatake gabbro, Japan	GSJ

The GeoRem database provides a compilation of published elemental concentrations of reference standards obtained by different analytical methods (http://georem.mpch-mainz.gwdg.de; Jochum et al., 2005). The composition for

some elements in the GeoRem database is not always available or is too poorly constrained to use these to derive calibration curves. Because of the lack of high quality data for many of the elements of interest in this study (As, Ag, Cd, Mo, Sn, and Tl), the first stage of this project involved determining the concentration of these elements in the reference materials listed in Table 2.1.

2.1. Isotopes and Potential Interferences for the Elements to be Analyzed in the Reference Materials

In order to determine the concentration of the elements of interest in the reference materials (Table 2.1) by ICP-MS we need to consider the possible interferences at each isotope mass. Of the elements to be analyzed, As is monoisotopic, whereas Ag, Cd, Mo, Sn, and Tl all have more than one natural isotope allowing measurements at different masses to be compared to evaluate data quality. Potential isobaric interferences are listed in Table 2.2. For some elements, the interferences caused by polyatomic sources also need to be considered (Table 2.3).

Molybdenum has seven isotopes (between masses 92 and 100) that suffer from various interferences; ^{92}Mo, ^{94}Mo, and ^{96}Mo have isobaric interferences from ^{92}Zr, ^{94}Zr, and ^{96}Zr respectively while ^{98}Mo and ^{100}Mo have isobaric interferences from ^{98}Ru and ^{100}Ru respectively. Because Ar is used to generate the plasma in the ICP-MS instrument, the polyatomic interference $^{40}Ar_2{}^{16}O^1H^+$ (Table 2.3) on atomic mass 97 cannot be avoided or calculated precisely. Thus, ^{95}Mo was selected for determining Mo concentration, which has no known isobaric interferences.

For determining the concentration of Cd, the relatively high abundance ^{110}Cd

and ^{111}Cd were selected. However, they are effected by polyatomic interferences (Table 2.3) as discussed below.

For Sn, ^{117}Sn and ^{118}Sn was selected for determining the Sn concentration, as they do not have isobaric or polyatomic interferences.

The two isotopes of Ag at atomic mass 107 and 109 both have polyatomic interferences (Table 2.3), which can be measured and corrected for.

Table 2.2. Element abundance chart showing the isotopes of interest in this study. Orange cells: atomic mass; green cells: elements of interest; numbers in white cells: isotopic abundance (%).

Atomic Mass	92	94	95	96	97	98	100		
Zr	17.1	17.38		2.6					
Mo	14.8	9.2	15.9	16.7	9.6	24.1	9.6		
Ru						1.9	12.6		
Atomic Mass	106	108	110	111	112	113	114	115	116
Cd	1.3	0.9	12.5	12.8	24.1	12.2	28.7		7.5
Sn					1.0		0.7	0.3	14.5
In						4.3		95.7	
Pd	27.3	26.5	11.7						
Atomic Mass	117	118	119	120	121	122	123	124	
Sn	7.7	24.2	8.6	32.6		4.6		5.8	
Te				0.1		2.6		0.9	

Note:
Reference for isotopic abundance: (Zr) Nomura et al., 1983; (Mo) Moore, et al., 1974; (Ru) Huang and Masuda, 1997; (Cd) Rosman et al., 1980; (Sn) Devillers, et al., 1983; Rosman et al., 1984; (In) Chang and Xiao, 1991; (Pd) Shima et al., 1978; (Te) Smith et al., 1978; (Sb) Chang et al., 1993

Table 2.3. Polyatomic interferences on the isotopes of interest

Isotope	Isotopic Abundance	Interferences	References
^{107}Ag	51.8	$^{91}Zr^{16}O^{+}$	Beary and Paulsen, 1993; Evans and Giglio, 1993
^{109}Ag	48.2	$^{92}Zr^{16}O^{1}H^{+}$, $^{93}Nb^{16}O^{+}$	Evans and Giglio, 1993
^{75}As	100	$^{12}C^{31}P^{16}O_2^{+}$, $^{23}Na^{12}C^{40}Ar$	Evans and Giglio, 1993
^{95}Mo	15.9	$^{94}Zr^{1}H$, $^{31}P_2$ $^{16}O^{17}O$	
^{97}Mo	9.6	$^{40}Ar_2{}^{16}O^{1}H^{+}$, $^{40}Ca_2{}^{16}O^{1}H^{+}$, $^{40}Ar^{41}K^{16}O^{+}$, $^{81}Br^{16}O^{+}$	Beary and Paulsen, 1993; Vandecasteele, et al., 1993
^{110}Cd	12.5	$^{94}Zr^{16}O$, $^{93}Nb^{16}OH$, $^{39}K_2{}^{16}O_2^{+}$	Beary and Paulsen, 1993
^{111}Cd	12.8	$^{94}Zr^{16}OH^{+}$, $^{39}K_2{}^{16}O_2{}^{1}H^{+}$, $^{93}Nb^{17}OH$	McLaren et al., 1987; Beary and Paulsen, 1993

To determine the abundance of the elements of interest in the reference materials I developed a standard addition method (Section 2.2). This provides an accurate way to determine the concentration of an element in a sample if there is no interfering species at the same mass. However, polyatomic interferences are not removed using this approach. For example, Table 2.3 shows, $^{91}Zr^{16}O^{+}$ is an important polyatomic interference on ^{107}Ag and simply using a standard addition method will not account for this. To resolve such interferences, single element solutions of possible interfering elements were analyzed and the count rates at both the mass of an interference free isotope of the single element and at the mass of the interference of interest were monitored allowing a correction factor to be calculated.

2.2. Standard Addition Method

2.2.1. Principles of analysis using standard addition

The method of standard addition offers better accuracy than external standardization and is generally less expensive than isotope dilution, an alternative

approach. A series of different amounts of the analyte, a spike, are added to the unknown solution. The increase in signal per unit of spike added is used to determine the concentration of the analyte in the sample by regressing the concentration of the analyte added against the count rate. The negative value of the intercept is the initial concentration of the unknown solution (Abbyad et al., 2001) (Fig. 2.1).

Standard addition requires the use of known quantities of element spike solutions added into each reference material solution in order to build a regression line (Fig. 2.1). Five spikes with increasing concentrations and the same amount of 2% HNO_3 (the matrix solution all samples are analyzed in) were added into 6 aliquots of each reference material with the sixth solution added being a blank.

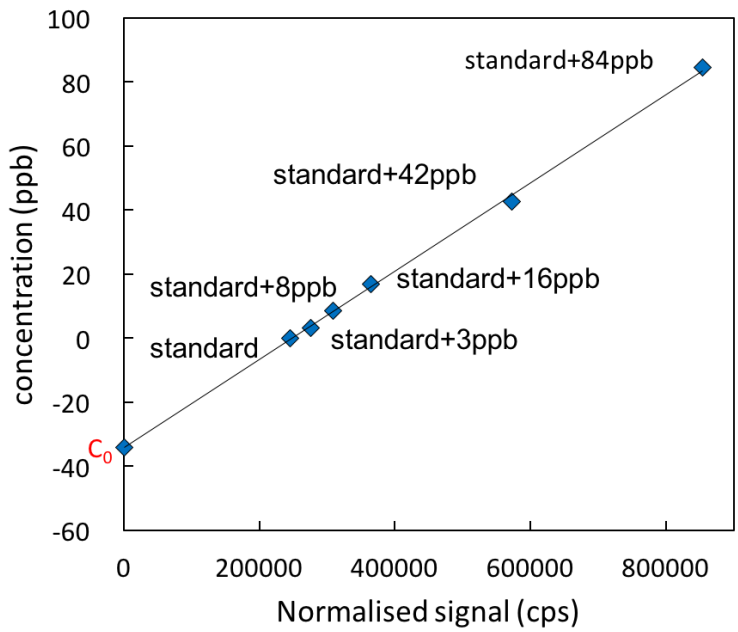

Figure 2.1. An example of the standard addition method showing experimental data points and the extrapolated linear regression line, which intercepts the y-axis at C_0. The concentration in the standard solution (C_{std}) = $-C_0$.

2.2.2. Single element solutions preparation

The possible interferences on Ag, As, Mo and Cd are listed in Table 2.3. As introduced in Section 2.1, the polyatomic interferences could be measured and calculated by analyzing single element solutions. Therefore, single element solutions of Na, P, K, Zr, and Nb were prepared (Table 2.4) to determine the interference on the elements of interest and develop corrections for each of these. Three different concentrations of each single element solution were prepared. Zr has five isotopes: ^{90}Zr, ^{91}Zr, ^{92}Zr, ^{94}Zr, ^{96}Zr. The isotopes ^{92}Zr and ^{94}Zr have interferences from ^{92}Mo and ^{94}Mo respectively, and ^{96}Zr has a very low abundance (2.799%) comparing with ^{90}Zr (51.452%) and ^{91}Zr (11.223%). Therefore, interferences from Zr were determined based on the count rates of ^{91}Zr.

Table 2.4. Concentrations of single element solutions used to identify interferences and develop corrections.

Element	Concentrations of the single element solutions			Isotopes monitored
Na	2500 ppb	4900 ppb	10000 ppb	^{23}Na, ^{75}As
K	2500 ppb	4600 ppb	10000 ppb	^{39}K, ^{110}Cd, ^{111}Cd
P	2500 ppb	5000 ppb	10000 ppb	^{31}P, ^{75}As, ^{95}Mo, ^{110}Cd, ^{111}Cd
Zr	20 ppb	40 ppb	60 ppb	^{91}Zr, ^{95}Mo, ^{107}Ag, ^{109}Ag, ^{110}Cd, ^{111}Cd
Nb	10 ppb	20 ppb	40 ppb	^{93}Nb, ^{109}Ag, ^{110}Cd, ^{111}Cd

2.2.3. Spike solution preparation

To determine the concentration of As, Ag, Mo, Cd, Sn, and Tl in the selected reference materials (Table 2.1), a stock solution with the known concentration of these elements was prepared (Table 2.5). The five spike solutions were diluted from this stock solution. A concentration range that brackets the likely concentration

ranges in the unknowns is required for determining multiple spike concentrations. This range was determined based on the published values listed on GeoRem (http://georem.mpch-mainz.gwdg.de; Jochum et al., 2005); these are reported in Table 2.6).

The spike stock solution was prepared by adding each single element standard solutions (Ag, As, Cd, Mo, Sn, Tl), and diluting with 1% nitric acid (Table 2.5). Once the stock solution was made, this mixture was diluted down to the working concentrations for spike solutions (Table 2.6).

Six aliquots (3 ml) of the standard solutions of each reference material were added to 3 ml of spike solutions (Table 2.6). Two procedure blanks were prepared the same way as the reference material solutions in order to determine the blank signal. A mixture of the spiked standards solutions was prepared as a drift solution for monitoring the instrument drift during the day.

Table 2.5. Concentration of stock solution.

Elements	Concentration (ppb)
Ag	7.935
As	199.9
Cd	19.98
Mo	359.1
Sn	500.89
Tl	19.93

Table 2.6. Concentration of working spike solutions.

Spike ID	Ag (ppb)	As (ppb)	Cd (ppb)	Mo (ppb)	Sn (ppb)	Tl (ppb)
0	0	0	0	0	0	0
1	0.0031	0.0773	0.0077	0.1388	0.1937	0.0077
2	0.0078	0.1971	0.0197	0.3541	0.4939	0.0197
3	0.0157	0.3967	0.0397	0.7127	0.9941	0.0396
4	0.0391	0.9861	0.0986	1.7715	2.4710	0.0983
5	0.0775	1.9536	0.1952	3.5094	4.8950	0.1948

2.3. Instrument Settings and Analytical Run Conditions

The samples were analyzed on a Thermo X-Series 2 quadrupole ICP-MS at University of Victoria. The solutions were analyzed in both standard mode and Collision/Reaction Cell (CRC) mode. The plasma, cooling and auxiliary gas is Ar, and the cell gas in the CRC is 7% H_2 in He. An analytical sequence was selected to minimize the memory effect, and this is described in Appendix A. Each solution was analyzed in four runs, with 30 sweeps of each mass in a run. The average count rates were used for data reduction (Section 2.4). Operation conditions are given in Table 2.7.

Table 2.7. Operating parameters used during ICPMS analyses in this study

Forward RF power (watts)	1400
Nebulizer gas flow rate (l min^{-1})	0.91
Cool gas flow rate (l min^{-1})	13
Auxiliary gas flow rate (l min^{-1})	0.8
Cell gas flow rate (ml min^{-1})	3.0

2.3.1. Basic Principles of Collision/Reaction Cell

The approach of CRC is to remove polyatomic and molecular interferences by colliding the ions within a collision cell (Thomas, 2001). Ions enter the interface in the normal manner, where they are extracted under vacuum into a collision cell that is positioned before the analyzer quadrupole (Fig. 2.2). The collision cell gas leads to

ion-collision and reduces the interferences. For example, the species $^{95}Mo^{16}O^{+}$ has interference on ^{111}Cd, which will be turned into $^{95}Mo^{16}O^{1}H$ in the collision cell as follow:

$$^{95}Mo^{16}O^{+}+H^{+}=^{95}Mo^{16}O^{1}H$$

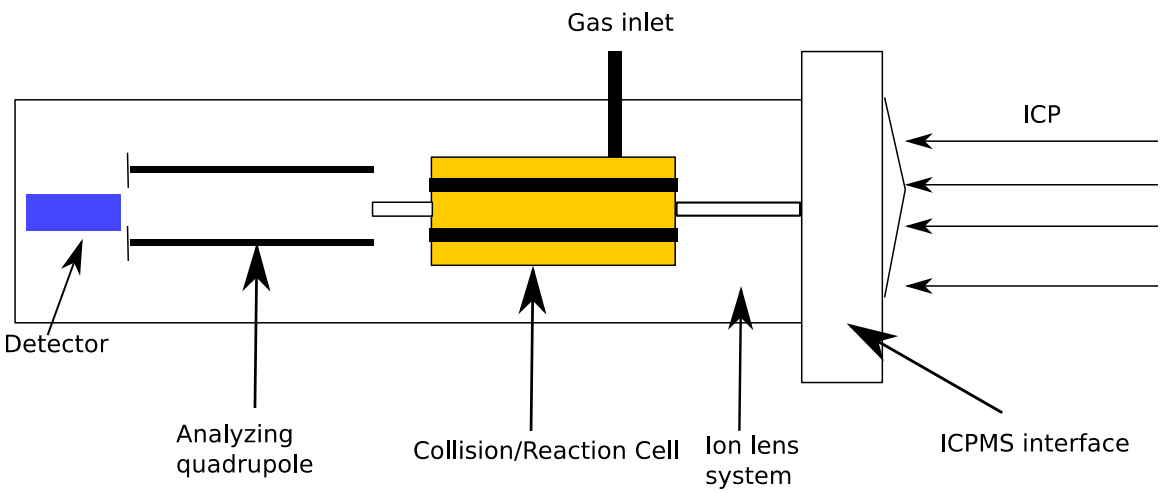

Figure 2.2. A typical collision cell instrument. Adapted from Thomas, 2001

2.4. Data Reduction

The raw count rate data of standard addition method and the process of data reduction are in Appendix B. The procedure of data reduction from raw count rate data to final concentration has six steps. The first step is to correct the count rates for the variation in dilution factor. The reference materials are prepared by powder dissolution and dilution, which introduces in dilution factor (DF_1) (Equation 2.1). Spiking these solutions introduces two more dilution factors (DF_2 and DF_3) (Equation 2.2 and 2.3).

$$DF_1 = \frac{M_{STD}}{M_F} \qquad \textit{Equation 2.1}$$

$$DF_2 = \frac{M_T}{M_T + M_x} \qquad \textit{Equation 2.2}$$

$$DF_3 = \frac{M_{xa}}{M_T + M_x} \qquad \textit{Equation 2.3}$$

where, DF_1 is the dilution factor of the reference materials in diluted HNO_3; DF_2 is the dilution factor of reference materials mixed with the spike solution; DF_3 is the dilution factor of the spike in the final solution; M_{STD} is the weight of the powdered reference materials; M_F is the total weight of the solution of the reference materials; M_T is the weight of the aliquot of the reference materials solution; M_x is the weight of each of the six working spike solution, x represents spike number 0 to 5 (Table 2.4).

The dilution factor corrected signal of element i in the solution of reference materials (CPS_{DF}^{i}):

$$CPS_{DF}^{i} = CPS_{RAW}^{i} / (DF_1 \times DF_2) \qquad \textit{Equation 2.4}$$

where, CPS_{RAW}^{i} is the raw signal for element i.

The concentration of element i in the spike x ($X_{DF(x)}^{i}$) added into the standard solution is:

$$X_{DF(x)}^{i} = X_x^i \times DF_3 \qquad \textit{Equation 2.5}$$

where, X_x^i is the concentration of element i in the working spike solution (Table 2.4).

The second step of the data processing is internal standardization. Internal standards were added online into all the analyzed solutions; these were ^{103}Rh, ^{115}In, and ^{185}Re. The raw signal for each internal standard had a smooth drift over the run. The elements of interest that were analyzed have an atomic mass range of 75-205. ^{115}In was selected as the internal standard for all elements because it is the most similar in mass to the elements of interest.

For each solution analyzed, the dilution factor corrected signals for the analyte elements was divided by the signal of ^{115}In in that sample to obtain an internal standard normalized signal (CPS_{In}^{i}):

$$CPS_{In}^{i} = CPS_{DF}^{i} / CPS^{In} \qquad \textit{Equation 2.6}$$

where, CPS_{DF}^{i} is the dilution factor corrected signal of element i, and CPS^{In} is the signal of the internal standard (^{115}In).

For the signals in single elements solutions, the internal standardization of element i ($CPS_{In(SE)}^{i}$) is :

$$CPS_{In\,(SE)}^{i} = CPS_{SE}^{i} / CPS_{SE}^{In} \qquad \textit{Equation 2.7}$$

where, CPS_{SE}^{i} is the raw signal of element i in single element solution, and CPS_{SE}^{In} is the raw signal of the internal standard (^{115}In) in single element solution.

The third step of the data processing is blank correction. During the dissolution of the samples, the procedure blanks were prepared identically to the samples.

The signals of the blanks are constant and negligible (<< 1% of the lowest sample value). Thus the average of the corrected and normalized blank signal was subtracted from the samples analyses (Equation 2.8),

$$CPS_{BLANK}^{i} = CPS_{In}^{i} - CPS_{APBK}^{i} \qquad \textit{Equation 2.8}$$

where, CPS_{BLANK}^{i} is the blank corrected signal for element i; CPS_{In}^{i} is the internal standard normalized signal for element i; and CPS_{APBK}^{i} is the average signal for element i in the procedure blanks.

The signals of the single element solutions are not corrected using Equation 2.8.

A 2% HNO_3 solution was run at regular intervals throughout the analyses. The blank correction of the signals in single element solutions $CPS_{BLANK(SE)}^{i}$ is:

$$CPS_{BLANK(SE)}^{i} = CPS_{In\,(SE)}^{i} - CPS_{HNO_3(SE)}^{i} \qquad \textit{Equation 2.9}$$

where, $CPS_{HNO_3(SE)}^{i}$ is the internal standard normalized signal of 2% HNO_3 analyzed most closely in time before the single element solution was analyzed.

The fourth step is drift correction. As introduced in Section 2.3.1, a mixed sample solution was used as a drift monitor to correct for secondary drift. Secondary drift is the drift that not been corrected for by internal standardization.

For a drift that is linear, a best-fit line of the ratios of counts to the first drift solution counts (y=mx+c) was calculated, where y is the correction factor and x is the analysis number. Drift corrected signal (CPS_{SECD}^{i}) can be calculated as:

$$CPS_{SECD}^{i} = CPS_{BLANK}^{i}/y \qquad \textit{Equation 2.10}$$

where, y is the secondary drift correction factor. Alternatively, for non-linear drift the polynomial lines were used for calculating the secondary drift correction factor.

The fifth step in the data processing is interference correction based on the analysis of the single element solutions. The signal of the interfered mass against the signal of the interference source element in single element solutions were regressed, which allows calculation of the magnitude of the interference. The slope of the regression line is the interference correction factor (INF). For example, $^{91}Zr^{16}O^{+}$ has a mass of 107, which overlaps ^{107}Ag. Three Zr single element solutions with different concentration were analyzed. Calculation of a regression line of the ^{91}Zr signal and

the signal at mass 107, forced through the origin, allows determination of an interference correction factor for $^{91}Zr^{16}O^{+}$ on ^{107}Ag (Fig. 2.3).

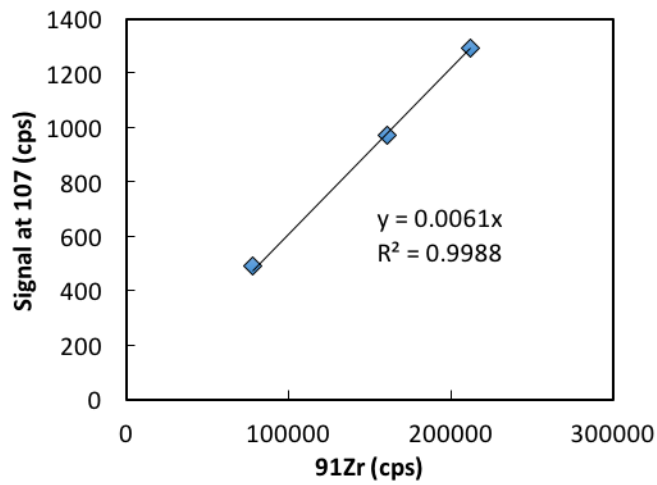

Figure 2.3. Regression line for the signals at ^{91}Zr (represent the interference source $^{91}Zr^{16}O^{+}$ on ^{107}Ag) and ^{107}Ag analyzed in Zr single element solutions. The interference corrected ^{107}Ag signal is subtracting 0.0061 times of the ^{91}Zr signal (x in the plot) from the signal of mass 107.

The interference corrected signal is calculated as:

$$CPS_{INF}^{\ i} = CPS_{SECD}^{\ i} - INF \times CPS_{SECD}^{\ int} \qquad \textit{Equation 2.11}$$

where, $CPS_{SECD}^{\ i}$ is the signal of the element needs to be interference corrected after secondary drift correction, and $CPS_{SECD}^{\ int}$ is the signal of the isotope that causes the interferences after secondary drift correction.

The final step in the data processing is calibration, and this will achieve the concentration of the elements of interest in the seven standards. Equation 2.5 shows calculation of the dilution factor corrected signal of elements in the each working spikes. Using the standard addition method, the corrected count rates (calculated by Equation 2.11) and the concentrations of working spikes are regressed against one

another. Extrapolation of the calibration line to intercept with the concentration axis gives the concentration of the element as the negative value of the intercept.

2.5. Concentration of Selected Chalcophile Elements in Reference Materials

2.5.1. Interference correction factors from analysis of single element solutions

The elements of interest were analyzed in CRC and standard mode, which allows us to evaluate interferences and helps to achieve better quality data. In considering the interference correction factor, the larger the correction factor the larger the uncertainty in the final data.

The count rate at any mass is made up of contributions from the isotope of interest and counts from interfering species. The scale of the interferences on each isotope of interest due to each possible interference was calculated from the count rates on the single element solutions and the count rates on the reference materials. These are shown in Fig. 2.4 with the aim of identifying the isotope and method (standard mode or CRC mode) that requires the smallest corrections and thus are likely to give the most precise data.

The interference from $^{91}Zr^{16}O^{+}$ at mass 107, measured in both CRC and standard mode (Table 2.8), has large correction factor (>50%), which makes the corrected data of ^{107}Ag less reliable than ^{109}Ag (Fig. 2.4 A and B). Likewise, the correction factors for $^{92}Zr^{16}O^{1}H$ and $^{93}Nb^{16}O$ at mass 109 measured in standard mode (Fig. 2.4 C) makes the corrected data of ^{109}Ag less reliable than the data measured in CRC mode (Fig. 2.4 D). However, even in CRC mode, the data for ^{109}Ag in JG-2 and BCR-2 are less reliable than the other reference materials because of the relative high (>70%) correction factor

(Table 2.8). The data from ^{109}Ag in CRC mode has the smallest correction factor among these four set of data (Table 2.8), therefore, it is used for determining Ag concentrations.

Table 2.8. Interference correction factor (in percentage) for Ag in reference material

Analytical method	Isotope	BIR-1a	BHVO-2	AGV-1	JGb-1	JG-2	DNC-1	BCR-2
Standard mode	^{107}Ag	37.3	77.3	75.5	60.5	89.1	61.7	82.9
	^{109}Ag	12.9	69.9	58.1	43.8	82.6	30.7	82.2
CRC	^{107}Ag	20.8	66.1	61.1	43.1	77.5	41.7	72.4
	^{109}Ag	6.6	53.7	41.9	28.9	73.3	20	71.8

The correction factor for ^{95}Mo indicates that the data analyzed in standard mode has a smaller interference correction factor than the data analyzed in CRC mode (Fig. 2.4 E and F). This is interpreted to be the result of the 7% H_2 in the CRC cell gas forming the interfering species $^{94}Zr^{1}H$ at mass 95. In the standard mode, ^{95}Mo does not have as large an interference from $^{94}Zr^{1}H$. Therefore, ^{95}Mo analyzed in standard mode is used to determine Mo concentrations.

For Cd, the isotope ^{111}Cd analyzed in both modes (Fig. 2.4 E and F) gave smaller interference correction factors than ^{110}Cd (Fig. 2.4 G and H). However, the corrections on JG-2 for ^{111}Cd in both modes are too large (over 100%), such that effectively all the signal at mass 111 is from the interferences ($^{94}Zr^{16}O^{1}H$, $^{39}K_2{}^{16}O_2{}^{1}H^+$, and possibly $^{93}Nb^{17}O^{1}H^+$). ^{111}Cd analyzed in CRC mode is used for Cd concentration.

Arsenic was only analyzed in standard mode, because the interference species $^{36}Ar^{38}Ar^{1}H^{+}$ forms in CRC mode because of the 7% H_2 in the collision cell gas. The correction factors are below 11% for all of the reference materials (Fig. 2.4 K).

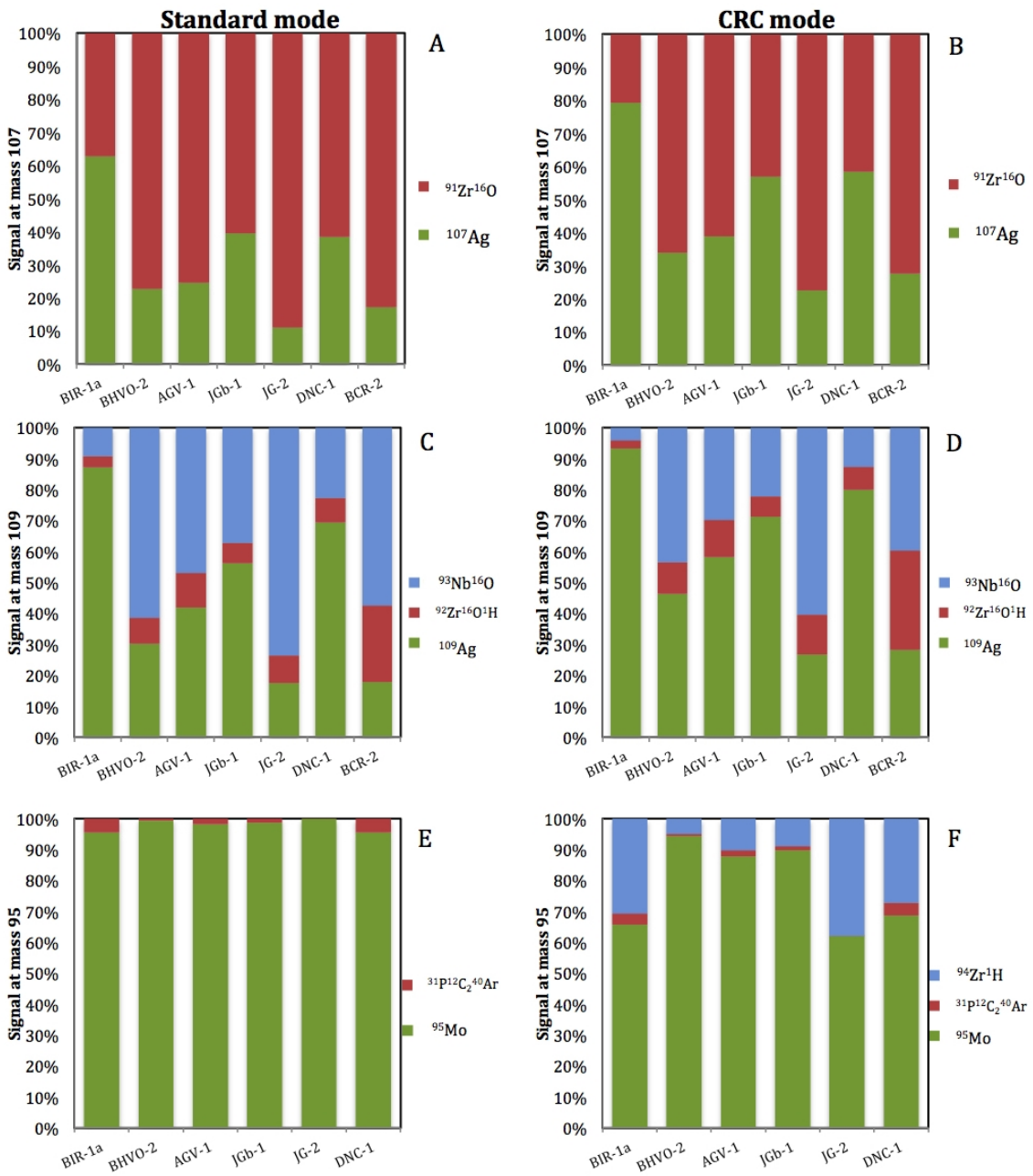

Figure 2.4. (Caption on following page)

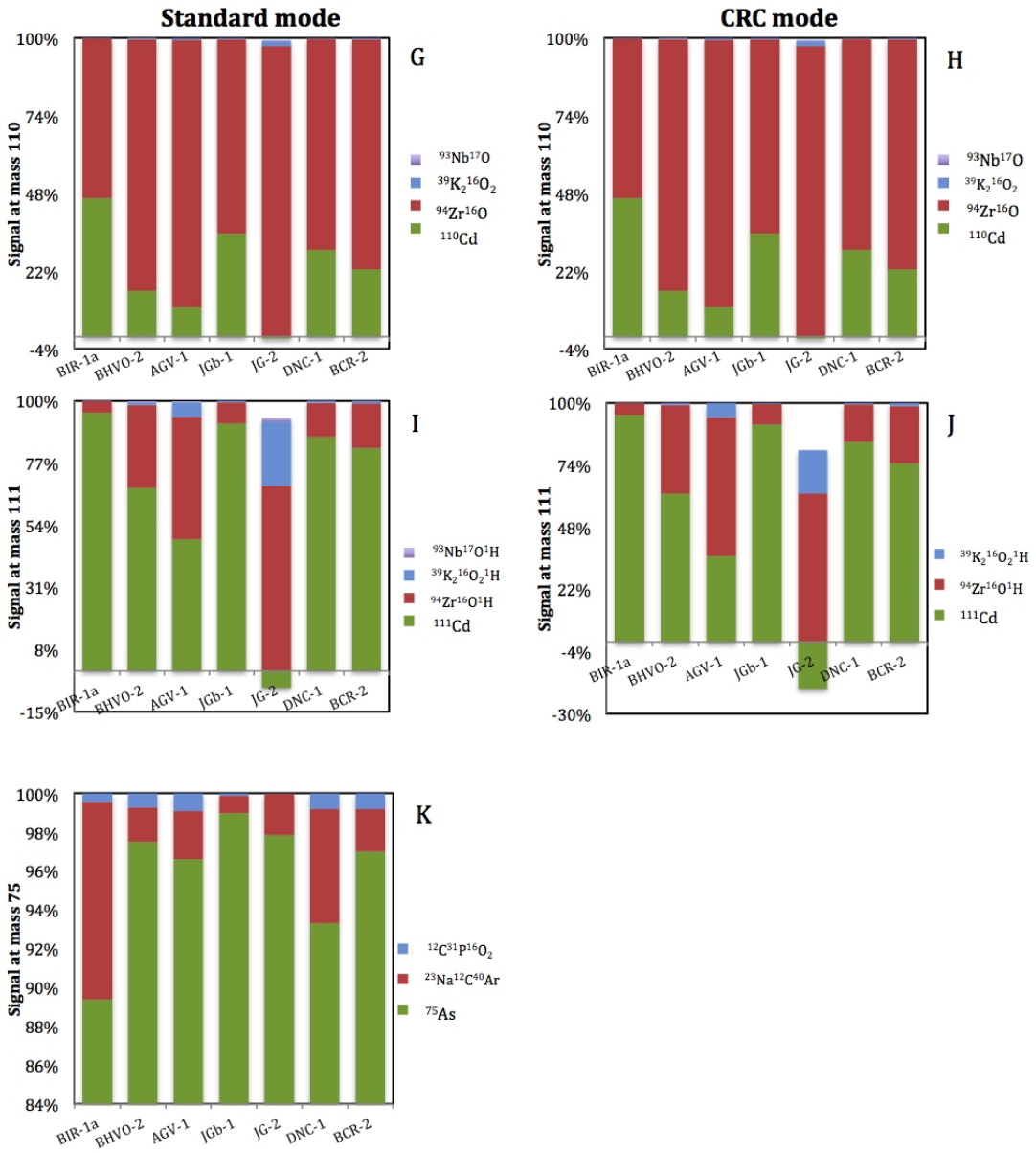

Figure 2.4. Histograms showing interference corrections as a proportion of the total count rate on the elements of interest in CRC and standard mode. (A): signal at mass 107 in standard mode; (B): signal at mass 107 in CRC mode; (C): signal at mass 109 in standard mode; (D): signal at mass 109 in CRC mode; (E): signal at mass 95 in standard mode; (F): signal at mass 95 in CRC mode; (G): signal at mass 110 in standard mode; (H): signal at mass 110 in CRC mode; (I): signal at mass 111 in standard mode; (J): signal at mass 111 in CRC mode; (K): signal at mass 75 in standard mode (note the compressed scale in this part). Negative values in (G), (I), and (J) represent that effectively all of the signal from the element of interest is coming from the interferences. Note variable y-axis scales. See text for details.

2.5.2. Chalcophile element compositions in the reference materials

The concentrations of the spikes added into reference material solutions can be calculated with the information in Table 2.6 and the dilution factor of spikes (Equation 2.5) in each reference material solution. To determine the concentration of the unknown element of the standard, the signal (counts per second) was first corrected for the interferences described above and then these corrected signals used to make calibration curves with the concentration of the corresponding element concentration of spikes (e.g. as shown in Fig. 2.1). The calibration curve intercepts at a negative value of concentration axis. The absolute value of the intercept is the concentration of the solution.

The standard addition calibration curves used to determine the concentrations of As in the reference materials are shown in Figure 2.5. The published Mo concentration in BCR-2 is much higher than other standards (due to contaminations from materials used for crushing or powdering this standard), which was excluded in the calibration curves (Fig. 2.6). As discussed in Section 2.5.1, ^{109}Ag in CRC mode, ^{111}Cd analyzed in standard mode have the best data quality. The calibration curves of ^{109}Ag analyzed in CRC mode and ^{111}Cd analyzed in standard mode are shown in Figure 2.7 and Figure 2.8. Sn has two isotopes at mass 117 and 118, they were analyzed in both CRC and standard mode. The calibration curves are all shown in Figure 2.9. ^{205}Tl was also analyzed in both modes (Fig. 2.10). Calibration curves for all the elements achieved in this study have good fit curves (R^2 >0.96). The concentrations of As, Mo, Ag, Cd, Sn, and Tl determined in the seven reference materials using this approach are shown in Table 2.9.

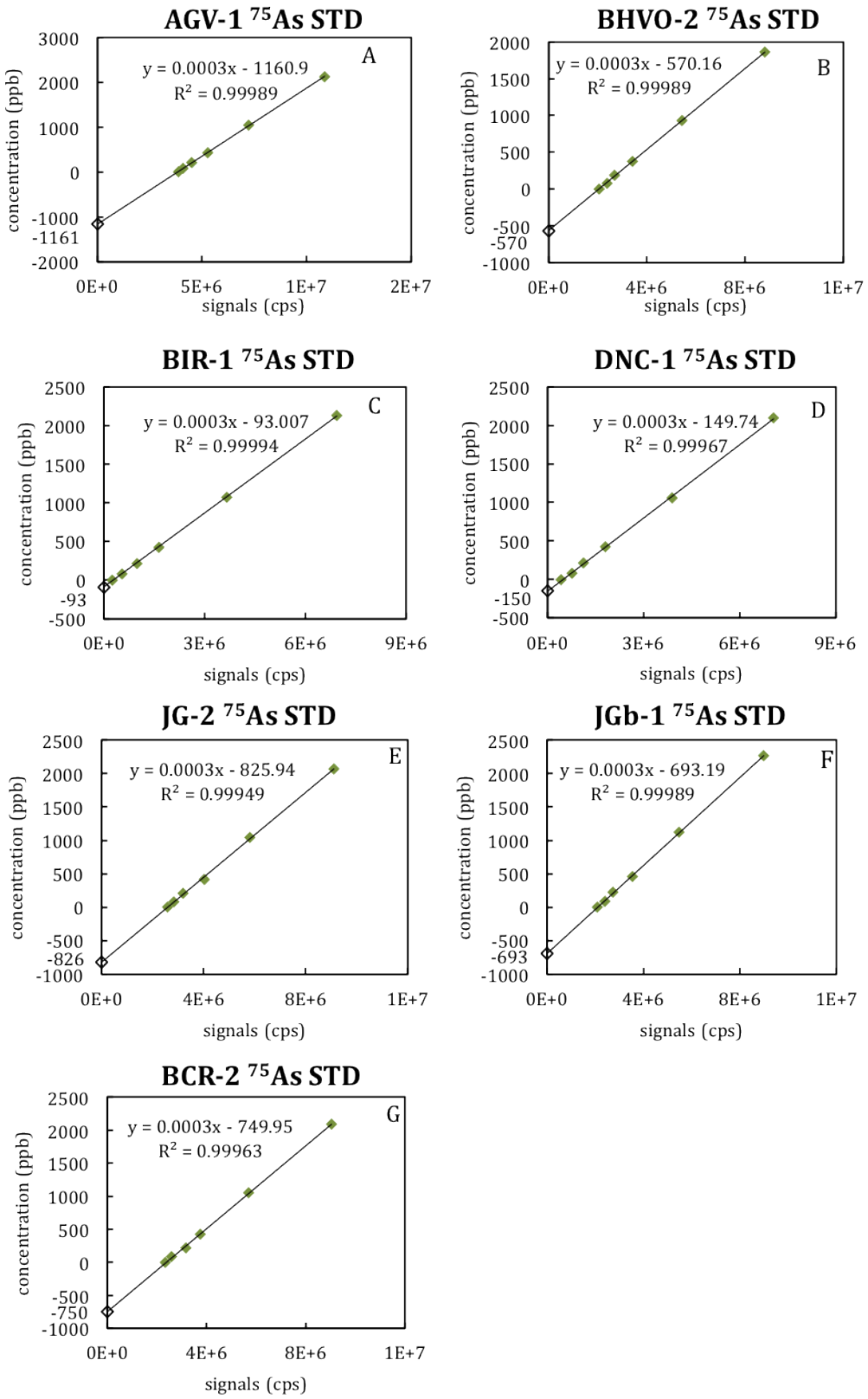

Figure 2.5. Standard addition calibration curves of ^{75}As in standard mode of the standards: (A) AGV-1; (B) BHVO-2; (C) BIR-1; (D) DNC-1; (E) JG-2; (F) JGb-1; (G) BCR-2.

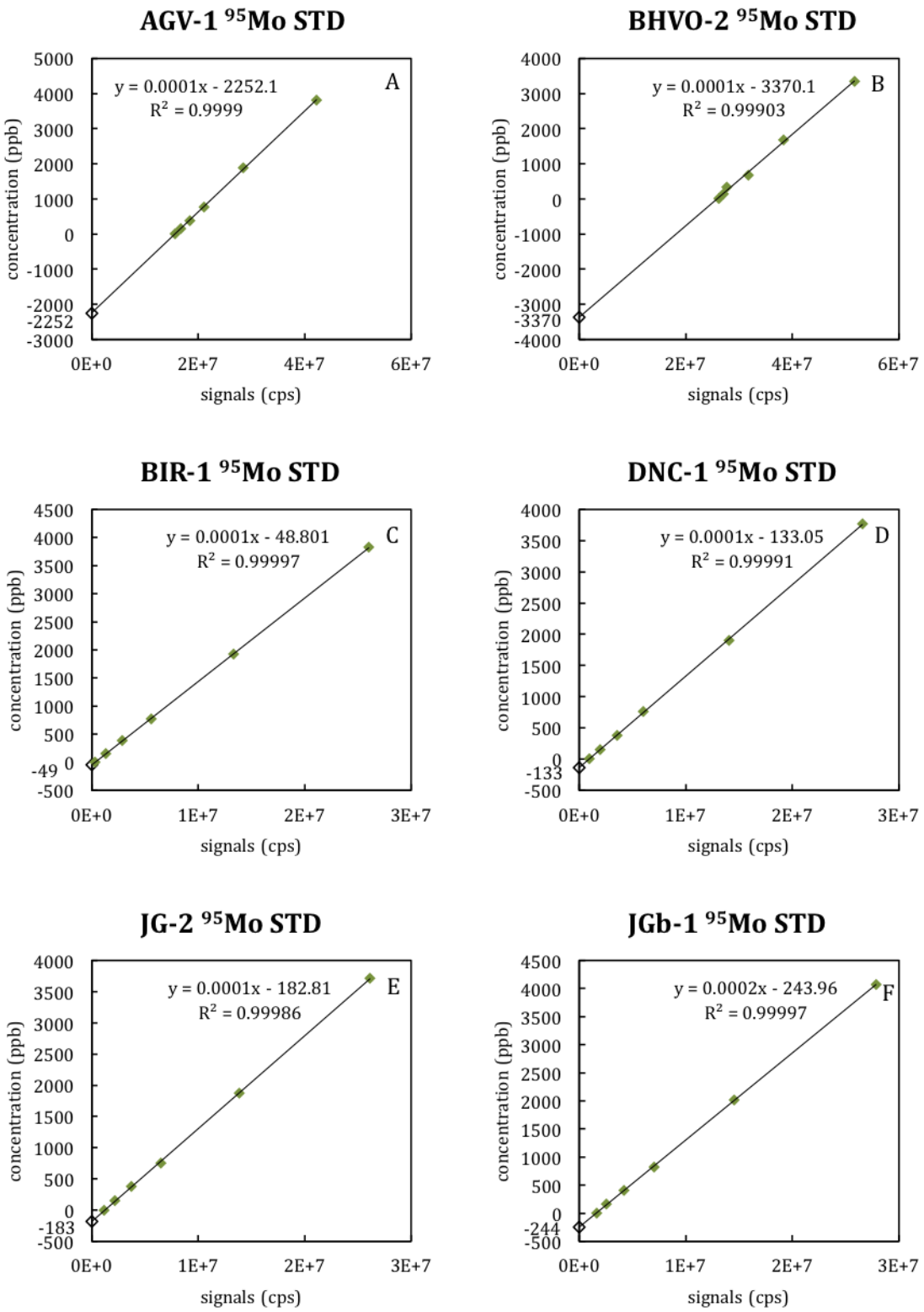

Figure 2.6. Standard addition calibration curves of ^{95}Mo in standard mode in the six reference materials. (A) AGV-1 in standard mode; (B) BHVO-2 in standard mode; (C) BIR-1 in standard mode; (D) DNC-1 in standard mode; (E) JG-2 in standard mode; (F) JGb-1 in standard mode.

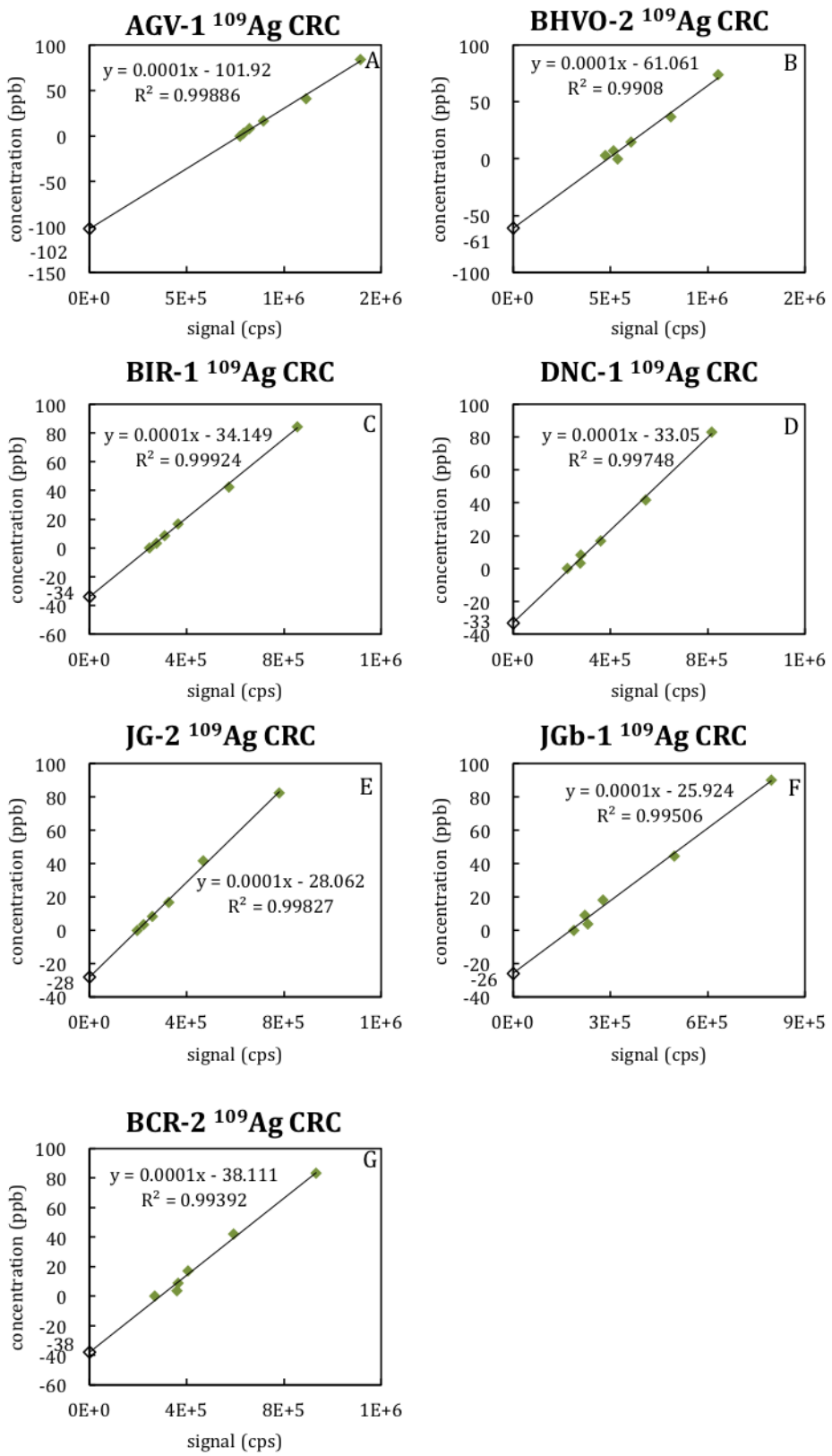

Figure 2.7. Standard addition calibration curves of ^{109}Ag in CRC mode of the standards: (a) AGV-1; (b) BHVO-2; (c) BIR-1; (d) DNC-1; (e) JG-2; (f) JGb-1; (g) BCR-2.

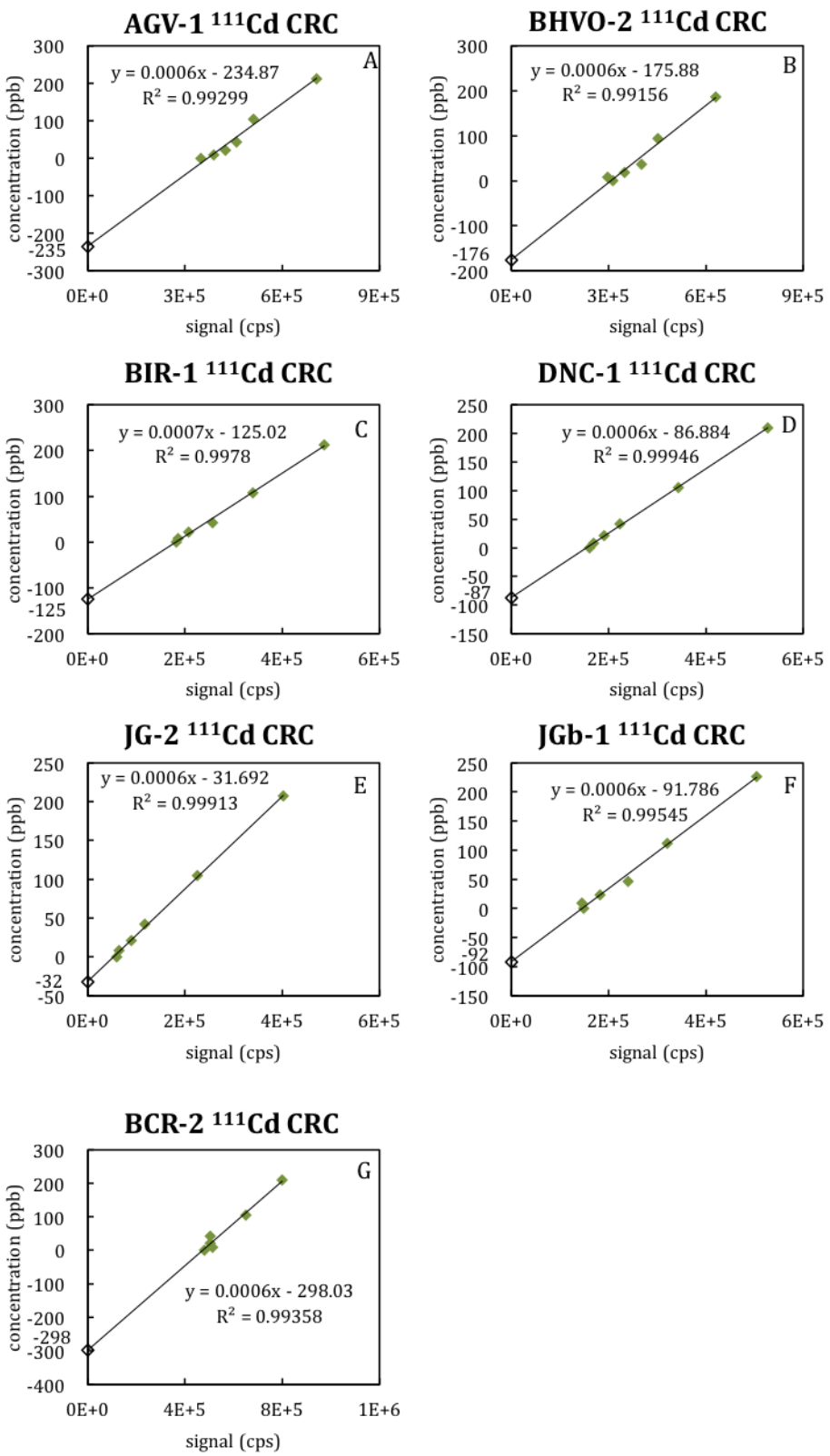

Figure 2.8. Standard addition calibration curves of ^{111}Cd in CRC mode of the standards: (A) AGV-1; (B) BHVO-2; (C) BIR-1; (D) DNC-1; (E) JG-2; (F) JGb-1; (G) BCR-2.

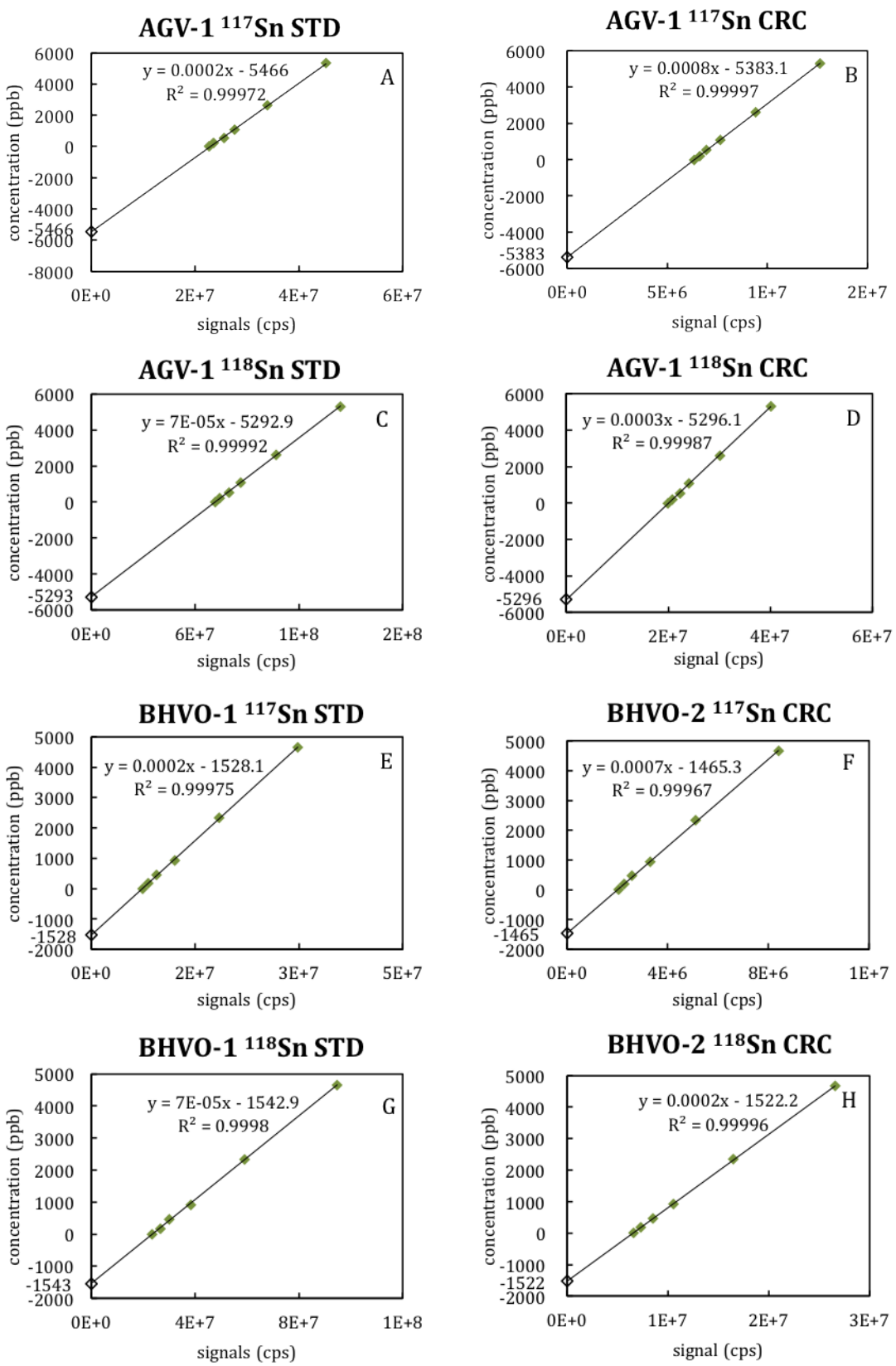

Figure 2.9. (Caption on Page 46)

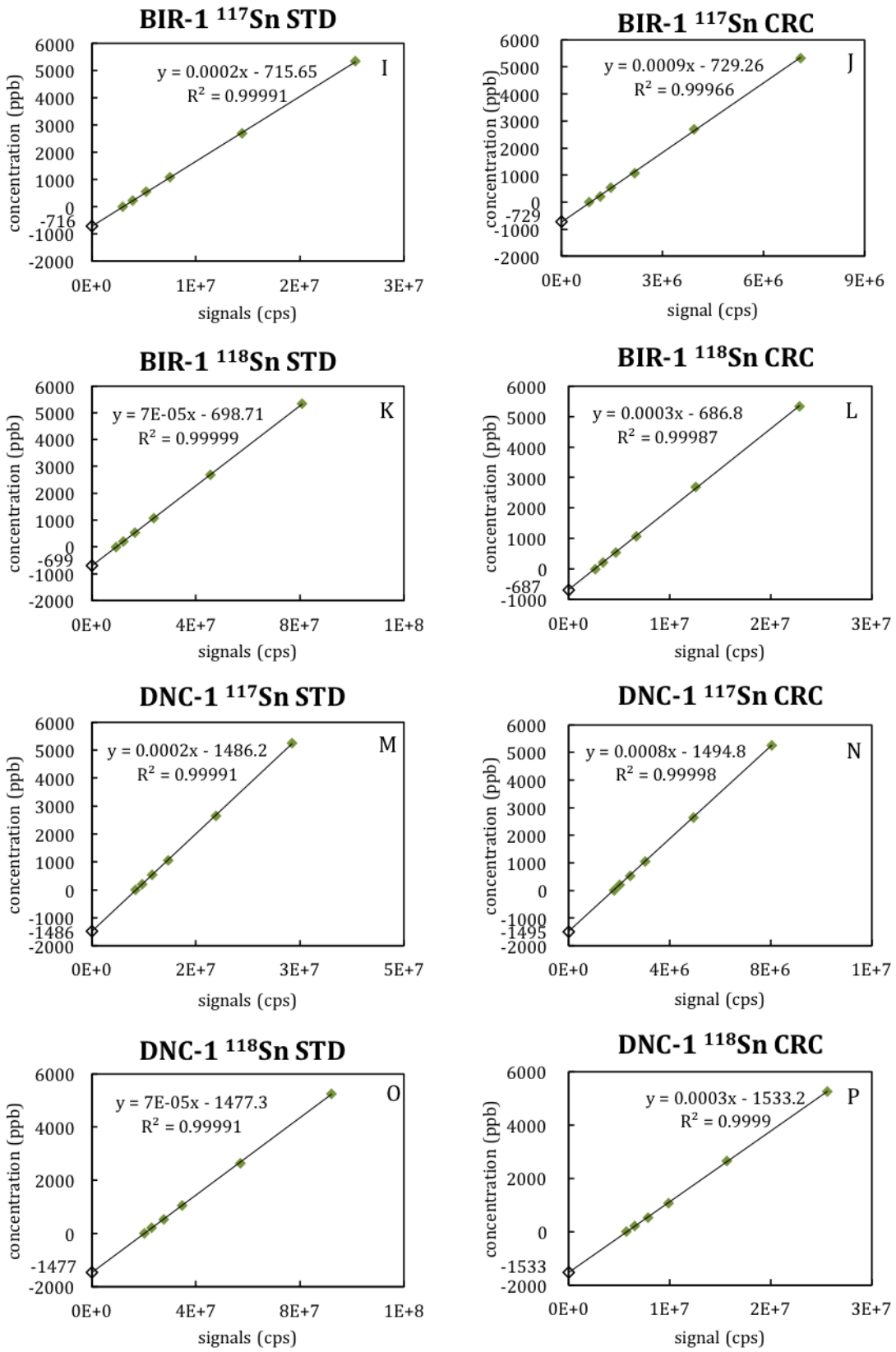

Figure 2.9. (Caption on Page 46)

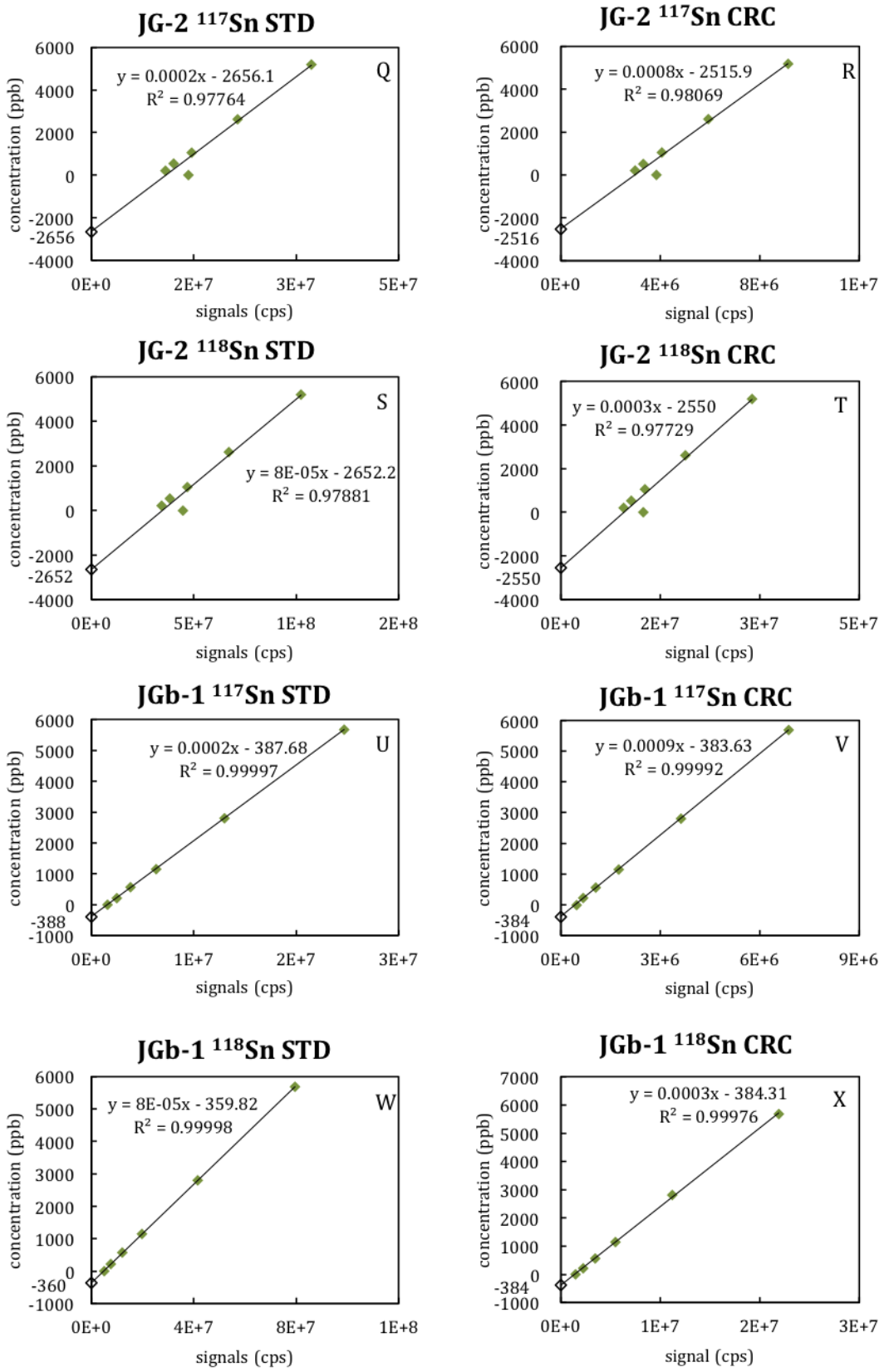

Figure 2.9. (Caption on Page 46)

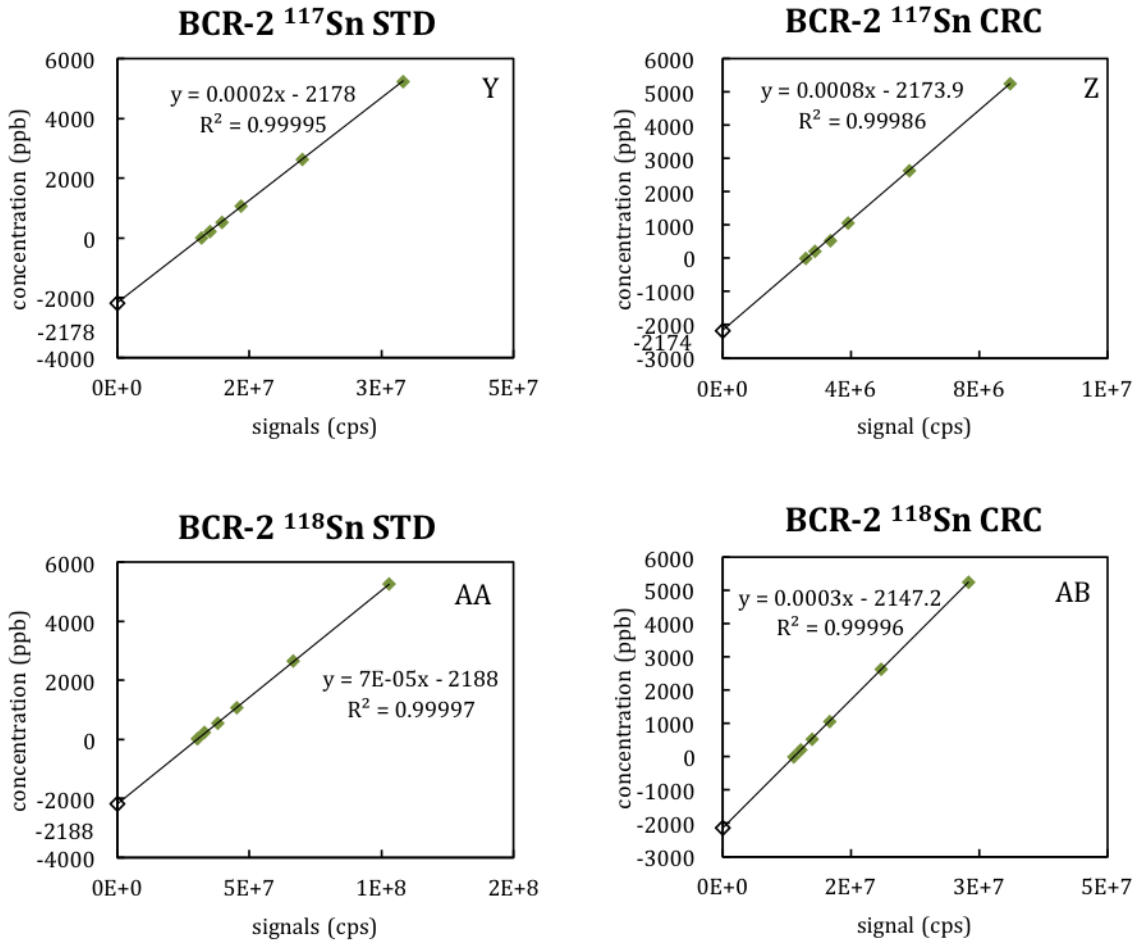

Figure 2.9. Standard addition calibration curves of ^{117}Sn and ^{118}Sn in both CRC and standard modes. (A) ^{117}Sn of AGV-1 in standard mode; (B) ^{117}Sn of AGV-1 in CRC mode; (C) ^{118}Sn of AGV-1 in standard mode; (D) ^{118}Sn of AGV-1 in CRC mode; (e) ^{117}Sn of BHVO-2 in standard mode; (F) ^{117}Sn of BHVO-2 in CRC mode; (G) ^{118}Sn of BHVO-2 in standard mode; (H) ^{118}Sn of BHVO-2 in CRC mode; (I) ^{117}Sn of BIR-1 in standard mode; (J) ^{117}Sn of BIR-1 in CRC mode; (K) ^{118}Sn of BIR-1 in standard mode; (L) ^{118}Sn of BIR-1 in CRC mode; (M) ^{117}Sn of DNC-1 in standard mode; (N) ^{117}Sn of DNC-1 in CRC mode; (O) ^{118}Sn of DNC-1 in standard mode; (P) ^{118}Sn of DNC-1 in CRC mode; (Q) ^{117}Sn of JG-2 in standard mode; (R) ^{117}Sn of JG-2 in CRC mode; (S) ^{118}Sn of JG-2 in standard mode; (T) ^{118}Sn of JG-2 in CRC mode; (U) ^{117}Sn of JGb-1 in standard mode; (V) ^{117}Sn of JGb-1 in CRC mode; (W) ^{118}Sn of JGb-1 in standard mode; (X) ^{118}Sn of JGb-1 in CRC mode; (Y) ^{117}Sn of BCR-2 in standard mode; (Z) ^{117}Sn of BCR-2 in CRC mode; (AA) ^{118}Sn of BCR-2 in standard mode; (AB) ^{118}Sn of BCR-2 in CRC mode. The calibration curves for JG-2 (Q-T) all show the offset of the sample without spike from the curves, which is probably resulted from contamination during sample preparation.

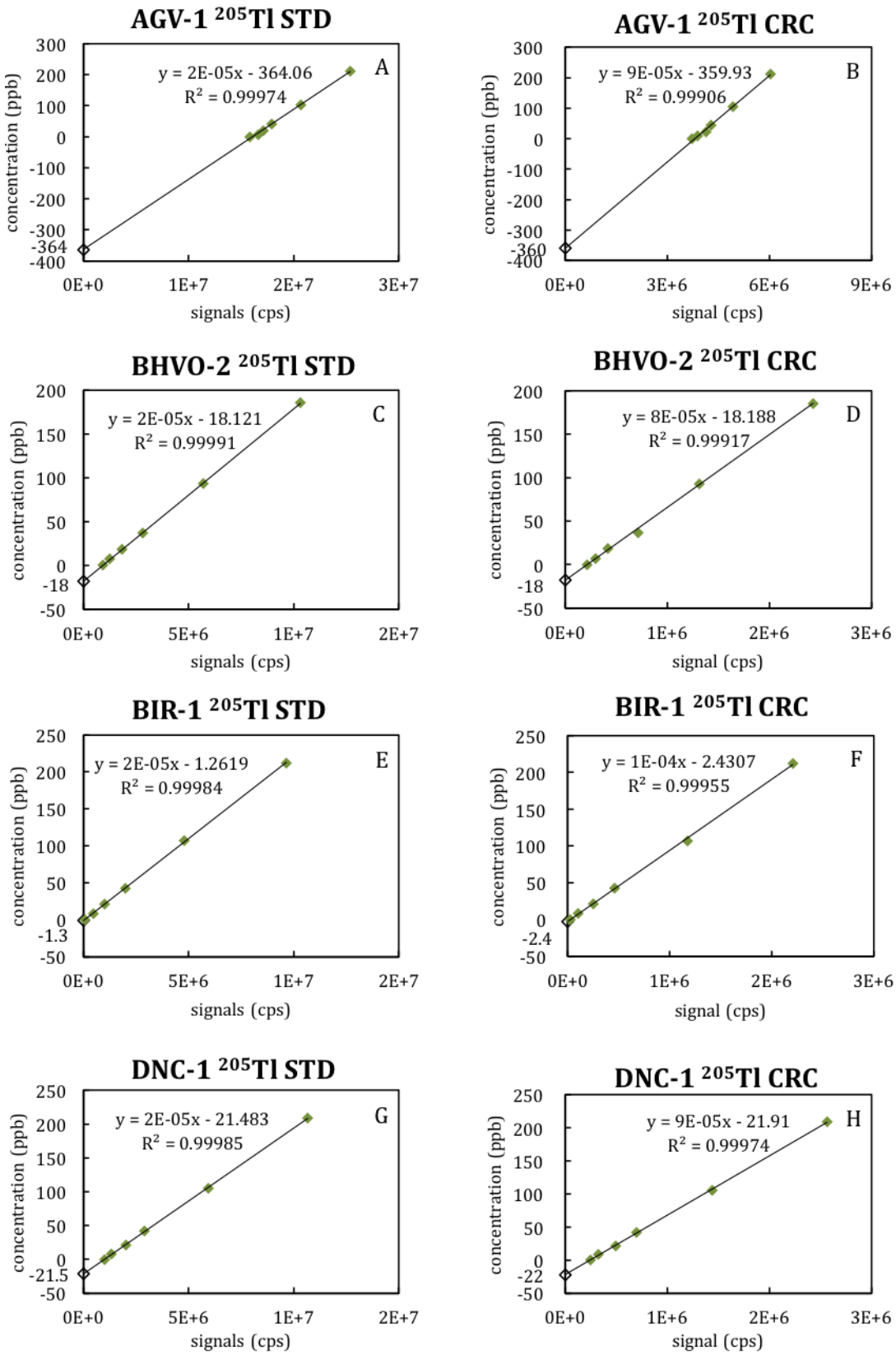

Figure 2.10. (Caption on following page)

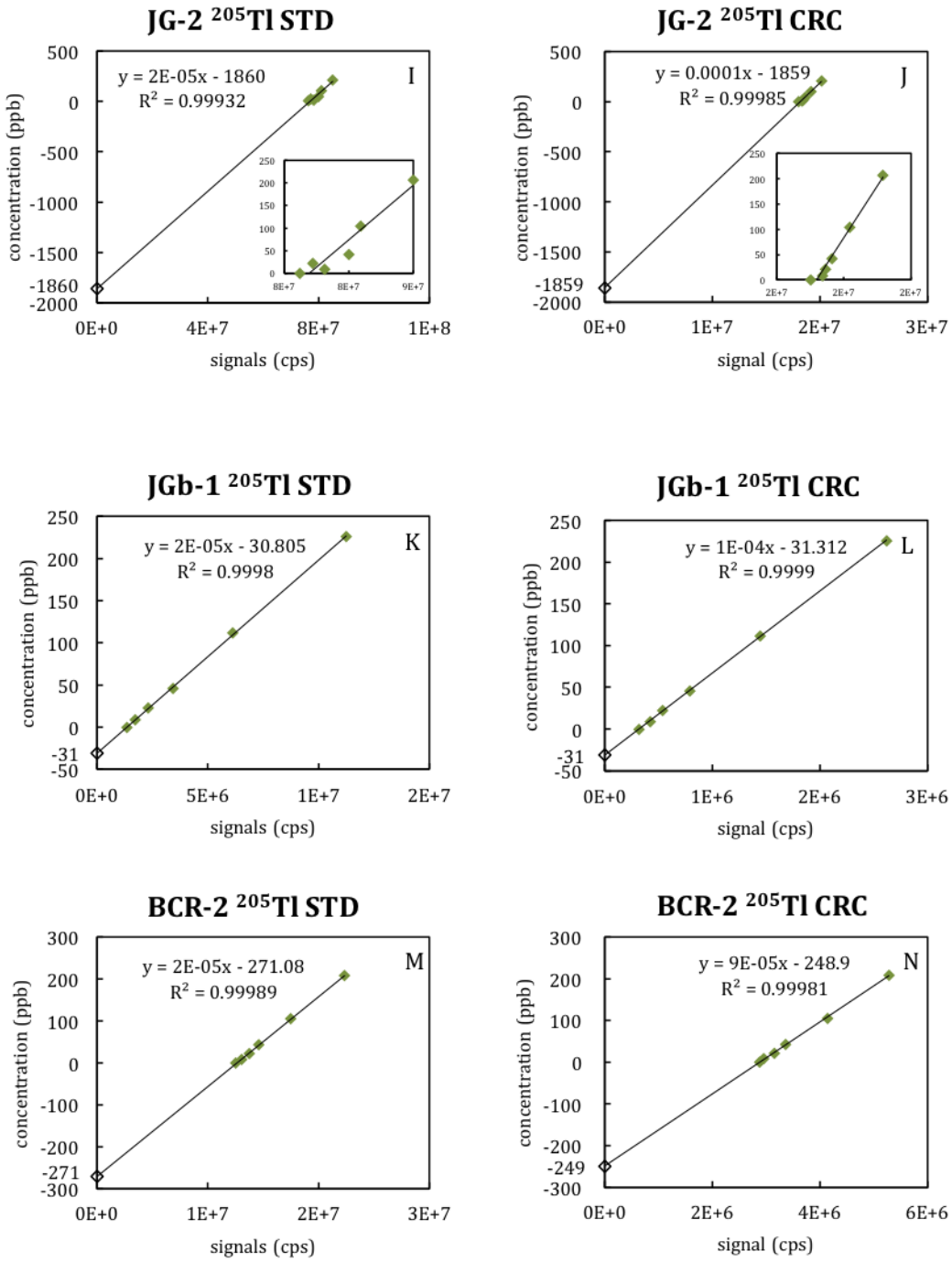

Figure 2.10. Standard addition calibration curves of ^{205}Tl in both CRC and standard modes in the seven reference materials. (A) AGV-1 in standard mode; (B) AGV-1 in CRC mode; (C) BHVO-2 in standard mode; (D) BHVO-2 in CRC mode; (E) BIR-1 in standard mode; (F) BIR-1 in CRC mode; (G) DNC-1 in standard mode; (H) DNC-1 in CRC mode; (I) JG-2 in standard mode; (J) JG-2 in CRC mode; (K) JGb-1 in standard mode; (L) JGb-1 in CRC mode; (M) BCR-2 in standard mode; (N) BCR-2 in CRC mode. The inset plots in (I) and (J) are the zoom-in plots for the calibration lines. Even though the extrapolation of the intercepts of AGV-1, standard mode and CRC gave the results of 1860 ppb and 1859 ppb, which means that the result is precise for calibrating the unknown samples.

Table 2.9. Selected chalcophile elements composition (ppm) in reference materials achieved by spike calibration.

	MODE/ Published	AGV-1	BHVO-2	BIR-1	DNC-1	JG-2	JGb-1	BCR-2	LOD
^{75}As	Standard	1.16	0.57	0.093	0.15	0.83	0.69	0.75	0.0099
	SE	±0.01	±0.01	±0.007	±0.02	±0.03	±0.01	±0.02	
As	Published	0.88-1.08	0.42-0.92	0.068-0.33	0.18	0.75-0.86	1.31	0.69-1.29	
^{95}Mo	Standard	2.25	3.37	0.049	0.13	0.18	0.24		0.033
	SE	±0.02	±0.08	±0.010	±0.02	±0.02	±0.01		
Mo	Published	2.7	1.9-6.05	0.037-0.13	0.05-0.19	0.22-0.4	0.33-0.82	248	
^{109}Ag	CRC	0.102	0.061	0.034	0.033	0.028	0.026	0.038	0.00093
	SE	±0.002	±0.005	±0.001	±0.002	±0.002	±0.003	±0.004	
Ag	Published	0.078	0.0445-1.54	0.0378 - 0.0435	0.027	0.017-0.02	0.025	0.07-1.6	
^{111}Cd	CRC	0.23	0.22	0.13	0.11	0.039	0.11	0.38	0.0038
	SE	±0.014	±0.012	±0.006	±0.003	±0.003	±0.008	±0.015	
Cd	Published	0.061-0.099	0.08-3.4	0.113	0.064-0.094	0.004-0.03	0.085-0.087	0.2-1.2	
^{117}Sn	Standard	5.47	1.53	0.72	1.49	2.66	0.39	2.18	0.011
	SE	±0.07	±0.04	±0.02	±0.03	±0.44	±0.01	±0.02	
^{117}Sn	CRC	5.38	1.47	0.73	1.50	2.52	0.38	2.17	0.0039
	SE	±0.02	±0.04	±0.05	±0.01	±0.41	±0.02	±0.04	
^{118}Sn	Standard	5.29	1.54	0.70	1.48	2.65	0.36	2.19	0.017
	SE	±0.04	±0.03	±0.009	±0.03	±0.43	±0.01	±0.02	
^{118}Sn	CRC	5.30	1.52	0.69	1.53	2.55	0.38	2.15	0.00018
	SE	±0.04	±0.02	±0.03	±0.03	±0.44	±0.04	±0.02	
Sn	Published	3.96-5.72	1.47-5.78	0.65	1-2.46	2.8	0.43-0.48	1.57-3.16	
^{205}Tl	Standard	0.36	0.018	0.001	0.021	1.86	0.031	0.27	0.00006
	SE	±0.003	±0.001	±0.001	±0.001	±0.02	±0.002	±0.002	
^{205}Tl	CRC	0.36	0.018	0.002	0.022	1.86	0.031	0.25	0.00074
	SE	±0.006	±0.003	±0.002	±0.002	±0.01	±0.001	±0.002	
Tl	Published	0.29-0.44	0.011-0.08	0.001-0.005	0.0207 -0.025	1.56	0.023-0.1	0.2-0.362	

Note:
Published: published data by GeoRem
LOD: limit of detection; detail of estimation is described in Section 2.5.3.
SE: standard error of intercept calculated using the function $\sqrt{\frac{1}{n-2}\{\sum(y-\overline{y})^2 - \frac{[\sum(x-\overline{x})(y-\overline{y})]^2}{\sum(x-\overline{x})^2}\}}$. n is the number of spikes (n=6), y is the spike concentration; $\overline{y}$ is the spike concentration calculated by the regression line; x is the the signal of spike; $\overline{x}$ is the signal of spike calculated by the regression line.

The concentrations of elements of interests in reference materials determined with standard addition method in this study are mostly in the range of published data

by GeoRem (<10% difference; Table 2.9). The results of BHVO-2 agree with the published data. However, there are some elements concentrations determined in this study have large difference. The results of AGV-1 show 18% lower in Mo concentration, 27% higher in Ag concentration, and 80% higher in Cd concentration than the published data. The results of BIR-1 show 11% lower in Ag concentration and 14% higher in Cd concentration than the published data. The results of DNC-1 show 18% lower in As concentration, 20% higher in Ag concentration, and 16% higher in Cd concentration than the published data. The results of JG-2 show 20% lower in Mo concentration, 33% higher in Ag concentration, 26% higher in Cd concentration, and 18% higher in Tl concentration than the published data. The results of JGb-1 show 62% lower in As concentration, 31% lower in Mo concentration, and 23% higher in Cd concentration than the published data. BCR-2 has 59% higher Ag concentration determined by this study than the published data.

2.5.3. Detection limits

The detection limit is defined as three times the standard deviation of the procedural blanks (Table 2.9). For most elements considered here the detection limits are from <1% to ~10% of the concentrations determined in the reference material. The detection limit of ^{95}Mo in BIR-1 analyzed in standard is 67% of the results of BIR-1. The detection limit of ^{205}Tl in BIR-1 analyzed in CRC mode is 37% of the results of BIR-1.

Chapter 3

3. STUDY AREA AND SAMPLE SUITE

3.1. Tectonic Setting and Previous Studies at Pito Deep

The samples studied here were formed at the East Pacific Rise and are exposed by the Pito Deep rift. The Pito Deep Rift is located at the northeast corner of the Easter Microplate, and is propagating into the old Nazca plate lithosphere (Fig. 3.1 A; Francheteau et al., 1988; Martinez et al., 1991; Naar and Hey, 1991; Naar et al., 1991). The rift is caused by slow extension that started ~1 My ago at a rate of ~10 mm/year (Karson et al., 2005), exposing ~4 km of vertical relief of the mid- to upper-crustal sections formed at the fast spreading (~142 mm/year, full rate) southern East Pacific Rise (EPR) ~3 My ago (Naar and Hey 1991; Hékinian et al., 1996; Hey et al., 2004). The exposed crustal section consists of basaltic lavas, sheeted dikes, and gabbroic rocks (Constantin et al. 1995; Hékinian et al. 1996; Francheteau et al. 1988; Karson et al. 2005).

In-depth studies of two areas (Area A and Area B; Fig. 3.1) were conducted during the R/V Atlantis AT11-23 cruise, using the Jason II ROV and the Alvin submersible for mapping and sampling (Karson et al., 2005). Area A exposes somewhat shallower level crustal material along the northern wall of the Pito Deep Rift, and Area B exposes somewhat deeper crustal levels to the southeast (Fig. 3.1 B). The areas are each ~5 km wide and are separated by ~14 km. The basaltic lava unit makes up the upper 300-500 m of each crustal section (Fig. 3.2). The lava-dike transition zone consists of 20-80% lavas mixed with dikes, with a vertical thickness of 80-200 m (Hayman and Karson, 2009; Heft et al., 2008). The underlying sheeted

dike complex ranges in thickness from 600 to 1000 m (Karson et al., 2005; Heft et al., 2008). Outcrops of gabbroic rocks are exposed over a depth range of ~ 900 m in Area B extending to water depths of more than 4000 m (Perk et al., 2007). Steeply dipping fault zones were found in a few places within the upper crust (Hayman and Karson, 2009). The fault zones feature intensely altered fault gouge cut by numerous quartz veins reflecting localized hydrothermal fluid flow (Barker et al., 2010a). Some of the fault zones are cut by later dikes and therefore probably formed near the spreading axis. Others appear to lack high-temperature mineralization and cross cutting dikes and may have formed or been reactivated during rifting in the area (Karson et al., 2005). A fault zone studied here is described separately in Section 3.1.1.

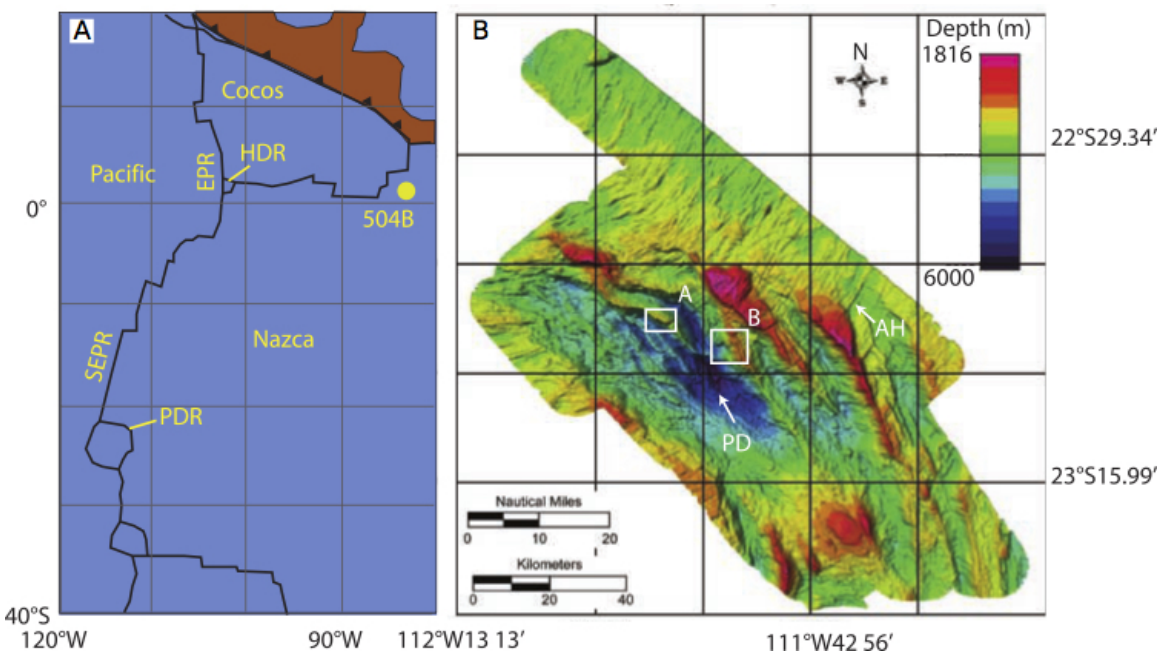

Figure 3.1. (A) The Pito Deep Rift (PDR) is located close to the Southern East Pacific Rise (SEPR). (B) 3-D bathymetry of the PDR showing the locations of the two sampling regions Area A and B. The Pito Deep (deep blue area in centre) is more than 6 km deep, and bounded by rift walls. Modified after Hayman and Karson (2009).

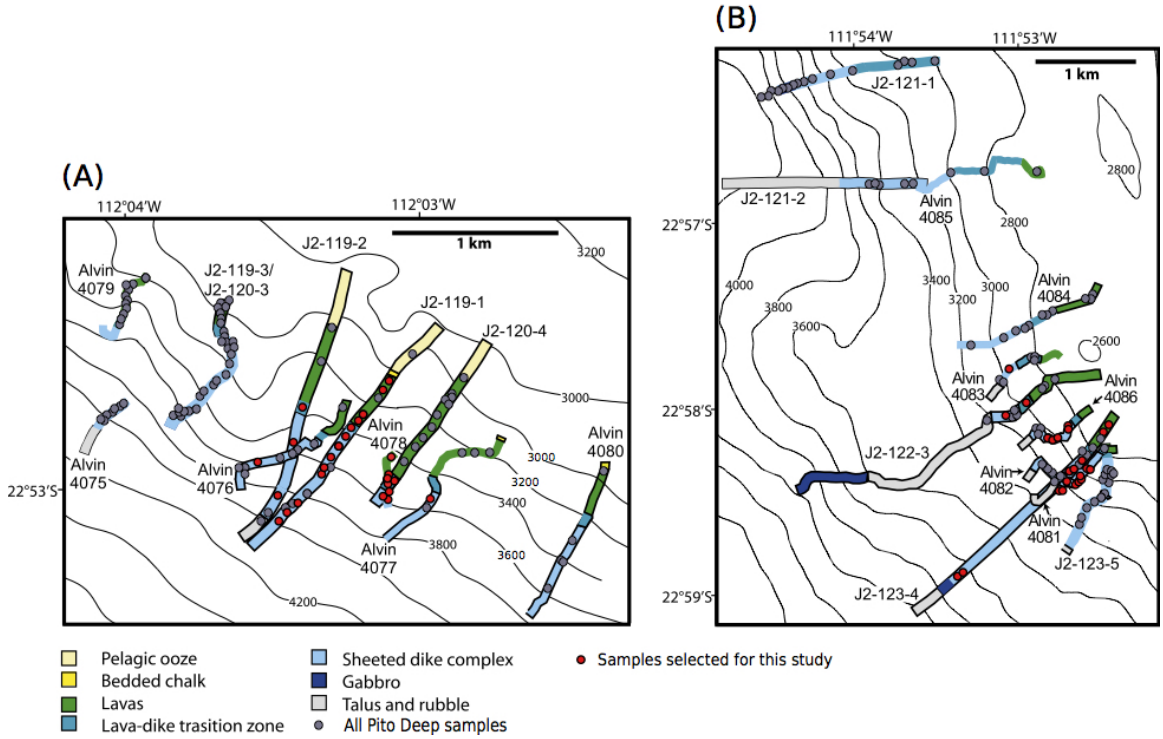

Figure 3.2. Jason II and Alvin dive tracks from research cruise AT11-23 of the R/V Atlantis in February 2005 in study areas Area A (A) and Area B (B) showing colour coded lithologic boundaries (Karson et al., 2005). Jason II dives begin with J2, followed by the lowering number and transect number. Alvin dives are numbered sequentially as only one transect was completed for each dive. Depths are meters below sea level (mbsl); contour intervals are 200m. Adapted from Heft et al., 2008.

The 2005 Alvin and Jason II expedition collected 435 samples in situ from outcrops of basaltic lavas, sheeted dikes, and massive gabbro rocks, as well as fault breccias. Previous studies showed that the majority of the Pito Deep samples are incompatible-element-depleted normal mid-ocean ridge basalts (N-MORB; $(La/Sm)_N < 1.0$), with no major difference between Area A or Area B (Heft et al., 2008; Pollock et al., 2009). The compositions of Pito Deep samples overlap those of other southern EPR basalts and Hess Deep samples (Pollock et al., 2009).

The alteration of the dike complex is heterogeneous with amphibole, the dominant phase replacing clinopyroxene, but with chlorite-rich dikes distributed

intermittently along dive tracks (Heft et al., 2008). It is interpreted that the peak alteration temperatures varied from <300° to > 450 °C, with no systematic depth or spatial trends (Heft et al., 2008). Dikes locally show substantial metal mobility, with Zn, Cu, and Pb depletion, indicating reaction with high-temperature (≥400 °C) fluids throughout the dike complex (Heft et al., 2008; Zoeller, 2014). The heterogeneity of alteration, and the lack of any systematic change of alteration temperature with depth in dikes, is also observed within the sheeted dike complexes at Hess Deep tectonic window (Gillis et al., 2001). However, there are systematic changes of alteration with depth in the drill cores from Hole 504B and Hole 1256D (Alt et al., 1986; Alt et al., 2010), which represent a smaller time interval of alteration than tectonic windows (<5 to 30 ka time interval for Pito Deep).

The Sr-isotopic composition of samples of the oceanic crust provide quantitative information about the amount of hydrothermal fluid that the crust has reacted with. Studies of the Sr isotopic composition of the Pito Deep sheeted dikes show that the average $^{87}Sr/^{86}Sr$ ranging from 0.70252 to 0.70295 relative to a protolith with $^{87}Sr/^{86}Sr$ of ~0.7024 (Barker et al., 2008). Sr-isotope profiles throughout the sheeted dike complex show no depth variation, suggesting that fluid flux flow through the sheeted dike complex is uniform (Barker et al., 2008). The extent of Sr-isotopic exchange between the crust and hydrothermal fluid is similar at Pito Deep to in ODP Hole 504B and the Hess Deep tectonic window (Barker et al., 2008).

The sulphur concentrations, $\delta^{34}S$, and $Fe_2O_3/Fe_2O_3^{Total}$ in the Pito Deep samples were studied to investigated the behavior of seawater sulphate in the sheeted dikes

(Barker et al., 2010b). A loss of 400-550 ppm of S from the sheeted dikes, and a minimal increase (1.5‰) of $\delta^{34}S$, indicating that most seawater SO_4^{2-} precipitates as anhydrite when the temperature of downwelling fluids increases to > 120 °C, and hydrothermal fluids must be enriched in H_2S after reaction with the sheeted dikes. Because Sr would partition into the anhydrite fluid fluxes calculated from the Sr-isotopic composition of the crust are minimum values. Barker et al., (2008) estimate a minimum fluid flux of $\sim 3 \times 10^6$ kg/m^{-2} would pass through the sheeted dikes to generate the observed Sr-isotope values.

3.1.1. Previous studies metal sulphides and the distribution of Cu, Zn and Pb in Pito Deep

Petrographic observation of the dike samples from the Pito Deep shows that the dominant metal-sulphides are pyrite and chalcopyrite, with trace amount of pyrrhotite (Zoeller, 2014). Pyrite and chalcopyrite range from <0.05 mm up to 2 mm, and chalcopyrite is commonly finer grained than pyrite (Zoeller, 2014). Pyrite occurs as a primary and secondary phase in the groundmass, or as a void-filling phase in the sheeted dike samples (Zoeller, 2014). Chalcopyrite is present only as a secondary or void-filling phase in sheeted dike samples (Zoeller, 2014).

Bulk rock composition of sheeted dikes display local metal mobility (Heft et al., 2008; Zoeller, 2014). Copper is depleted in the dike samples in Areas A and B and Cu-depleted dikes are distributed at all depth without systematic change (Heft et al., 2008; Zoeller, 2014). Zn- and Pb-depleted dikes (~90% and ~70% respectively) are more common than Cu-depleted dikes in Pito Deep (Heft et al., 2008; Zoeller, 2014).

The distribution of Cu- and Zn-depleted dikes indicates reaction with high-temperature (>400°C) fluids throughout the dike complex (Heft et al., 2008).

The LA-ICP-MS results of pyrite and chalcopyrite from Zoeller (2014) show that all Pb is below 0.1 wt%. The typical range of Zn and Cu in pyrite minerals is 50-500 ppm and 100-500 ppm, respectively. It is suggested that the increased concentrations of Zn and Cu may be possibly due to inclusions of sphalerite or chalcopyrite within the pyrite grains rather than partition into pyrite (Zoeller, 2014). Copper ranges from 32.8 wt% to 34.9 wt%, and the typical range of Zn in chalcopyrite minerals is 0-400 ppm. Zoeller (2014) suggested that the variation of Zn in chalcopyrite is possibly due to the solid solution of ZnS in $CuFeS_2$.

3.1.2. Previous studies on the fault zone in Area A

Fault zones are commonly hypothesized to provide channels to focus upflowing fluid at shallow levels at fast-spreading ridges (e.g., Haymon et al., 1991). Several fault zones in Pito Deep were studied previously (Hayman and Karson, 2009; Barker et al., 2010a) and it was suggested that the fault zones were pathways for both hydrothermal fluids and downwelling seawater. Therefore, the rock samples from fault zones are also expected to contain sulphide precipitations from hydrothermal fluid that cooled due to mixing with seawater.

A fault zone identified on Jason Transect 1 in Area A was more comprehensively mapped during Alvin dive 4078 (Fig. 3.3; Hayman and Karson, 2009). The main fault in this ~40 m-wide fault zone (indicating by the red line in Fig. 3.3) contains a continuous vein enriched in hydrothermal minerals, such as matrix and vein chlorite,

prominent veins of quartz, and grains of sulphides and oxides (Hayman and Karson, 2009). The fault zone locates at the depth of the dike-transition zone boundary. Barker et al. (2010a) analyzed the Ti content of quartz, and calculated the crystallization temperatures of quartz was 325-440 °C. The fluids passing through this fault zone had a temperature similar to those of black-smoker vent fluids (Barker et al., 2010a). However, the $^{87}Sr/^{86}Sr$ ratios in fault breccias are higher than in average vent fluids, which suggests mixing between high-temperature upwelling fluids and seawater-like fluids within the fault zone (Barker et al., 2010a). In order to maintain the high temperature of fluids, the ratio of high temperature to cool fluids must have been around 3:1-7:1 (Barker et al., 2010b). Samples from this fault zone are used in Chapter 4 to test for the evidence of chalcophile elements enrichment during fluid mixing.

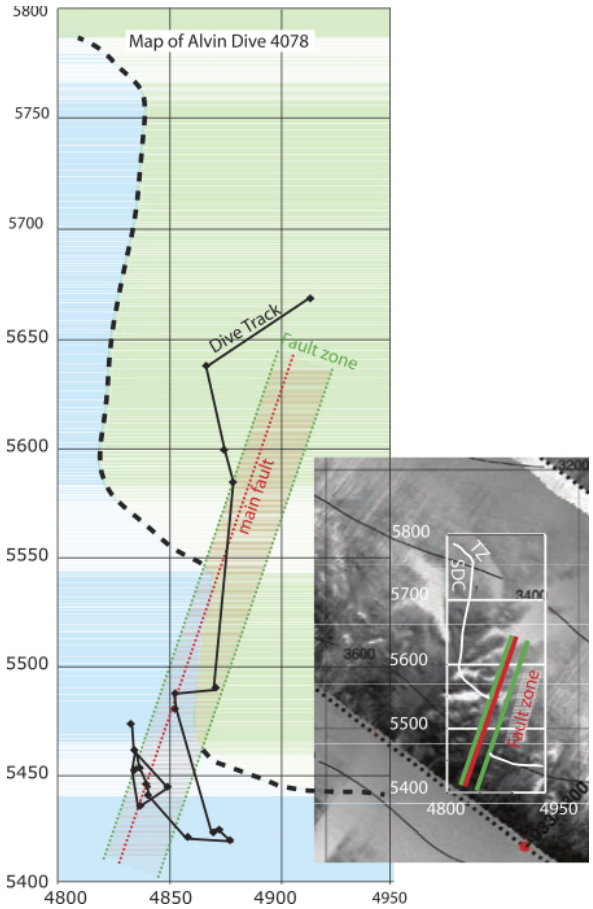

Figure 3.3. Geologic map and side scan sonar image of the Alvin Dive 4078 area in X and Y axis (modified from Hayman and Karson, 2009). The fault zone represented by the shaded area has a prominent "main fault" (red line). The fault zone cuts across the sheeted dike complex (SDC, blue) and the transition zone (TZ, green) at a depth of between ~3500 mbsl and ~3700 mbsl.

3.2. Sample Selection and Description

To track the chalcophile elements behaviour during hydrothermal circulation, samples were selected from sheeted dike complex, transition zone, and lava unit. Thus both the leaching and the precipitation of chalcophile elements in the oceanic crust could be traced.

Samples for this study were selected to provide a profile through the sheeted dike complex, the lava-dike transition zone, and the lava unit in both Area A and Area

B, from the samples recovered from the cruise AT11-23 of the R/V Atlantis in February 2005 (Figure 3.2, solid red circles). The samples were selected to maximize the available S content, S isotope, and $^{87}Sr/^{86}Sr$ data from previous studies (Barker et al., 2010a and 2010b). The samples were selected to cover a minimal lateral width, and a maximal depth into the sheeted dikes. In Area A, the samples selected for this study are from six adjacent and overlapping dives provided lateral coverage of ~900 m and a depth range of ~1000 m. The fault zone in Area A is an important area for studying mixing and precipitation processes, therefore, samples from fault zone were also included in samples selected from Area A. In Area B, the samples selected are from six adjacent and overlapping dives providing lateral coverage of ~1300 m at near-constant depth within 400 m below the lava-dike transition (mbld) and a depth range of ~1200 m. There is a gap in sampling between 450 and 1050 mbld in Area B transect J2-123-4 due to talus concealing the exposure (Karson et al., 2005).

Fourteen dike samples, three transition zone samples, and two lava samples, as well as nine samples from a fault zone near the lava-dike transition (including five fault breccias and four dike samples) were selected from Area A for analysis in this study. Twenty dike samples, two transition zone samples, and two lava samples were selected from Area B for analysis. The selected samples have previously been analyzed for major elements, trace elements, in some cases for $^{87}Sr/^{86}Sr$ (36 samples of total 52 samples selected), sulphur content (31 samples of 52 samples selected), and $\delta^{34}S$ values (15 samples of 52 samples selected) (Pollock et al., 2009; Barker et al., 2008; Barker et al., 2010a and 2010b; Heft et al., 2008). Previous analyses of base metal (Zn, Cu, Pb) concentrations were used to select samples that are enriched,

depleted and similar to N-MORB for analysis (Fig. 3.4 A, B, and C). Additionally, samples were selected to provide a depth profile for the change in trace metals through the crust. The fault zone in Area A provides a focused channel for down-welling seawater to mix with hydrothermal fluids (Barker et al., 2010a), therefore, samples showing relative higher $^{87}Sr/^{86}Sr$ (Barker et al., 2010a) than background dikes were also selected from the fault zone (Fig. 3.4 D).

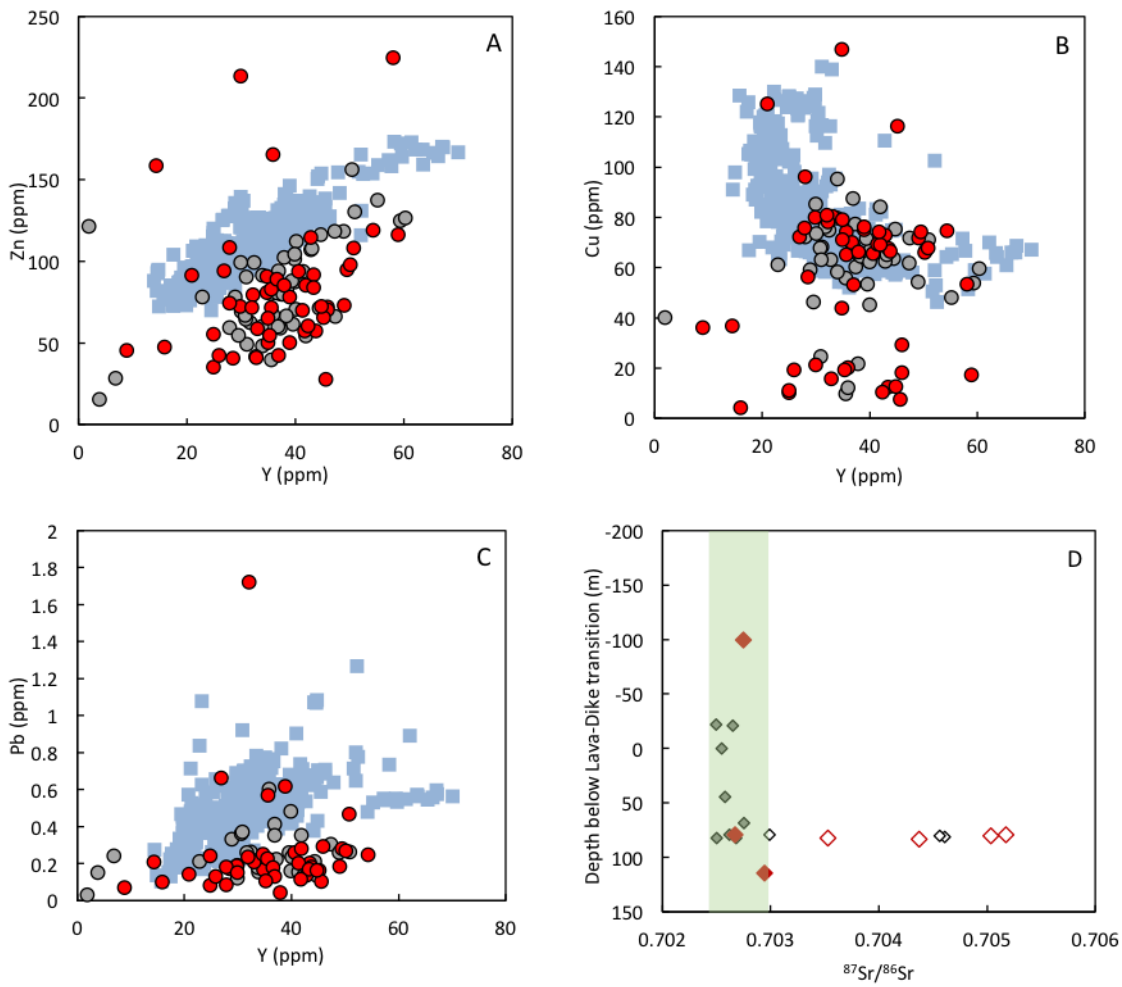

Figure 3.4. (Caption on following page)

Figure 3.4. (A)-(C): Zn, Cu, and Pb concentrations (ppm) versus Y (ppm) for fresh MORB glasses (Jenner and O'Neil, 2012; solid blue squares) and Pito Deep samples (samples selected for this study: solid red circles; not selected: solid grey circles). The data for Zn, Cu, Pb are from Pollock et al. (2009), Heft et al. (2008), Barker et al. (2008), and Barker et al. (2010a). In fresh MORB glasses, Pb and Zn have positive correlation with Y, whereas Cu shows negative correlation with Y. This is because that Cu is more incompatible than Pb and Zn (Wang and Becker, 2015). (D) $^{87}Sr/^{86}Sr$ versus the depth below the lava-dike transition (m) for Pito Deep samples in the fault zone studied (samples selected for this study: red solid diamonds are wall-rock dikes from the fault zone, and red open diamonds are the fault breccias; not selected: grey solid diamonds are wall-rock dikes from the fault zone, and black open diamonds are the fault breccias). Note that there are nine fault zone samples selected for this study but only seven of them have previously been analyzed for $^{87}Sr/^{86}Sr$. The green shaded area in (D) represents the $^{87}Sr/^{86}Sr$ for the background dikes in Pito Deep. Sr-isotope data are from Barker et al. (2010a).

Chapter 4

4. RESULTS AND DISCUSSION

Understanding the distribution of chalcophile elements within the upper oceanic crust (dike complexes, lava-dike transition zone, and lava unit) is important, as it provides geological insights into the conditions of fluid and rock interactions before hydrothermal fluids vent to the ocean bottom (Fig 1.6; Section 1.4.3). The goal of this chapter is to quantify the gains and losses of chalcophile elements in the sheeted dikes, lava-dike transition zone, and lavas at Pito Deep.

The analytical techniques and the data processing procedures are described in Section 4.1. In order to determine the gains and losses of the elements studied relative to fresh basalts, a filtered global MORB glass database (Jenner and O'Neil, 2012) is used for comparison and calculation of changes in element concentrations (Section 4.2.1). The distribution of the elements of interest in the crust exposed at Pito Deep is discussed in Section 4.2.2. The fault zone in Area A has been suggested to have provided a pathway for fluid mixing (Barker et al., 2010a), thus, the fault zone samples are discussed separately (Section 4.3).

The sulphide minerals that contain the elements of interest are numerous. For example, chalcopyrite, chalcocite, bornite and many more Cu dominant sulphides could form in hydrothermal systems. For simplicity, this study describes Zn, Cu, Fe, and Pb dominated sulphides using the terms sphalerite, chalcopyrite, pyrite, and galena respectively.

4.1. Sample Analysis and Data Reduction

Powdered rock samples were prepared following the steps described in Appendix C. Due to limited sample size, only ~50 mg of sample 4078-1728 was weighed instead of ~100 mg. This was dissolved in half amounts of acids in each step. Each powdered sample was dissolved using a standard HF-HNO_3 approach and diluted by a factor of ~1:1000 in 2% HNO_3 solution for analysis. The elements of interest were analyzed using a Thermo X-Series II ICP-MS at the University of Victoria following the approach of Eggins et al. (1997), and the operational parameters were as described in Chapter 2 (Table 2.4). Single element solutions of Zr, Nb, Na, K and P were analyzed at the end of the analytical sessions to determine correction factors for molecular interferences (Section 2.2.2). A drift solution was made out of a mixture of sample solutions and was measured after every eight samples to monitor instrument drift. The reference materials AGV-1, BCR-2, BIR-1a, BHVO-2, DNC-1, JG-2, JGb-1 were analyzed for calibration at the start and end of analytical sessions. Six procedure blanks were prepared following the same steps of sample preparing, and they were analyzed during the analytical sessions to quantify the blank. Data reduction follows the steps described in Appendix D, including the steps of internal standardization, blank correction, interference correction, dilution factor correction, secondary drift correction, and calibration. Raw data and data reduction process of the samples are included in Appendix F.

The precision of the data for each element was calculated using the variability in the drift solution which was analyzed 21 times during the run. The standard deviation of element x in drift solution (σ_x) is

$$\sigma_x = \sqrt{\frac{1}{n-1}\Sigma_1^n (x_i - \overline{x})^2} \qquad \textit{Equation 4.1}$$

where n is the number (21) of analyses of the drift solution; x_i is the measured concentration of element x in each run of the drift solution; $\overline{x}$ is the average of the measured concentrations of element x in all analyses of the drift solution.

The detection limits of the elements studied were quantified as three times the standard deviations of the blank:

$$x_{LOD} = 3\sigma_{xPBK} \qquad \textit{Equation 4.2}$$

where x_{LOD} is the limit of detection of element x; σ_{xPBK} is the standard deviation of concentration of element x in procedure blanks (Olesik, 2014). Silver concentrations in four samples are below the detection limit but the rest of the elements analyzed are all above the detection limit in all samples. The precision and limit of detection for each element are reported in Table 4.1. The accuracy of the analyses in this study is assessed by comparison with the analyses of the same Pito Deep samples (for Zn, Cu, Yb, and Pb) in other studies (Pollock et al., 2009; Heft et al., 2008; Barker et al., 2008 and 2010a) in Appendix F.

Table 4.1. Precision (2σ) and limit of detection (LOD) in this study.

Element	Co	Cu	Zn	Ga	Ge	As	Mo	Ag	Cd	Sn	Sb	Yb	Tl	Pb
2σ (ppm)	1.2	1.1	3.7	0.23	0.079	0.058	0.09	0.005	0.024	0.037	0.006	0.033	0.005	0.16
LOD (ppb)	2.6	19	624	0.7	4.1	54	8.6	1.1	0.8	6.1	0.7	0.1	0.1	3.2

4.2. The Bulk Rock Compositions of Interest

4.2.1. Assessment of fresh basalt composition and the change of concentration in Pito Deep samples

To calculate the change of concentration of elements due to hydrothermal processes in the Pito Deep samples, a fresh basalt composition is needed. A global MORB glass database analyzed by Jenner and O'Neill (2012) contained all the elements of interest in this study, thus it is used in this study to define the fresh basalt composition. To identify suitable data to compare with the Pito Deep samples, the following criteria were used to filter the database: (1) only data from mid-ocean ridge spreading centers were used; and (2) only data with a chondrite-normalized La/Sm ratio in the range 0.3 to 1.56, which is the La/Sm range of Pito Deep fresh basalts (Pollock, 2007) were used. The final filtered database consisted of 370 MORB glass samples.

To constrain the fresh basalt concentrations, calculation of how the chalcophile elements and Mo vary with differentiation of the parental magma is needed. Following the approach of Jowitt et al. (2012), the filtered glass database from Jenner and O'Neil (2012) was used to define magmatic differentiation trends by plotting Yb against the elements of interest. As Yb is an immobile element it is assumed that its concentration has not changed from the fresh rock value. These trends were fit to a least squares regression in the form of a power law curve:

$$M_c = A\,(Yb)^B \qquad \textit{Equation 4.3}$$

where M_c is the calculated element concentration (ppm) at a given concentration of Yb, and A and B are regression coefficients defined by the filtered Jenner and O'Neill

dataset. The fit of the data to a differentiation trend was assessed by determining root mean square of deviations between the model and data:

$$RMSD = \sqrt{[\Sigma(M_c - M_f)^2/n} \qquad \textit{Equation 4.4}$$

where M_f is the measured concentrations in the MORB glass sample, and n is the number of samples used to define the model.

The changes in concentration of an element in a given sample (ΔM) is as:

$$\Delta M = M_{PD} - M_c \qquad \textit{Equation 4.5}$$

where M_{PD} is the measured concentration of element in a sample from Pito Deep measured in this study. Values that fall within the range of uncertainty of MORB glass (Equation 4.4) are assumed to show no change, and the values fall outside of this range are identified as enrichment (+ ΔM) and depletion (– ΔM).

4.2.2. The distribution of the elements of interest in Pito Deep

The concentrations of the elements Co, Ni, As, Cu, Zn, Ga, Ge, Y, Zr, Nb, Mo, Ag, Cd, Sn, Sb, Ba, La, Ce, Yb, Tl, and Pb in the Pito Deep samples analyzed in this study are reported in Appendix F. The fault breccia samples 4078-1728 and 4078-1800 show a significantly dilution effect due to silica precipitation leading to high SiO_2 contents (83 and 72 w.t.% respectively; Barker et al., 2010a). Assuming that dilution resulted from SiO_2 addition only, the "undiluted" composition was calculated as:

$$C_X^i = C_X^f \times \frac{100 - C_{SiO_2}^i}{100 - C_{SiO_2}^f} \qquad \textit{Equation 4.6}$$

where $C_{SiO_2}^{i}$ is the initial weight percentage of SiO_2; $C_{SiO_2}^{f}$ is the weight percentage of SiO_2 measured from the sample; C_X^i is the concentration (ppm) of element X before the silica addition; C_X^f is the concentration (ppm) of element X measured from the sample. The average SiO_2 content of the Pito Deep samples that analyzed is 50.8% (Pollock et al., 2009), which is assumed as the value of $C_{SiO_2}^{i}$.

In the following sections the data are described based on the behaviour of different groups of elements. Compared to MORB glasses (Jenner and O'Neil, 2012), Co, Ga, Ge, and Sn show no change or are slightly depleted (discussed in 4.2.2.1); Zn, Cu, Cd, As, Ag, Pb, and Tl show variable depletions and enrichments (discussed in Section 4.2.2.2); Mo and Sb show large enrichments in dike samples (Section 4.2.2.3).

4.2.2.1. Cobalt, gallium, germanium, and tin

The elements Co, Ga, Ge and Sn were relatively immobile during alteration of the Pito Deep samples (Fig. 4.1). Previous studies show that the average concentrations of Co, Ga, and Ge in high-temperature (>300 °C) vent fluids from the EPR are 25 ppb, 2.6 ppb, and 10.8 ppb respectively (Table 4.1; Von Damm et al., 1985; Von Damm, 1995; Metz and Trefry, 2000; Seyfried et al., 2003). Comparing to MORB glass concentrations (Jenner and O'Neill, 2012) of Co (~50 ppm), Ga (14-22 ppm), and Ge (1.2-1.8 ppm), the vent fluids have very low concentrations of these elements. This indicates that the elements Co, Ga and Ge are relative immobile in oceanic hydrothermal systems. The bulk rock analyses of basalt samples from Hole 504B (e.g., Alt and Emmermann, 1985; Alt et al., 1989) and Hess Deep (Stewart et al., 2002) show

similar bulk rock concentrations of Co and Ga to the concentrations of both elements in Pito Deep.

The bulk rock Co concentration of the Pito Deep samples is slightly lower than (or similar to) MORB glass (Fig. 4.1 A). The similar immobile character of Co is also observed in Hole 504B, where the Co content is relatively constant in the upper oceanic crust (Alt and Emmermann, 1985). Although previous studies suggested that chalcopyrite solubility controls Co abundances (Section 1.3.2; Fouquet et al., 1988; Hannington et al., 1991; Tivey et al., 1995; Trefry et al., 1994; Metz and Trefry, 2000), the samples of this study show Co is not mobile during hydrothermal circulation. The immobility of Co in the Pito Deep may be due to local redistribution of Co into silicate minerals within the sheeted dike complex rather than Co being substantially leached out of the system (Jowitt et al., 2012).

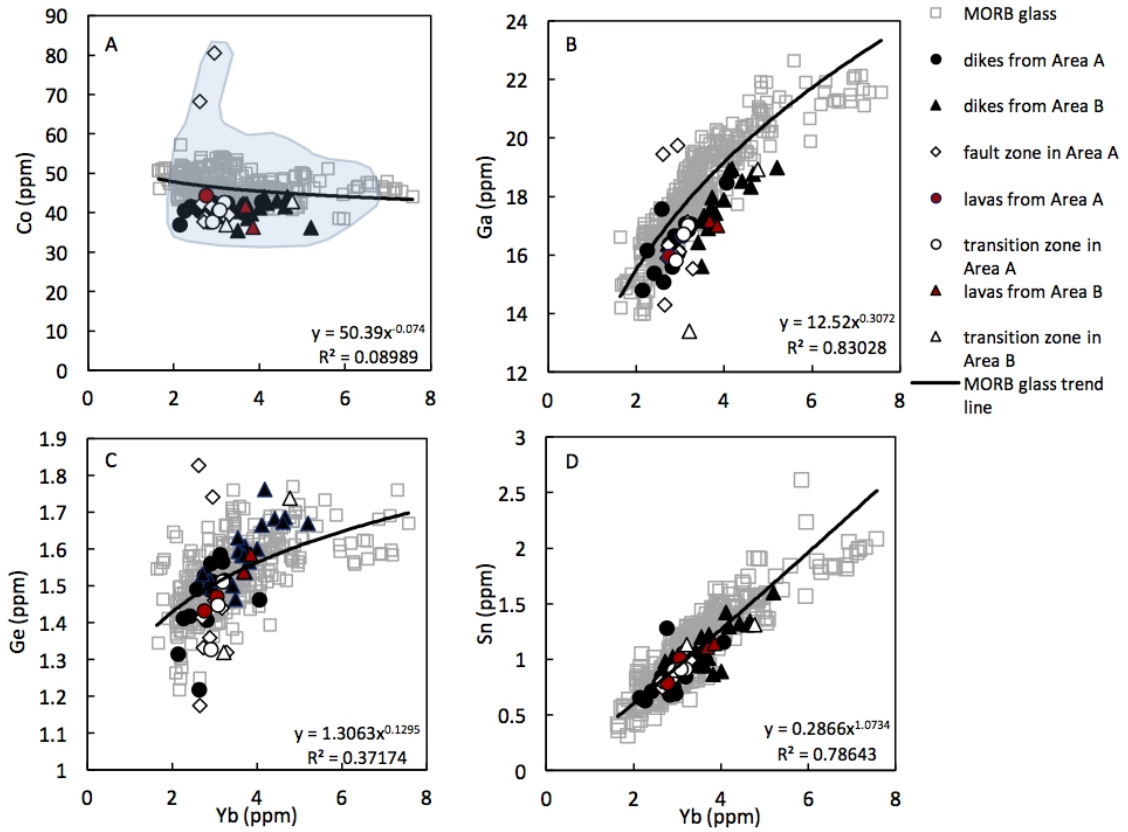

Figure 4.1. A-D: Cobalt, gallium, germanium, and tin concentrations (ppm) versus Yb (ppm) in Pito Deep samples (this study) compared with basalt glasses (Jenner and O'Neil, 2012; grey squares). Magmatic differentiation trends are defined by the element versus Yb trends in the glass that are fit to a power law curve (line and equation shown in each plot). Cobalt (A), germanium (C), gallium (B), and tin (D) show either no change or a slight depletion compared with MORB glass. Blue shaded area represents the previously published Pito Deep data from Heft et al. (2008), Barker et al. (2008), and Barker et al. (2010a).

The concentrations of Ga (Fig. 4.1 B) and Ge (Fig. 4.1 C) in the Pito Deep samples analyzed in this study are similar to MORB glass suggesting they were largely immobile during hydrothermal alteration. These two elements also show a strongly positive correlation with each other (Fig. 4.2). Previous observation of vent fluids from the Southern Juan de Fuca Ridge (SJFR) show a strong linear relationship between Zn and Ga (Metz and Trefry, 2000), which may indicate that these elements contents are controlled by the same parameters. However, the same correlation

between Ga and Zn is not observed in the upper crust of the Pito Deep, which might be a result of the small amount of Ga leached from the crust. The concentrations of Ga in 504B, Hess Deep, and 1256D also show no change compared to MORB glasses (Fig. 4.5 J, G and L; Alt and Emmermann, 1985; Stewart et al., 2002; Gao et al., 2009). Therefore, Ga and Ge are not useful tracers for sulphide mineralization at Pito Deep.

The concentration of Sn in the Pito Deep samples shows no change compared to MORB glass, which agrees with the absence of galena (the main mineral controlling Sn content in sulphide deposits; Fleischer, 1955) in the samples analyzed in this study. This indicates that Sn is immobile during hydrothermal circulation, thus Sn is not a useful tracer for sulphide mineralization at Pito Deep.

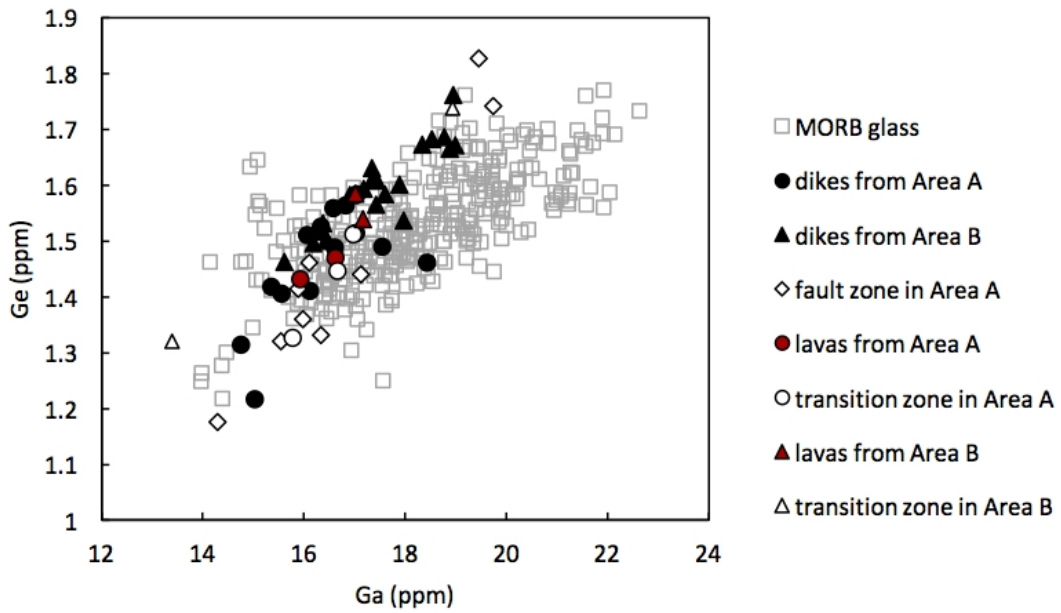

Figure 4.2. Bulk rock Ge concentration (ppm) versus Ga (ppm) in glass samples (Jenner and O'Neill, 2012; grey open squares) and the Pito Deep samples. These two elements behave similarly and do not partitioning into sulphide minerals during in hydrothermal processes.

4.2.2.2. Copper, zinc, arsenic, silver, cadmium, lead, and thallium

The concentrations of Cu, Zn, As, Ag, Cd, Pb and Tl in this study generally show no correlations with S content (Fig. 4.3; S content from Barker et al., 2010b), which indicates that the sulphur content is not a controlling factor for the distribution of these elements in Pito Deep. The reasons that the total sulphur content does not control the abundance of chalcophile element are: (a) protolith contains magmatic sulphur as well as hydrothermal sulphide minerals; and (b) various of hydrothermal sulphide minerals were formed in the Pito Deep, thus total sulphur content does not correlate with the concentration of a single chalcophile element.

The concentrations of Cu, Zn, As, Ag, Cd, Pb, and Tl in Pito Deep samples show both depletion and enrichment relative to MORB glass (Fig. 4.4). The samples which are enriched in these elements are mostly from the lava unit and the lava-dike transition zone (including the fault breccia samples). Most of the samples from the sheeted dike complex show depletion or no change in these elements, compared with MORB glass. The depletion in Zn, Cd and Pb are more common than the depletion in Cu, As and Ag in sheeted dikes (Fig. 4.4 A and B), which could be resulted from the larger composition uncertainties of Cu, As and Ag in fresh MORB glassed than Zn, Cd and Pb.

The concentrations of Cu, Zn, As, Ag, Cd, Pb, and Tl in the upper crust at Pito Deep do not show systematic changes with depth in the crust (Fig. 4.5). These elements are enriched in hydrothermal fluids (>300 °C) compared to seawater (Table 4.2), which indicates that these elements are mobilized from the sheeted dikes to the lava unit and the transition zone by hydrothermal fluids.

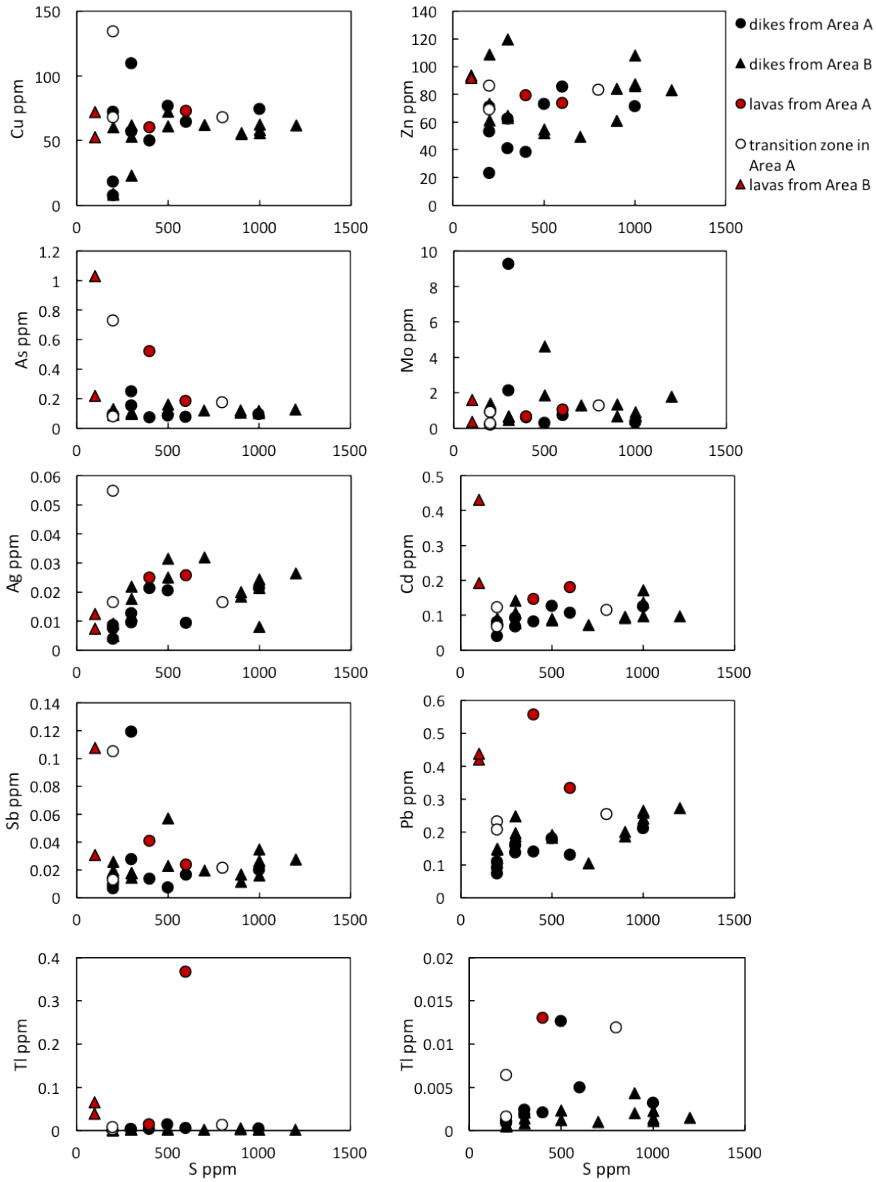

Figure 4.3. Correlations between the elements of interest and sulphur content in Pito Deep samples. None of the element concentration correlates with sulphur content. Sulphur content data is from Barker et al., 2010b.

Zinc is depleted in the Pito Deep dikes analyzed in this study (Fig. 4.4 A), as observed in previous studies (Fig. 4.5 A; Appendix F; Heft et al., 2008; Barker et al., 2008; Barker et al., 2010a). Two samples in the lava-dike transition zone (and two samples from fault zone, see discussion in Section 4.3) are enriched in Zn. These data

can be explained by a model in which the high-temperature fluids mobilized Zn from the sheeted dike complex, and the fluids were cooled by seawater in highly permeable crust, precipitating Zn-bearing sulphide minerals. However, Zn is not enriched in all transition zone samples (Fig. 4.6 A), instead, there appears to have been a scattered precipitation of Zn-bearing sulphides in the transition zone. Previous studies show consistency of Zn depletion throughout sheeted dikes in Pito Deep (Zoeller, 2014; Heft et al., 2008; Barker et al., 2010b). The depletion of Zn in dikes and enrichment in the transition zone is similar to the Zn distribution in the upper crust of Hole 504B (Fig. 4.5 B; Alt et al., 1989; Alt and Emmermann, 1985; Emmermann, 1983; Bach et al., 2003), Hess Deep (Fig. 4.5 C; Stewart et al., 2002), and 1256D (Fig. 4.5 D; Gao et al., 2009).

Table 4.2. Concentrations of the elements of interest in seawater and hydrothermal fluids.

	Seawater (ppt)[a]	Hydrothermal fluids (>300 °C) (ppb)
Co	2.36	1.3 - 13.4 [b]
Cu	192	620.8 – 2596 [b]
Zn	390	2600 – 6890 [b]
Ga	1.4	1.82 - 3.15 [c]
Ge	5.11	9.49 - 12.4 [c]
As	1725	2.25 - 33.9 [b]
Mo	9984	0 - 3.17 [c]
Ag	2.16	2.8 - 4.1[b]
Cd	67.2	24.2 - 78.4 [c]
Sn	0.476	
Sb	195.2	1 - 2.2 [b]
Tl	14.28	8.16 – 11.6 [c]
Pb	2.07	1.86 - 74.3 [b]

Note: Seawater concentrations were determined by analyzing 0.2 μm filtered seawater samples, which separated the dissolved and particulate forms of trace elements.
[a] Bruland, 1983; Donat and Bruland, 1995; [b] Von Damm et al., 1985; Von Damm, 1990 and 1995; Edmond et al., 1979b; Trefry et al., 1994; [c] Metz and Trefry, 2000

Copper is depleted in 40% of the dike samples in both Area A and B (Heft et al., 2008). Figure 4.6 B shows that Cu is depleted in the depth of 600 m to 0 mbld, while only two samples, both from the transition zone, show small enrichments. All of the lava samples analyzed previously and in this study show no change of Cu content (Fig. 4.5 E). Previous studies on Hole 504B (Fig. 4.5 F; Alt and Emmermann, 1985; Alt et al., 1989; Emmermann, 1983; Bach et al., 2003), Hess Deep (Fig. 4.5 G; Gillis et al., 2001), and 1256D (Fig. 4.5 H; Gao et al., 2009) all show depletion of Cu in dikes and enrichment in the transition zone.

Arsenic is enriched in two lavas and two transition zone samples from Pito Deep (Fig. 4.4 C; Fig. 4.6 C), but dikes show no general change compared to MORB glass (Fig. 4.4 C; Fig. 4.6 C). However, the dikes may be slightly depleted in As because of the high uncertainty of As in MORB glasses (shaded area in Fig. 4.6 C). One of the transition zone samples that is enriched in As also shows enrichment in Zn (Table 4.3). A lava sample enriched in As is also enriched in Cd and Tl (Table 4.3). The other As-enriched samples are not enriched in any other chalcophile elements (Table 4.3).

Silver is depleted in most of the dike samples from Area A, and generally shows no change in the dike sample from Area B. Only a single sample from the transition zone in Area A is enriched in Ag (Fig. 4.4 D; Fig. 4.6 D). The transition zone sample that is enriched in Ag also shows a slight enrichment in Cu, but depletion in Cd, and no change in Zn, As, Pb, or Tl (Table 4.3). The different degree of depletion in dikes from Area A and Area B is not a result of interference correction during data processing and appears to be a real feature of the samples.

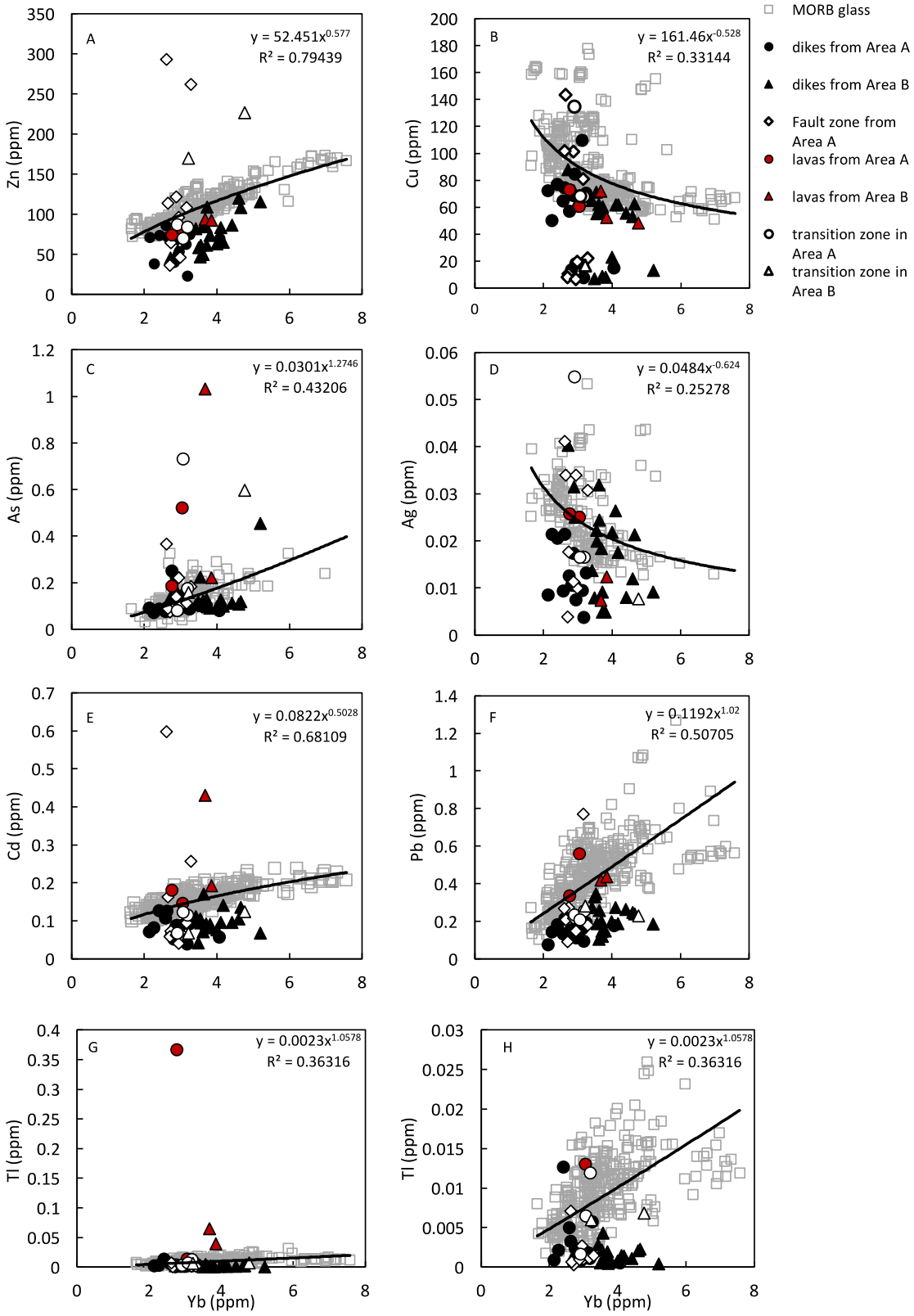

Figure 4.4. (Caption on following page)

Figure 4.4. A-G: Zinc, copper, arsenic, silver, cadmium, lead, and thallium concentrations (ppm) versus Yb (ppm) in Pito Deep samples (this study) compared with MORB glasses (Jenner and O'Neill, 2012; grey squares). Magmatic differentiation trends are defined by the element versus Yb trends in the glass that are fit to a power law curve (line and equation shown in each plot). The blue shaded areas are the data reported by previous studies (Heft et al., 2008; Barker et al., 2008; Barker et al., 2010a). H is a zoom-in of G.

Some samples from the fault zone and one lava sample are enriched in Cd, and most dike and transition zone samples are depleted in Cd (Fig. 4.4 E). The samples from the fault zone that are enriched in Cd are also enriched in Zn but show no change in As content and are depleted in Cu, Ag, Pb, and Tl (Table 4.3). The lava sample enriched in Cd show is also enriched in As and Tl but not in other chalcophile elements (Table 4.3).

Most of the dikes are depleted in Pb, and most lavas show no change in Pb (Fig. 4.4 F, Fig. 4.5 M, and Fig. 4.6 F). Only one sample from the fault zone is enriched in Pb. This is interpreted to be a result of high-temperature fluids mobilizing Pb from dikes and precipitating Pb-bearing minerals in the fault zone, where high-temperature fluids mixed with seawater and changed the solubility of Pb-bearing minerals. Previous studies on Hole 504B (Fig. 4.5 N; Alt et al., 1989; Bach et al., 2003), Hess Deep (Fig. 4.5 O; Stewart et al., 2002), and 1256D (Fig. 4.5 P; Cooper, 2007; Gao et al., 2009) all show depletion of Pb in dikes and enrichment in lava unit and the transition zone.

Table 4.3. Enrichment and depletion of the elements of interest in lavas, transition zone samples, fault zone samples (wall-rock dikes and fault breccias). Empty cells represent no change comparing the MORB glasses with uncertainties.

Sample ID	Area	Lithology unit	Depth to ldt (m)	Cu	Zn	As	Mo	Ag	Cd	Sb	Tl	Pb
020805-0108	A	lava	-280		-	+	+			+		+
020805-0042	A	lava	-205		-		+		+	+	+	
022205-1404	B	lava	-175		-		+		+	+	+	
022205-1335	B	lava	-130		-	+			+	+	+	
020805-0019	A	transition	-168	+	-			+	-			
020705-2343	A	transition	-47		-	+	+			+		-
020705-2317	A	transition	-12		-		+			+		-
4083-1829	B	transition	-123		+	+				+		
022105-0427	B	transition	0	-	+			-		+		
4078-1951	A	FZ wall-rock	-100						-		-	+
4078-1807	A	FZ wall-rock	79	-	-				-		-	-
021005-0741	A	FZ wall-rock	82	-	-				-		-	
021005-0708	A	FZ wall-rock	114	-	-			-	-		-	-
4078-1800	A	Fault breccia	79	-					-		-	-
4078-1728	A	Fault breccia	80		+			+	+	+		
021005-0730	A	Fault breccia	82		+				-	+	-	-
4078-1718	A	Fault breccia	83	-	+				+		-	-
4078-1720	A	Fault breccia	83	+	+		+		+	+	-	

+	enriched
-	depleted

Note:
ldt: lava-dike transition one; FZ: fault zone

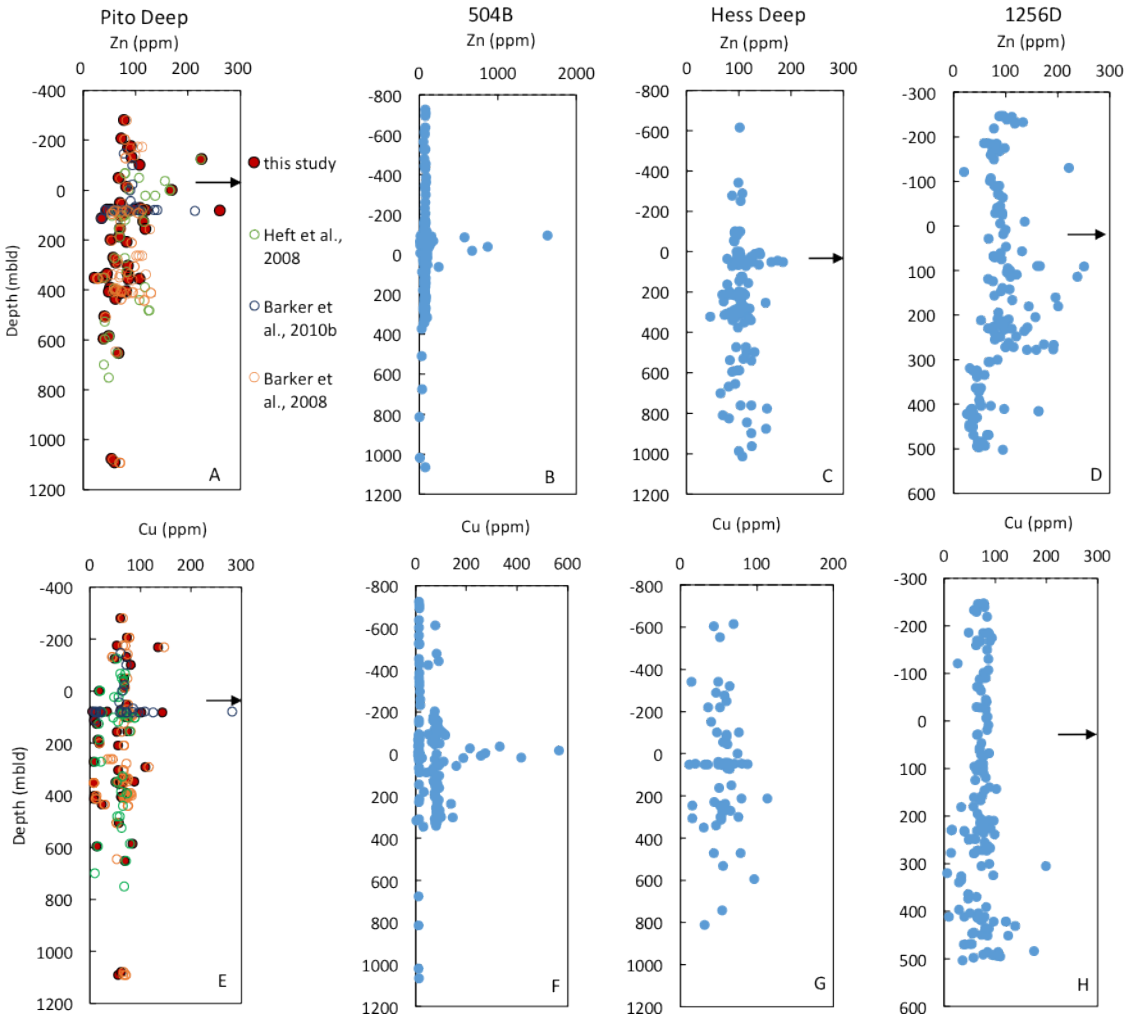

Figure 4.5. The concentrations of Zn, Cu, Ga, and Pb change with depth below lava-dike transition zone in Pito Deep (this study; Heft et al., 2008; Barker et al., 2008; and Barker et al., 2010a), 504B (Alt and Emmermann, 1985; Alt et al., 1989; and Bach et al., 2003), Hess Deep (Gillis et al., 2001; and Stewart et al., 2002), and 1256D (Cooper, 2007; Gao et al., 2009). Due to the lack of full element suite, the changing of the concentrations of Zn, Cu, Ga and Pb comparing with fresh MORB glasses is not calculated for 504B, Hess Deep, and 1256D. All data could be found in Appendix F. All four areas show Zn and Cu depletion in dikes and enrichment in the transition zone, and also show Pb depletion in dikes and enrichment in the lavas and the transition zone. There is little change of Ga concentration with depth in four areas.

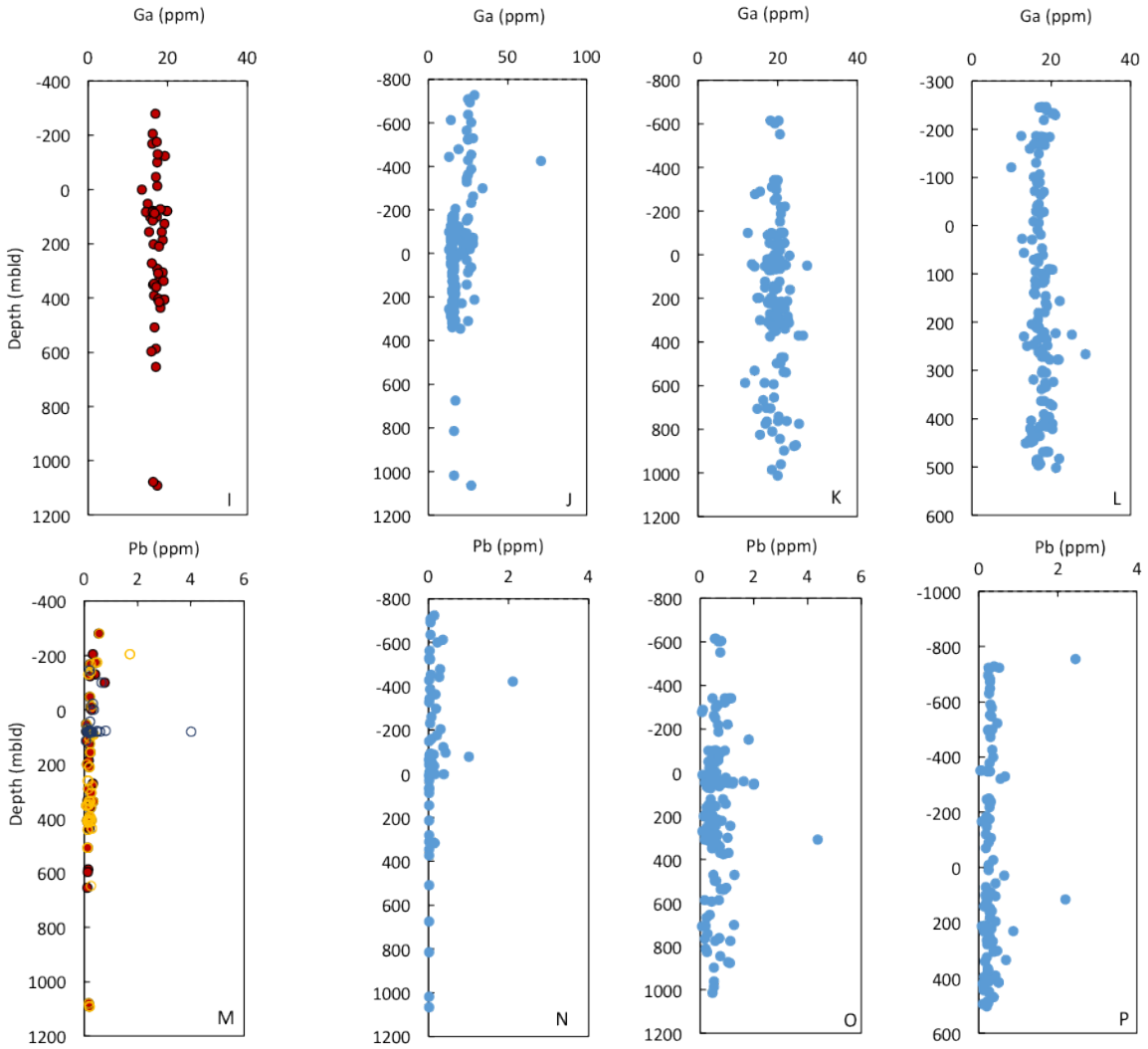

Figure 4.5. Continued.

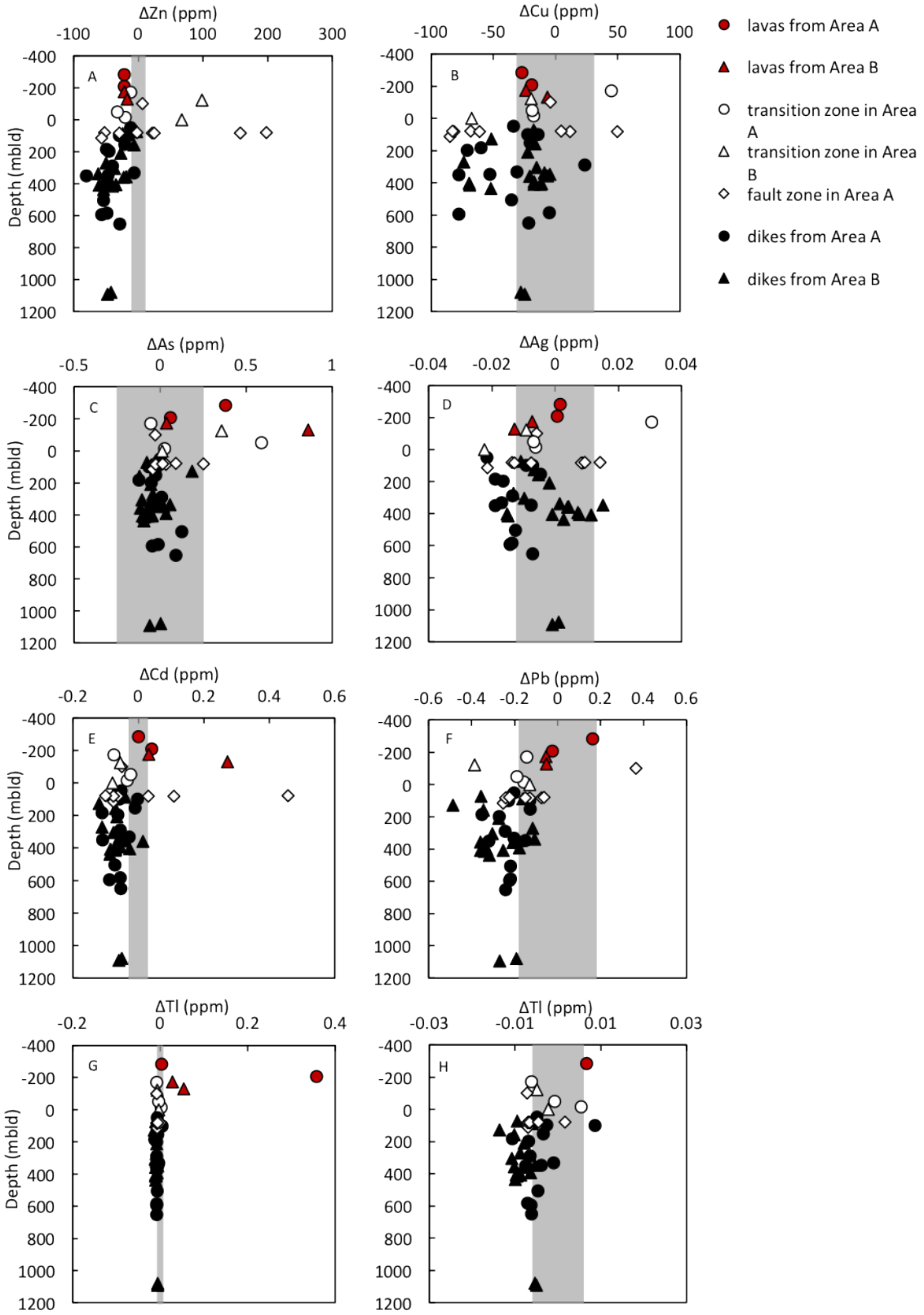

Figure 4.6. (Caption on following page)

Figure 4.6. A-G: Change of the concentrations of Zn, Cu, As, Ag, Cd, and Pb as a function of depth relative to the lava-dike transition zone. The grey shaded area in each plot is the uncertainty in the MORB glass composition (Jenner and O'Neill, 2012). The changes with depths show all enrichments occur in the transition zone and lava unit, whereas the concentrations of these elements in the sheeted dike complex shows no systematic change with depth.

Thallium is enriched in lava samples (Fig. 4.4 G and H; Fig. 4.6 G and H), while almost all dike samples are depleted in Tl. A similar variation of Tl concentration with depth into crust is observed in Hole 504B (Fig. 4.7; Nielsen et al., 2006). In this study, the enrichment of Tl in lavas is ~ 0.02 ppm (median value), and the depletion of Tl in dikes is ~0.007 ppm (median value). With the thickness ratio of lava and dike 1:2, the amount of Tl added into the lavas could not be mass balanced by the amount of Tl taken from dikes (0.014 ppm) by fluids, however, there are large uncertainties of the median values in lavas due to limited lava samples.

Previous studies proposed that Tl is added into the crust by low-temperature alteration off-axis based on the evidence that Tl has similar behaviour to the alkali metals Rb and Cs, which are added to the oceanic crust by low-temperature alteration off-axis (Heinrichs et al., 1980; Nielsen et al., 2006). However, Tl concentrations in the Pito Deep and Hole 504B do not have (or only have weak) correlations with Cs (Fig. 4.8 A and B). The lack of correlation between Tl and Cs is interpreted to indicate that Tl in the lavas is not gained during low-temperature alteration off-axis. Moreover, the lack of more enrichment in Tl at older crust in 504B than younger crust in Pito Deep also supports the argument that off-axis Tl addition may not be the sole control on the Tl distribution. There is a fair correlation between Tl and Cd in the Pito Deep samples (Fig. 4.9), which suggests that the Tl abundance may be partly controlled by the same parameters control Cd in the Pito Deep (exclude the fault zone and one lava

sample with high Tl concentration from Area A). Therefore, this study favors the hypothesis that Tl enrichment in the Pito Deep lavas is the result of on-axis hydrothermal circulation. This hypothesis needs to be tested by analyzing more lava samples in the future.

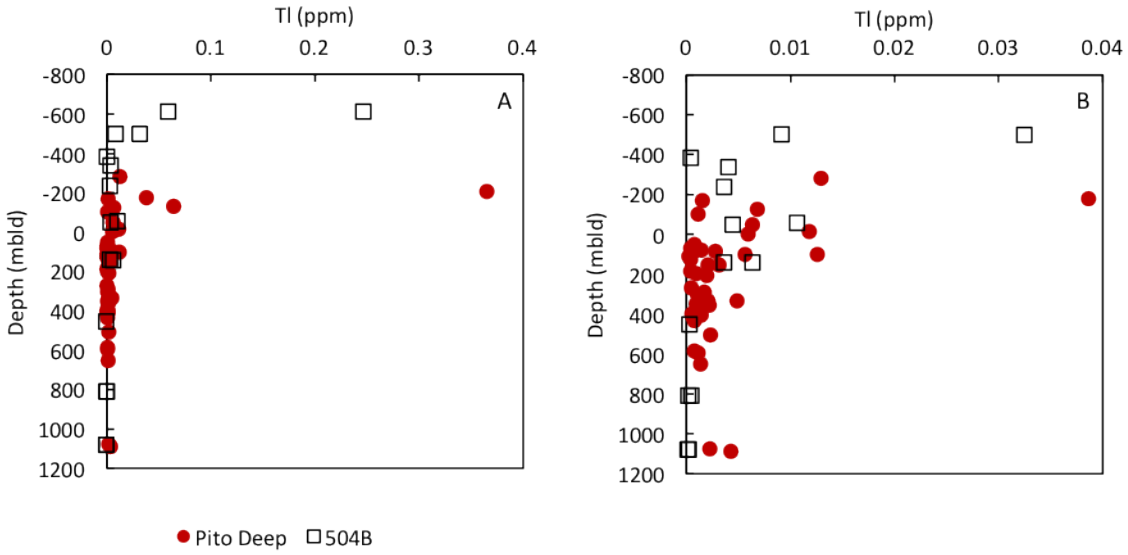

Figure 4.7. Concentration of Tl in the samples from the Pito Deep (red solid circles) and samples from Hole 504B (empty squares; Nielsen et al., 2006) as a function of depth relative to the lava-dike transition zone. Figure B is a zoom-in plot of figure A. Both locations show the same profile of depletion in dikes and enrichment of Tl in lavas.

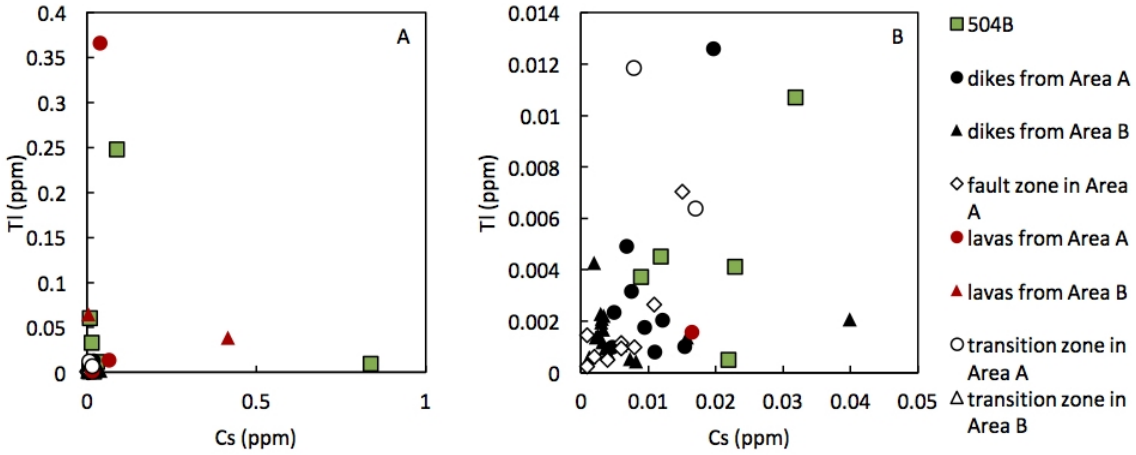

Figure 4.8. A and B: Thallium concentrations versus Cs concentrations of samples from Hole 504B (Nielsen et al., 2006), and the Pito Deep (this study). B is a zoom-in plot for A. Thallium show little correlations with Cs, indicating thallium uptake is not a result of low-temperature alteration.

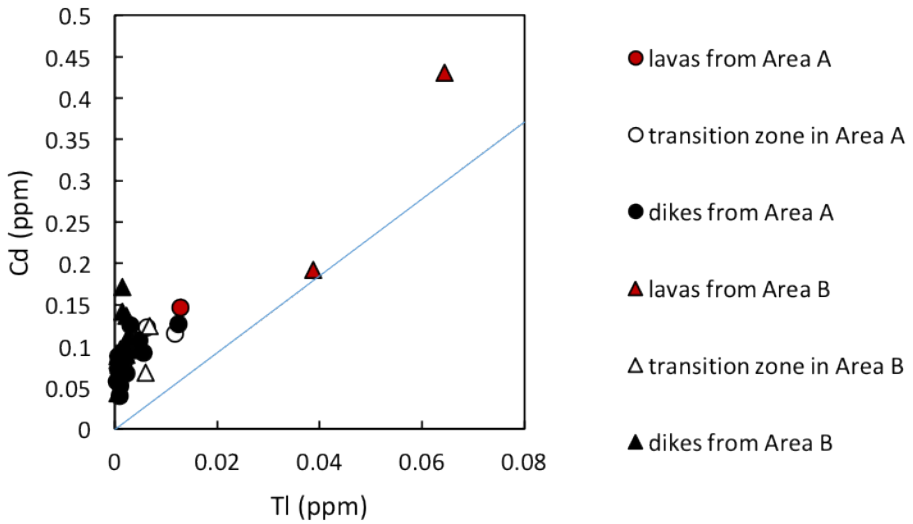

Figure 4.9. Cadmium concentration versus Tl concentration of samples (exclude one lava sample with high Tl concentration from Area A and samples from the fault zone) from the Pito Deep. Solid blue line represents the Cd/Tl ratio of seawater. Thallium and Cd have a fair correlation, which indicates the abundance of Tl is controlled by the same parameters control Cd abundance in the Pito Deep.

4.2.2.3. Molybdenum and antimony

The concentrations of Mo and Sb in this study generally show no correlation with S content (Fig. 4.3; S content from Barker et al., 2010b), which indicates that the sulphur content is not a controlling factor for the distribution of Mo or Sb in the Pito Deep.

Molybdenum is enriched in samples from all the geologic units of the Pito Deep (Fig. 4.10 A and C), and the dikes are more enriched in Mo than the lavas and transition zone samples. Molybdenum in the downwelling seawater will partition into chalcopyrite (Fouquet et al., 1988, 1993; Hannington et al., 1991; Tivey et al., 1995), and chalcopyrite is more stable in the sheeted dikes than in lava unit and transition zone. Molybdenum is added to the oceanic crust by hydrothermal circulation, as the concentration of Mo is ~11 ppb in seawater (Table 4.1; Bruland et

al., 2014), which is much higher than that in average EPR vent fluids (~0.8 ppb; Von Damm, 1995).

Similar to Mo, enrichment of Sb is observed in most of the Pito Deep samples (Fig. 4.10 B). Antimony is enriched in most of the dikes which also show Mo enrichment, and lavas and transition zone samples without Mo enrichment (Fig. 4.11, Fig. 4.12). The samples showing enrichment in Sb but not in Mo are also enriched in As (Fig. 4.12). The correlation between Sb and As in the lavas and transition zone samples may indicate that the abundance of Sb is controlled by the same parameters of As while precipitating associated with As within the lava unit and the transition zone. The possible metal-sulphide that controls both As and Sb abundances is pyrite, which needs to be tested in the future work.

The enrichment of Mo and Sb in dikes could be a result of seawater recharge on-axis, low-temperature alteration after the rifting of the Pito Deep, and/or addition of particulates carried by seawater. The change of Mo concentration in the dikes is 0.87 ppm on average, if the addition of Mo is caused by on-axis seawater recharge, calculated using a seawater Mo concentration of 11 ppb and assuming hydrothermal fluids contain no Mo (i.e. 100% added to the dikes), the seawater/rock ratio required for this amount of Mo addition is about 80. However, the water/rock ratio of the Pito Deep dikes averages 0.86±0.25 (Barker et al., 2008), which is much lower than the ratio calculated here. Therefore, it seems impossible that the addition of Mo introduced was only by recharged seawater on-axis. Unlike Mo, Sb is enriched in hydrothermal fluids compared to seawater (Table 4.2), thus the addition of Sb is also not a result of on-axis seawater recharge. The concentrations of Mo and Sb show no

correlation with Rb (Fig. 4.13), which indicates that the addition of Mo and Sb is probably not controlled by off-axis, low-temperature, alteration. The only plausible explanation left for the addition of Mo and Sb in the crust is that it resulted from addition of particulates in seawater. The concentration of Sb in seawater (Table 4.2) was analyzed after filtering by a 0.2 μm filter, however the particulates over 0.2 μm could enter the permeable upper oceanic crust. Previous study showed that oceanic sediments have a high Sb concentration (Jochum and Verma, 1996), which could cause the additional Sb in the crust.

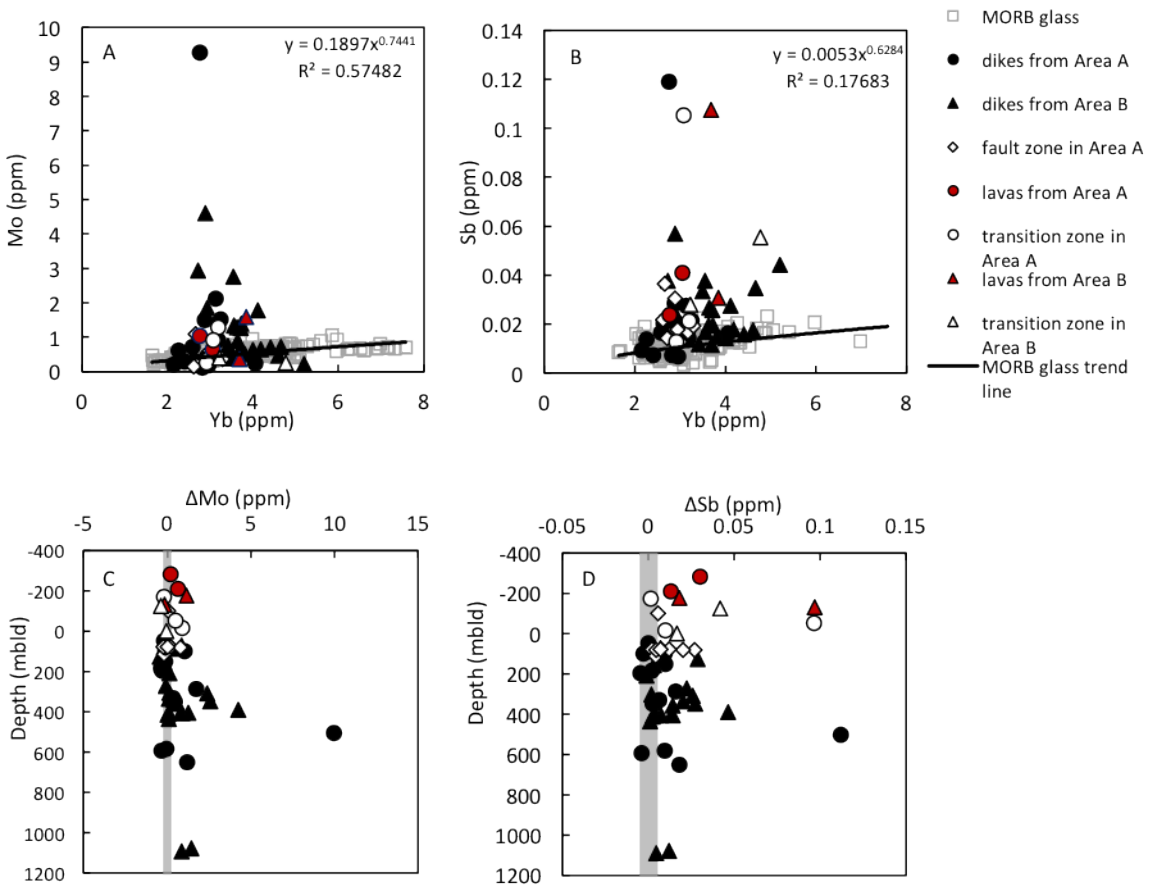

Figure 4.10. Molybdenum (A) and antimony (B) concentrations in Pito Deep compared with MORB glasses. The change of the concentrations of Mo and Sb as a function of depth beneath the lava-dike transition zone (C and D). The grey shaded area is the uncertainty in the MORB glass composition (Jenner and O'Neill, 2012).

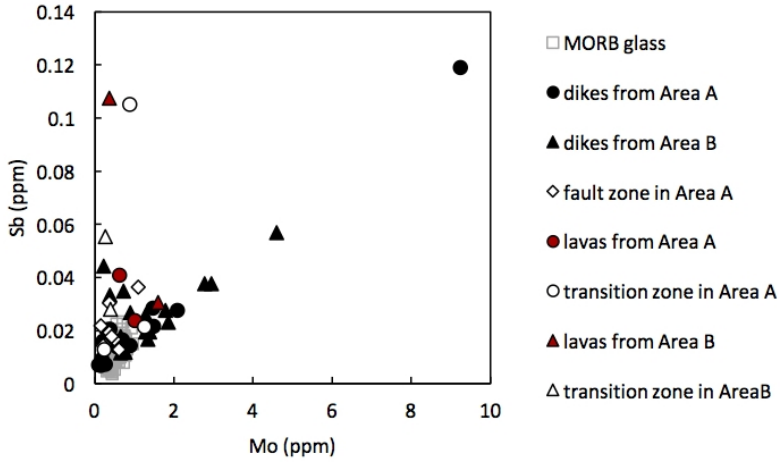

Figure 4.11. Plot of Mo and Sb in Pito Deep samples and MORB glass (Jenner and O'Neill, 2012). The dike samples show strong positive correlation between the concentration (ppm) of Mo and Sb, indicating the area of seawater alteration process.

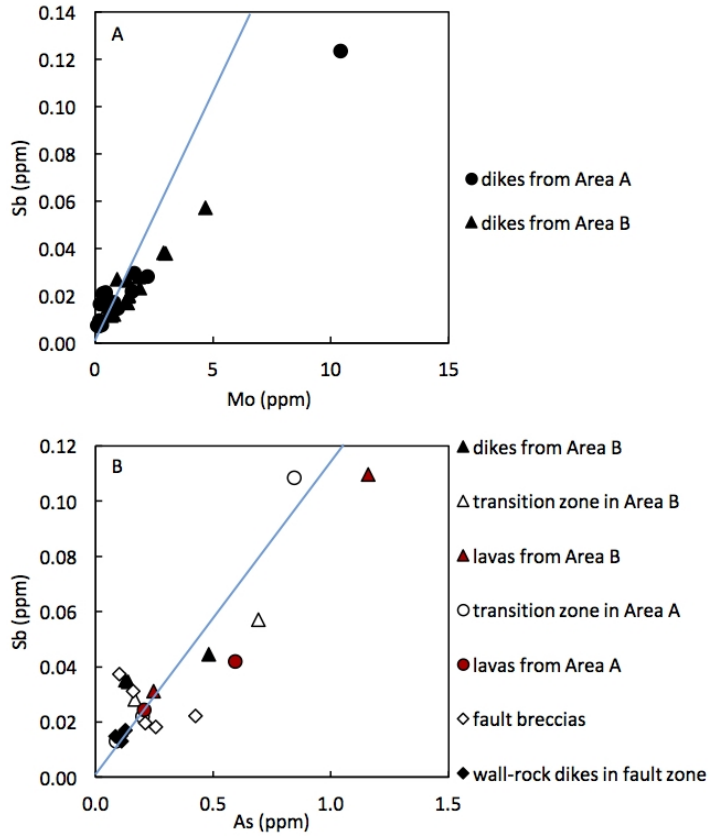

Figure 4.12. A: strong positive correlation between Sb and Mo concentrations in the Pito Deep dike samples. B: positive correlation between the concentrations of Sb and As in the Pito Deep lavas, transition zone samples, two samples of the dikes, and fault zone samples.

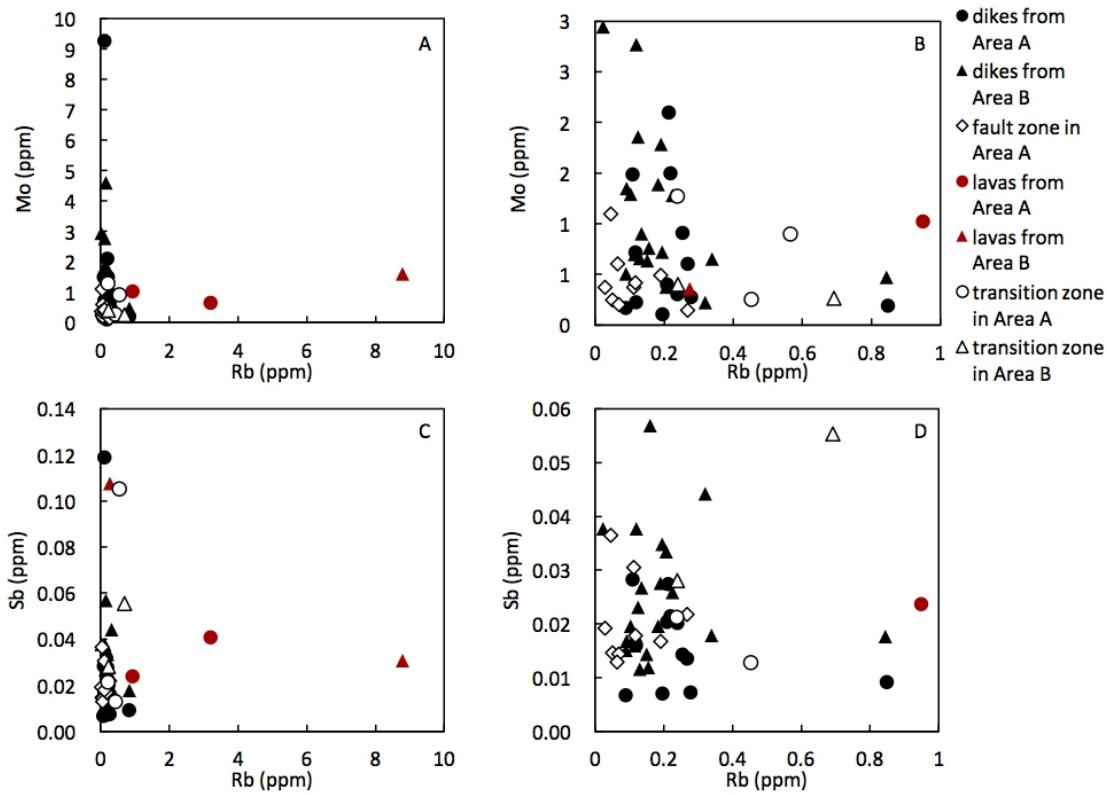

Figure 4.13. Concentrations of Mo (A) and Sb (C) versus Rb. Molybdenum and Sb show no linear correlations with Rb in the Pito Deep. Plot B is zoom-in for plot A, and D is zoom-in for plot C.

4.3. Sulphide Precipitation in a Fault Zone

A fault zone in Area A of the Pito Deep was sampled and studied previously (Section 3.1.1). This provided a highly permeable channel for both seawater and hydrothermal fluids. The $^{87}Sr/^{86}Sr$ value of fault breccias is high in the fault zone (Fig. 4.14 A) indicating an input from a higher $^{87}Sr/^{86}Sr$ source of cool seawater (Barker et al., 2010a).

The concentrations of Zn, As, Cu, Ag, Cd, and Tl (Fig. 4.14 B-F, H) show depletion and/or no change compared to MORB glasses in wall-rock dikes of the fault zone, which is similar to the depletion of these elements in dikes out of fault zone (Section 4.2.2). The fault breccias generally show different extents of enrichment in Zn, As, Cu,

Ag, and Cd (Fig. 4.14 B-F). Fault breccias show relatively higher concentrations of Tl than in wall-rock dikes (Fig. 4.14 H). The fault breccias enriched in Zn, Cd and Ag (Fig. 4.14 B, E and F) have higher $^{87}Sr/^{86}Sr$ ratios than background dikes (Fig. 4.14 A).

Before the fault zone formed (or before focused flow started), it is assumed that the area underwent the same hydrothermal circulation as the areas outside the fault zone. Therefore, the elements of interest were leached from crust before the faulting, which explains the similar depletion of Zn, As, Cu, Ag, Cd, and Tl in the wall-rock dikes to the dikes outside the fault zone. However, after faulting, the fault zone acted as a permeable channel for downwelling seawater to mix with upwelling hydrothermal fluids, as indicated by the relatively high $^{87}Sr/^{86}Sr$ values in fault breccias. Thus, the fault zone could be considered as transition zone. The study of the same fault zone by Barker et al. (2010a) concluded that the fluid temperature in the fault zone is 392±33 °C on average. However, the observation of chalcophile elements enrichment in fault breccias suggests that the temperature of the fluids passing through the fault zone had not always stayed that high. Mixing between hydrothermal fluids and seawater decreased fluid temperature, and increased the pH of the fluids, which decreases the solubility of sulphide minerals containing Zn, As, Cu, Cd, and Ag (Section 1.4.1; Fig. 1.5). Moreover, similar to the the lavas and transition zone samples outside the fault zone, the enrichment of Zn, As, Cu, Cd, and Ag in fault breccias is also heterogeneous. Therefore, the enrichment of Zn, As, Cu, Cd, and Ag in fault breccias is very likely the result of sulphide precipitation during fluid mixing in the fault zone. A plausible interpretation of the heterogeneous enrichment of the elements in fault breccias is that, the fault breccias provide multiple permeable fractures as fluids pathways, thus

the fluids would follow the higher permeability pathways rather than all of them. Therefore, only the fault breccia samples that came from fluid pathways are the ones enriched in the elements precipitated as sulphides.

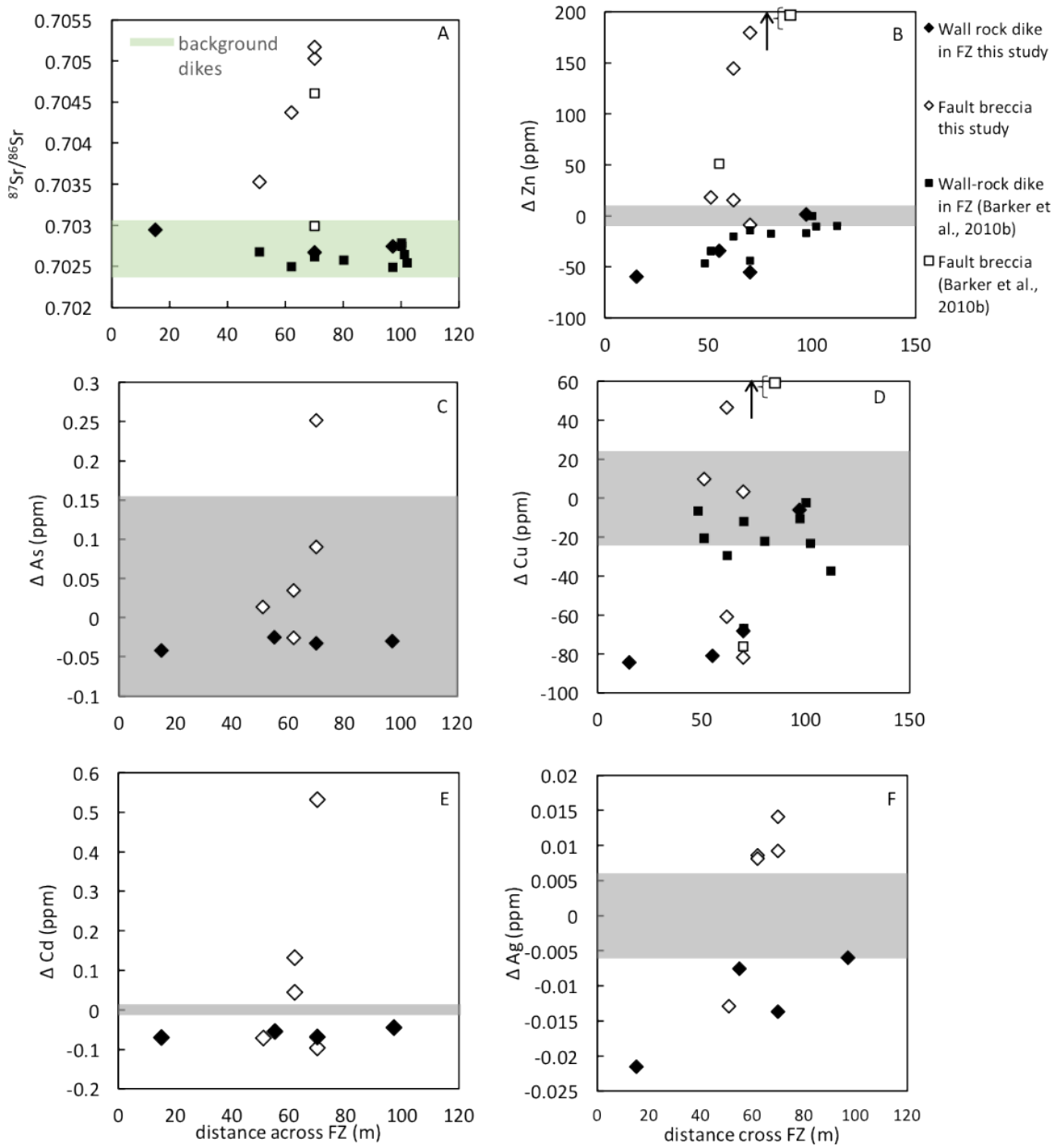

Figure 4.14. (Caption on following page)

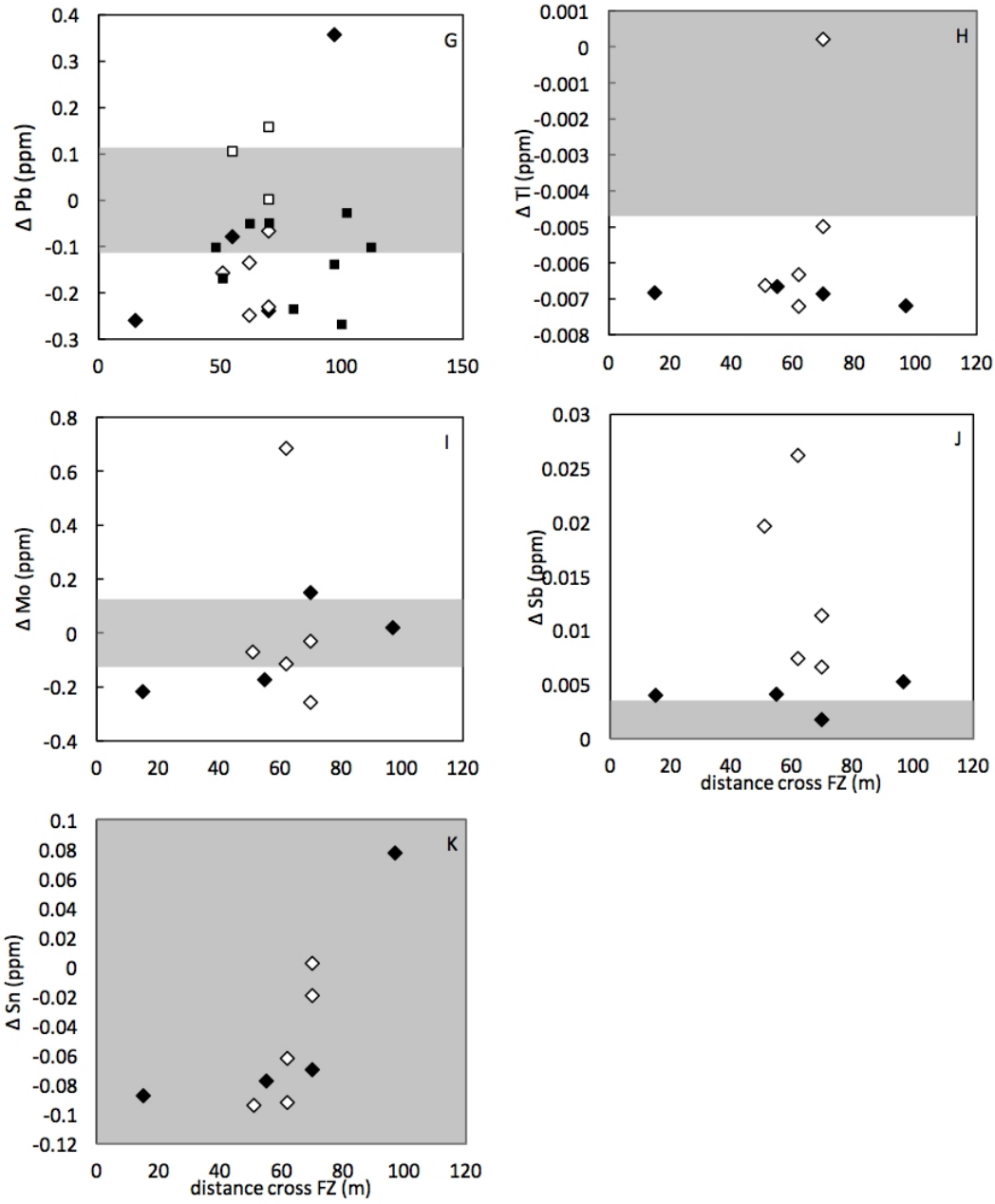

Figure 4.14. Composition changes versus lateral distance cross fault zone in Area A. The distances cross fault zone are represented by the lateral coordinates of samples. Grey shaded areas are the uncertainties in the MORB glasses composition. Green shaded area represents for the $^{87}Sr/^{86}Sr$ values of the background dikes from Pito Deep. "FZ" represents fault zone. Arrows in B and D represent a fault breccia sample with higher values of enrichment in Cu and Zn than the scale. A: $^{87}Sr/^{86}Sr$ in fault breccia samples are higher than in the wall-rock dike samples; B-K: changes of Zn, As, Cu, Cd, Ag, Pb, Tl, Mo, Sb and Sn concentration compared with MORB glass across the fault zone. $^{87}Sr/^{86}Sr$ values of Pito Deep background dikes are from Barker et al.

(2008), and the $^{87}Sr/^{86}Sr$ values of fault breccias from Pito Deep are from Barker et al. (2010a).

Lead is mostly depleted or unchanged in the fault zone samples, and only one wall-rock dike is enriched in Pb (Fig. 4.14 G). The sample enriched in Pb is from 100 m above the lava-dike boundary, which may be due to precipitation before the faulting event. After faulting, Pb did not precipitate during fluid mixing, which indicates that the fluids may be under-saturated in Pb-bearing minerals.

Thallium is mostly depleted in fault zone samples, and one fault breccia is relatively enriched in Tl compared to the other fault zone samples (Fig. 4.14 H). The depletion of Tl was probably caused by hydrothermal processes before faulting. The fault breccia that contains a relatively higher concentration of Tl may result from Tl-bearing sulphide precipitation during fluid mixing within the fault zone after the faulting, in the same way as the lavas showing enrichment outside of the fault zone (Section 4.2.2.2). The lack of observation of Tl enrichment in fault zone samples indicates that the fluids were under-saturated in Tl-bearing minerals.

Molybdenum is depleted or unchanged in most of the fault zone samples, and only one fault breccia is enriched in Mo (Fig. 4.14 I). The fault breccia enriched in Mo is also enriched in Cu. According to the studies of vent fluids by Trefry et al. (1994) and Metz and Trefry (2000), Mo is most likely removed from vent fluids during precipitation of Cu-rich sulphide at temperatures >350 °C. Thus, the fault breccia enriched in both Mo and Cu is interpreted to be the result of Cu-rich sulphide precipitation during fluid mixing within the fault zone. As discussed in Section 4.2.2.3, Mo is generally added into the crust by recharged seawater. There is no Mo

enrichment in most of the fault zone samples might be because of the lack of Cu-riched sulphides in those fault zone samples.

Antimony is generally unchanged in wall-rock dikes in fault zone, and enriched in fault breccias (Fig. 4.14 J). As discussed in Section 4.2.2.3, the enrichment of Sb in fault breccias is interpreted related to the particulate input by the recharged seawater and on-axis co-precipitation with As.

4.4. Summary

In the Pito Deep upper crust the concentrations of Co, Ga, Ge, and Sn are relatively unchanged compared to MORB glasses. Zinc, Cu, As, Ag, Cd, Pb, and Tl are depleted in most of the dikes due to hydrothermal alteration, and unchanged or enriched in lavas and/or transition zone samples. Molybdenum and Sb were generally added to the crust. The enrichment of Zn, Cu, Ag, Cd, and Pb in lavas and/or transition zone samples is a result of sulphide precipitation during fluid cooling (either by conductive cooling or fluid mixing). The enrichment of As and Sb in the transition zone and lava unit is interpreted as indicating on-axis sulphide-mineral precipitation. Whereas, the enrichment of Mo and Sb (in the dikes) is interpreted to have resulted from both recharged seawater input and the particulates input.

The fault zone in Area A of the Pito Deep underwent similar alteration as dikes outside the fault zone before the faulting. Zinc, Cu, As, Ag, Cd, and Tl were all depleted in the wall-rock dikes from the fault zone before faulting. After the fault formed, fluid mixing caused sulphide precipitation adding Zn, Cu, As, Cd, and Ag to the fault zone breccias. However, the precipitation of metal-sulphides did not just occur in a

focused, localized zone. It is more likely that the samples enriched in these elements were on the pathways of fluid mixing, whereas other samples are not. Molybdenum is generally not changed in fault zone samples because of the fluids passing through the fault zone is under-saturated in Mo-bearing sulphides. Antimony is generally added into the fault zone samples by both on-axis Sb-bearing sulphides precipitation and input from particulates carried by recharging seawater.

CHAPTER 5

5. CONCLUSIONS AND FUTURE WORK

Base on the discussion in Section 4.3, this chapter is considering the fault breccias as transition zone samples for observing chalcophile elements distribution and calculating diffuse fluids composition. The chalcophile elements Cu, Zn, As, Ag, Cd, Tl and Pb in the Pito Deep area are generally depleted in the sheeted dikes, and enriched in the transition zone and lava unit (Section 4.2). This is also the conclusion of previous studies on fast- to superfast-spreading mid-ocean ridges, although largely just Cu and Zn have previously been studied (e.g., Alt et al., 1989 and 2010; Gillis et al., 2001; Nielsen et al., 2006). The distribution of chalcophile elements indicates that hydrothermal fluids mobilized these elements from dikes and carried them to the transition zone and lavas, where the temperature and/or pH of the fluids changed and precipitation of metal-sulphides occurred. The abundance of the elements of interest indicates that the precipitation areas of these elements are scattered in the Pito Deep hydrothermal system. The results of this study also include the elements distribution in a fault zone at the Pito Deep, which provided channels for fluid mixing and the precipitation of metal-sulphides.

This chapter first interprets the distribution profiles of chalcophile elements in the upper oceanic crust at the Pito Deep (Section 5.1). Based on the distribution of the elements of interest, Section 5.2.1 discusses plausible models for generating diffuse fluids in Pito Deep. Mass balance calculations for the elements of interest between high-temperature hydrothermal fluids and diffuse fluids from the Pito Deep are described in Section 5.2.2. The results of this study addressing the question of diffuse

fluid generation are summarized in Section 5.3. This study also raises several questions about analytical methods for the chalcophile elements and the possibilities of additional sources of chalcophile elements in natural systems, which need to be tested in the future studies (Section 5.4).

5.1. Distribution Profiles of the Elements of Interest in the Upper Crust of the Pito Deep

As discussed in Chapter 4, the chalcophile elements Zn, Cu, As, Ag, Cd, Pb, and Tl are mobilized from the sheeted dike complex during high-temperature hydrothermal circulation. In contrast, Mo and Sb are added to the crust during hydrothermal circulation. Cadmium, Pb, As, and Tl are enriched in both lavas and transition zone samples, while Cu, Zn, and Ag are only enriched in transition zone samples. Copper, Zn, and Ag are only enriched in the transition zone but not in lavas, which indicates that these elements were precipitated in the transition zone and the fluids became under-saturated in these elements when they reached the lava unit. Whereas Cd, Pb, As, and Tl are enriched in both the lava unit and the transition zone, which indicates that their solubilities decrease more slowly when temperature drops.

Hydrothermal fluids mobilized the elements from dikes and carried them upwards to the transition zone (considering fault zone breccias as transition zone samples) and/or the lava unit where the elements precipitated. Therefore, the amount of the loss from dikes should be larger than, or at least equal to, the amount of enrichment in the transition zone and/or the lava unit. To calculate the loss from dikes and gain in the transition zone and/or the lava unit, the median values of

depletion and enrichment are used. The median value is defined by the middle value in the data population arranged from smallest to the largest. The samples selected and analyzed only include four lava samples and five transition zone samples. The influence from the extremely large or small values could be statistically minimized by using median value rather than mean value. However, the uncertainties of using median value still could not be overlooked. For example, one lava sample is more than ten times enriched in Tl than the other three lava samples, in which case, with the limited numbers of lava samples, the extreme enriched in Tl in one sample could generate large uncertainties for the mass balance calculation of Tl.

Cadmium and Pb are depleted in dikes and enriched in both lavas and samples from the transition zone (Fig. 5.1 A). The median value of Cd and Pb enrichment in lavas and the transition zone is about twice as the depletion in the dikes (Table 5.1). Since the thickness ratio of sheeted dike complex / (lava unit and the transition zone) is about 2, nearly all the Cd and Pb leached from the dikes may have been precipitated within the lavas while interacting with diffuse fluids. However, this calculation considers the fault zone samples as transition zone samples, which could possibly enlarge the total enrichment amount in the lava unit and the transition zone. Therefore, it is possible that there are still considerably higher concentrations of Cd and Pb left in the high-temperature hydrothermal fluids than nearly zero assumed above.

Table 5.1. Median values* of the elements of interest changes in the upper crust of Pito Deep.

	thickness normalized to sheeted dike complex	Median values of changes (ppm)						
		ΔCu	ΔZn	ΔAs	ΔAg	ΔCd	ΔTl	ΔPb
Sheeted dike complex	1	-52	-45	-0.098	-0.012	-0.06	-0.007	-0.27
Lava section and transition zone	0.5	-	-	0.46	-	0.095	0.03	0.4
Transition zone (including fault zone samples)	0.2	184	114.5	-	0.021	-	-	-
		ΔMo	ΔSb					
Enrichment in all sections		0.4	0.014					

Note:
*Median values are used instead of mean values because that the median value is resilient to extremely large or small values,
Dash lines (-) mean that the changes of concentrations are within the MORB glass uncertainties.
The thickness of the sheeted dike complexes, lava section and the transition zone are 600-1000 m, 300-500 m, and 80-200 m respectively (Chapter 3; Heft et al., 2008; Hayman and Karson, 2009).

Arsenic and Tl are depleted in dikes and enriched in both lavas and transition zone samples (Fig. 5.1 B). The median values of As and Tl enrichment in the lava unit and the transition zone are more than twice the depletion in the dikes (Table 5.1). Assuming that the mass ratio of dike/(lava and transition zone) is 2, if the additional As and Tl are supplied by seawater (1.7 ppb and 0.014 ppb respectively), the seawater/rock ratio would have to be 150 and 1140 respectively. Such large seawater/rock ratios do not appear to be realistic for the lava unit and the transition zone (e.g., fluid/rock ratio is ~50 in the transition zone of Hole 504B, Alt et al., 1986), thus an additional source of As and Tl other than seawater is possibly needed to achieve the large amount of enrichment in the lavas and transition zone samples. It is possible that this source is particulates carried by bottom seawater. However, the uncertainties of As concentration in MORB glasses and the uncertainties of the

median value of Tl enrichment in lavas are large, thus it is also possible that As enrichment in lavas and the transition zone and Tl enrichment in lavas could be balanced by the depletion in dikes.

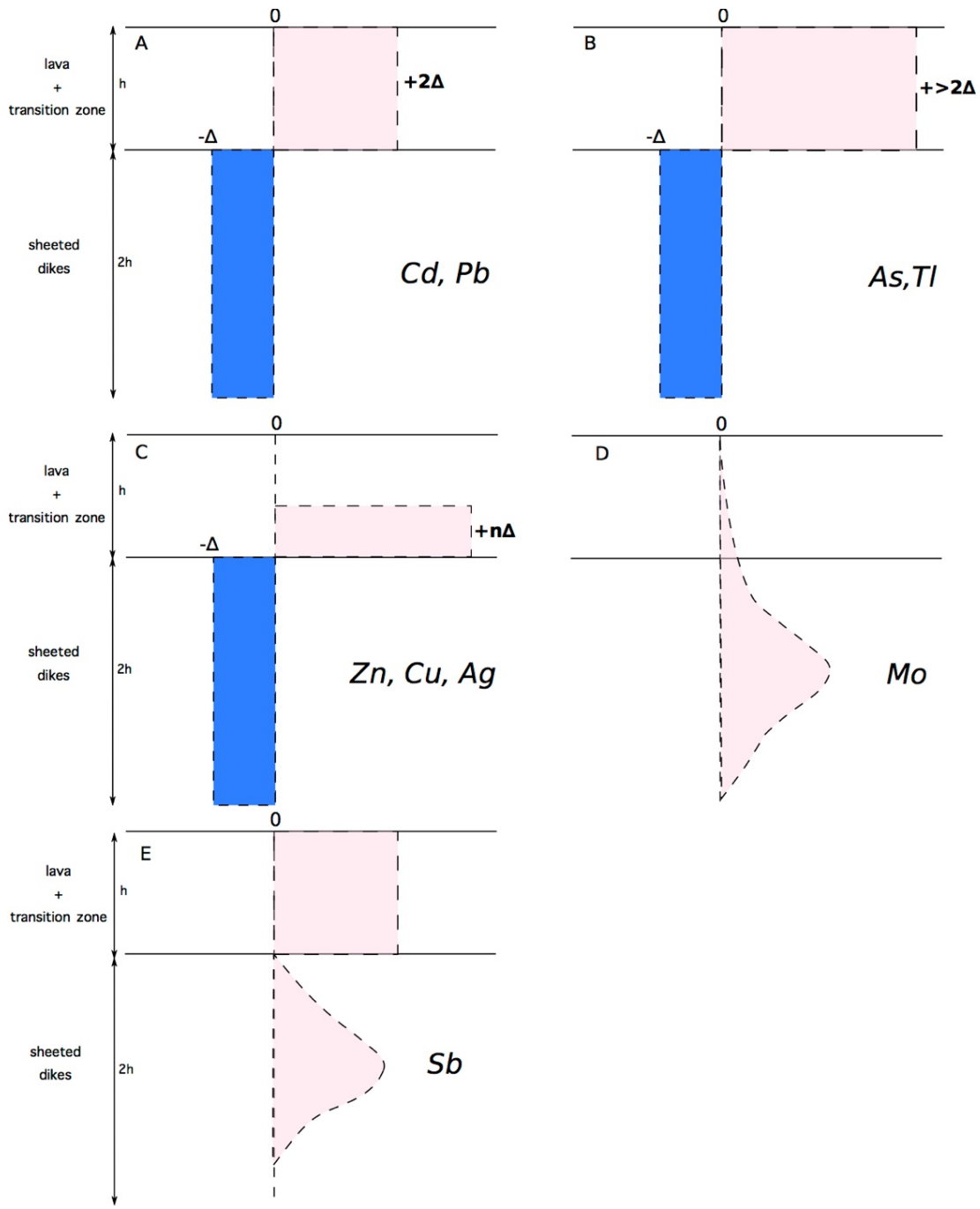

Figure 5.1. (Caption on the following page)

Figure 5.1. Cartoon profiles of the changes of the elements of interest against depths comparing to MORB glasses in Pito Deep. The thickness of sheeted dike complex (2h) is twice as the lava unit and the transition zone (h). Zero value in all profiles means no change. Pink- and blue-shaded areas represent enrichment and depletion of the element compared to MORB glass respectively. A: enrichment in the lavas (+ 2Δ) is about twice of the depletion in dikes (− Δ), representing no net loss from the crust. B: enrichment over two times (+> 2Δ) in lavas and transition zone of the depletion in dikes (− Δ). C: enrichment in the transition zone. D: enrichment in almost all the samples in the upper crust, and the enrichment of the element reaches a peak at a certain depth in the dikes. E: enrichment in almost all the samples in the upper crust. Enrichment in dikes at a certain depth, and equally enriched in lavas and the transition zone.

Zinc, Cu and Ag are depleted in dikes and enriched only in the transition zone (Fig. 5.1 C). The median values of Zn and Cu enrichment in the transition zone are more than twice the depletion in dikes, whereas the median value of Ag enrichment in the transition zone is similar to that of the depletion in dikes. This indicates that the enrichment of Zn, Cu, and Ag in the transition zone can be mass balanced by the amount of these elements mobilized from the dikes. Calculating by mass ratio of dikes/transition zone and the changes of concentrations (Table 5.1), out of the mobilized amount, 71% of Cu, 51% of Zn, and 35% of Ag was precipitated back in the crust in the transition zone. In other words, the rest of the mobilized amount of Cu, Zn and Ag were carried by the hydrothermal fluids to the seafloor.

Molybdenum and Sb are enriched in all units of the upper crust. Enrichment of Mo reaches a maximum within the dikes, whereas Sb is equally enriched in dikes, lavas and transition zone samples. According to the discussion in Chapter 4, the lack of correlation of Mo and Sb with Rb suggests that Mo and Sb were added to the crust on-axis. Assuming that the concentrations of Mo and Sb in seawater are 10 ppb and 0.2 ppb (Table 4.2), such enrichments of Mo and Sb requires seawater/rock ratio of

40:1 and 70:1, respectively. Alternatively, Jochum and Verma (1996) suggested that the bottom seawater could be modified by earlier interaction with nearby sediments, which makes the seawater extremely enriched in Sb. The study by Jochum and Verma (1996) did not include Mo, however, this process is also plausible for explaining the addition Mo in the crust. There might be some particulates contribution from pelagic ooze at the Pito Deep.

5.2. Diffuse Fluid Generation in the Upper Crust of Pito Deep

5.2.1. A plausible model of diffuse fluid generation in the Pito Deep crust

Compared with seawater, high-temperature hydrothermal fluids are enriched in Cu, Zn, As, Ag, Cd, Sb, Tl, and Pb (Table 4.1). The results of this study show that these elements (except for Sb) were mobilized by hydrothermal fluids from the sheeted dikes. These elements are enriched in the transition zone and lava unit, which suggests that the fluids temperature and/or pH changed when they reached this level causing metal-sulphide precipitation. There are some other minerals hosted some of these chalcophile elements, which could contribute to the enrichment of the chalcophile elements. For example, Zn could be hosted in secondary silicates (Zoeller, 2014). This thesis will use metal-sulphide precipitation as the dominant reason for chalcophile elements enrichment. Previous studies proposed three models for the generation of diffuse fluids, (A) mixing of seawater and high-temperature hydrothermal fluids, (B) conductive cooling of high-temperature hydrothermal fluids, and (C) conductive heating of seawater. Among the three models, this study tests the

first two models (Fig. 5.2) using the chalcophile element distribution in the upper crust at Pito Deep. The conductive heating of seawater model could not be tested by the results of this study, because the model does not directly involve chalcophile elements precipitation. However, generating large amounts of diffuse fluids via model (C) mechanism would require conductive cooling of large amounts of high-temperature hydrothermal fluid, and this would lead to model B (Fig. 5.2 B). The results of this study show that both fluid mixing and conductive cooling of hydrothermal fluids may have led to the generation of diffuse fluids during the formation of the Pito Deep crust (Fig. 5.2).

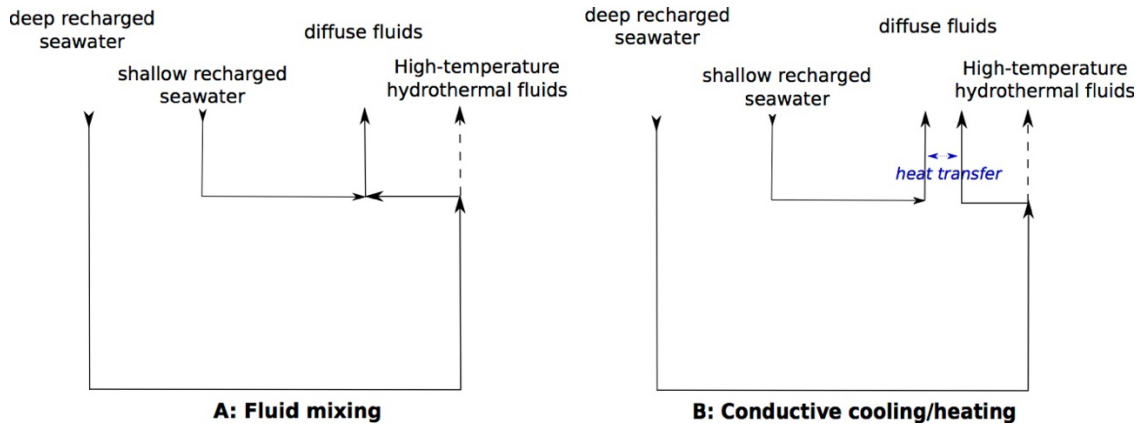

Figure 5.2. Schematic diagram of models for the generation of diffuse fluid. The deep-recharged seawater is heated up during hydrothermal circulation forming high-temperature hydrothermal fluids. A: fluid mixing model for diffuse fluids generation. The dashed line represents the un-mixed part of the high-temperature hydrothermal fluids. If the high-temperature hydrothermal fluids were thoroughly mixed into diffuse fluids, the model would only follow the solid lines. B: conductive cooling of high-temperature hydrothermal fluids for diffuse fluids generation. The dashed line represents the part of high-temperature hydrothermal fluids that are not cooled into diffuse fluids. If all high-temperature hydrothermal fluids were all conductively cooled to form diffuse fluids, the model would only follow the solid lines.

The results of this study, together with the data for Cu and Zn from previous studies of the upper crust at Pito Deep (Fig. 4.5; Heft et al., 2008; Barker et al., 2010a and 2010b), show that Zn and Cu are both enriched only in the transition zone. As introduced in Chapter 1, if diffuse fluids are generated by conductive cooling of high-temperature hydrothermal fluids, the pH of the fluids would decrease (due to metal-sulphide precipitation; Equation 1.1) which inhibits Zn precipitation (Fig. 1.4 A). The results show that Zn enrichment occurred in the transition zone of Pito Deep, which indicates that diffuse fluids were generated in the transition zone by (1) fluid mixing, and/or (2) conductive cooling of high-temperature hydrothermal fluids to low enough temperatures to drive Zn-sulphide precipitation (<250 °C; Fig. 1.4 B; Janecky and Seyfried, 1984) despite the decreasing pH caused by metal-sulphide precipitation. As introduced in Section 1.4.1, the main precipitation temperature range for Zn-sulphides is from ~170 °C to <250 °C (Fig. 1.4 A and B). If the fluid temperature decreased to lower than ~170 °C, nearly all Zn would have been precipitated out and the fluids became under-saturated in Zn-sulphides. The precipitation of Zn-sulphides only was observed in the transition zone, which indicates that the fluid temperature at the boundary between the transition zone and the lava unit was lower than ~170 °C, or the fluids had lost most of Zn before the fluids reached the boundary.

The observation that Ag was only precipitated in the transition zone but not in the lava unit indicates that Ag-bearing minerals became under-saturated or no Ag left in fluids when fluids reached the lava unit. The similar distribution of Ag, Cu, and Zn may suggest that Ag could partition into both Cu-rich and Zn-rich sulphide minerals

in the transition zone. However, the precipitation temperature range for Ag-bearing minerals is poorly constrained due to the limitation of previous field and experimental data.

Arsenic, Cd, and Pb precipitated in both the transition zone and the lava unit (Fig. 4.6), which indicates that the temperature of the fluids was below the precipitation temperature of the sulphide minerals containing these elements. Although the precipitation temperature of As, Cd, and Pb is poorly studied, these elements are commonly recognized as a low-temperature sulphide mineral assemblage (Section 1.4.2). This indicates that the fluid temperature decreased into the temperature range for these elements to precipitate in both the transition zone and lava unit.

Thallium is only enriched in the lavas (Fig. 4.6), where the fluids cooled down to the saturation temperature for Tl-bearing minerals. A previous study on ore deposit chemistry proposed that Tl only precipitates from solutions at temperature lower than 160 °C (Ewers and Keays, 1977). This temperature proposed by Ewers and Keays (1977) is close to the temperature at the boundary between transition zone and lava unit (<170 °C) predicted by the observation of Zn distribution.

As discussed above, hydrothermal fluid temperatures decreased from >350 °C in the main portion of the sheeted dikes to at least <270 °C at the bottom of the transition zone, and the fluids cooled to < 170 °C when they reached the boundary of transition zone and lava unit. Therefore, the high-temperature hydrothermal fluids were cooled (either conductively or by fluid mixing) throughout the transition zone and the lava unit.

5.2.2. Calculating the concentrations of the elements of interest in diffuse fluids

This section will use a mass balance to calculate the concentrations of the elements of interest in diffuse fluids. In this section, all fault breccia samples are considered as transition zone samples. The mass balance consisted of recharged seawater, rock samples from upper crust (lavas, transition zone samples, and dikes), high-temperature hydrothermal fluids, and diffuse fluids. The input data include the amount of the elements in recharged seawater and the amount of depletion the elements in the dikes. The output includes enrichment amount of the elements in lavas and/or transition zone samples, high-temperature hydrothermal fluids, and diffuse fluids.

Previous studies suggested that about 10% of the on-axis heat flux is carried by high-temperature fluids, and the other 90% are carried by diffuse fluids. Assuming that 100% of the on-axis fluids are initially high-temperature fluids, all of the elements mobilized from dikes would be carried by high-temperature fluids, following the mass balance of:

$$M_{SW}C_{SW}^{X} + M_{DK}\Delta C_{DK}^{X} = M_{HF}^{e}C_{HF}^{X} \qquad \textit{Equation 5.1}$$

Here M_{SW} , M_{DK}, and M_{HF}^{e} represent the mass of the recharged seawater, sheeted dikes, and high-temperature hydrothermal fluids. C_{SW}^{X} and C_{HF}^{X} are the concentrations of element X in the seawater and high-temperature hydrothermal fluids. ΔC_{DK}^{X} is the change of element X concentrations in dikes. The fluid/rock ratio

in Pito Deep is about 1 (Barker et al., 2010b; i.e., $M_{SW} = M_{HF}^{e} \approx M_{DK}$), therefore, the concentration of element X in high-temperature hydrothermal fluids can be calculated.

If diffuse fluids were generated by cooling high-temperature hydrothermal fluids, element X may precipitate in both lavas and the transition zone, or only in the transition zone. The mobilization of element X should follow the mass balance of Equation 5.2 (precipitation in lavas and the transition zone) or Equation 5.3 (precipitation in only the transition zone):

$$M_{SW}^{1}C_{SW}^{X} + M_{SW}^{2}C_{SW}^{X} + M_{DK}\Delta C_{DK}^{X} = M_{LT}\Delta C_{LT}^{X} + M_{HF}^{f}C_{HF}^{X} + M_{DS}C_{DS}^{X} \qquad \textit{Equation 5.2}$$

$$M_{SW}^{1}C_{SW}^{X} + M_{SW}^{2}C_{SW}^{X} + M_{DK}\Delta C_{DK}^{X} = M_{TR}\Delta C_{TR}^{X} + M_{HF}^{f}C_{HF}^{X} + M_{DS}C_{DS}^{X} \qquad \textit{Equation 5.3}$$

Here M_{SW}^{1} and M_{SW}^{2} represent the mass of the deep-recharged and shallow-recharged seawater (Fig. 5.2). M_{LT}, M_{TR}, M_{HF}^{f} and M_{DS} represent the mass of the lavas and the transition zone, the transition zone, high-temperature hydrothermal fluids after generating diffuse fluids, and diffuse fluids. C_{DS}^{X} is the concentration of element X in the diffuse fluids. ΔC_{LT}^{X} and ΔC_{TR}^{X} are the change of element X concentrations in lavas and the transition zone, and the transition zone. As introduced in Chapter 3, the thickness of the sheeted dike complex is about twice as thick as lava unit and the transition zone (Hayman and Karson, 2009; Heft et al., 2008). The transition zone in Pito Deep is on average one fifth of the thickness of the sheeted dike complex (Hayman and Karson, 2009; Heft et al., 2008), although this volume is poorly

constrained. Therefore, the mass relations among deep-recharged seawater, dikes, lavas and the transition zone, and the transition zone are assumed as $M_{SW}^{1} \approx M_{DK} \approx 2 M_{LT} \approx 5M_{TR}$. Moreover, the fluid mixing model should conserve fluid mass, that is,

$$M_{SW}^{1} + M_{SW}^{2} = M_{HF}^{f} + M_{DS} \qquad \textit{Equation 5.4}$$

If all high-temperature hydrothermal fluids were cooled to form diffuse fluids, M_{HF}^{f} is zero (Fig. 5.2, paths following solid lines).

Lowell et al. (2013) used fluid temperature and Mg concentration as tracers to trace the formation of diffuse fluids at EPR 9°50'N and JdFR at Main Endeavour (MEF) fields. Based on their results, they argued that the diffuse fluids are formed by conservative mixing (for temperature and Mg) at EPR 9°50'N, and conductive cooling of high-temperature fluids at JdFR. This study will use the mass ratios of deep-recharged seawater, shallow-recharged seawater, diffuse fluids, and high-temperature hydrothermal fluids from the results of Lowell et al. (2013) to calculate the composition of diffuse fluids generated at the Pito Deep.

The mass ratio of deep-recharged seawater, shallow-recharged seawater, diffuse fluids, and high-temperature hydrothermal fluids for fluid mixing was adopted from EPR 9°50'N (where diffuse fluids were interpreted to be generated by fluid mixing; Lowell et al., 2013) as

$$M_{SW}^{1} : M_{SW}^{2} : M_{HF}^{f} : M_{DS} \approx 1 : 14 : 0.1 : 14.9 \qquad \textit{Equation 5.5}$$

Lowell et al. (2013) also calculated the mass ratios of these four fluid members from MEF on the JdFR (where diffuse fluids were generated mainly by conductive cooling of high-temperature hydrothermal fluids), which yields the result as

$$M_{SW}^{1} : M_{SW}^{2} : M_{HF}^{f} : M_{DS} \approx 1 : 6 : 0.4 : 6.6 \qquad \textit{Equation 5.6}$$

The concentrations of end member hydrothermal fluids and diffuse fluids generated by fluid mixing and conductive cooling are calculated following the equations above. If the diffuse fluids were generated by fluid mixing, the calculated concentrations of the elements of interest in diffuse fluids are listed in Table 5.2. The concentrations of As and Tl in diffuse fluids calculated from mass balance equations are negative, which suggests additional sources other than recharged seawater is needed based on this calculation. If the additional source is particulates in seawater, the concentrations of As and Tl in seawater particulates are calculated (Table 5.2) assuming the particulates that reacted with crust were from the total recharged seawater (including both shallow-recharged and deep-recharged seawater).

Table 5.2. Calculation of the concentrations of the elements of interest in high-temperature hydrothermal fluids (C^X_{HF}) and diffuse fluids (C^X_{DS}) generated by fluid mixing in Pito Deep.

		Cu	Zn	As	Ag	Cd	Tl	Pb	Mo	Sb
	C^X_{SW} (ppt)	192	390	1725	2.16	67.2	14.28	2.07	9984	195.2
Mass normalized to deep-recharged seawater	M^1_{SW}	1	1	1	1	1	1	1	1	1
	M^2_{SW}	14	14	14	14	14	14	14	14	14
	M^f_{HF}	0.1	0.1	0.1	0.1	0.1	0.1	0.1	0.1	0.1
	M_{DS}	14.9	14.9	14.9	14.9	14.9	14.9	14.9	14.9	14.9
	M_{DK}	1	1	1	1	1	1	1	1	1
	M_{LT}	-	-	0.5	-	0.5	0.5	0.5	-	-
	M_{TR}	0.2	0.2	-	0.2	-	-	-	-	-
Median value of changes	ΔC^X_{DK} (ppm)	-52.3	-45.1	-0.098	-0.012	-0.06	-0.0074	-0.27	0.4	0.014
	ΔC^X_{LT} (ppm)	-	-	0.46	-	0.095	0.033	0.397		
	ΔC^X_{TR} (ppm)	184	114.5	-	0.021	-	-	-		
Calculation results	C^X_{HF} (ppm)	52.3	45.1	0.098	0.012	0.06	0.0074	0.27	0	0
	C^X_{DS} (ppb)	689.5	1187.6	*-7.78*	0.45	0.5	*-0.65*	2.99	0	0
particulates concentration of element X in bottom seawater (ppb)		-	-	7.73	-	-	0.64	-	30.0	1.21

Note: C^X_{SW} : element X concentration in seawater; M^1_{SW}, M^2_{SW}, M^f_{HF}, and M_{DS} are the mass of deep-recharged seawater, shallow-recharged seawater, high-temperature hydrothermal fluids, and diffuse fluids; M_{DK}, M_{TR}, and M_{LT} are the mass of dikes, transition zone, and lava and transition zone. ΔC^X_{DK}, ΔC^X_{TR}, and ΔC^X_{LT} are the median value of changes in dikes, transition zone, and lava unit and transition zone; C^X_{HF} and C^X_{DS} are the calculated concentration of element X in high-temperature fluids and diffuse fluids. Negative italic values are calculated from equations but not realistic in natural systems, which means additional sources of the elements are needed.

Table 5.3. Calculation of the concentrations of the elements of interest in high-temperature hydrothermal fluids (C^X_{DF}) and diffuse fluids (C^X_{DS}) generated by conductive cooling of high-temperature hydrothermal fluids in Pito Deep.

		Cu	Zn	As	Ag	Cd	Tl	Pb	Mo	Sb
	C^X_{SW} (ppt)	192	390	1725	2.16	67.2	14.28	2.07	9984	195.2
Mass normalized to deep-recharged seawater	M^1_{SW}	1	1	1	1	1	1	1	1	1
	M^2_{SW}	6	6	6	6	6	6	6	6	6
	M^f_{HF}	0.4	0.4	0.4	0.4	0.4	0.4	0.4	0.4	0.4
	M_{DS}	6.6	6.6	6.6	6.6	6.6	6.6	6.6	6.6	6.6
	M_{DK}	1	1	1	1	1	1	1	1	1
	M_{LT}	-	-	0.5	-	0.5	0.5	0.5	-	-
	M_{TR}	0.2	0.2	-	0.2	-	-	-	-	-
Median value of changes	ΔC^X_{DK} (ppm)	-52.3	-45.1	-0.098	-0.012	-0.06	-0.0074	-0.27	0.4	0.014
	ΔC^X_{LT} (ppm)	-	-	0.46	-	0.095	0.033	0.397		
	ΔC^X_{TR} (ppm)	184	114.5	-	0.021	-	-	-		
Calculation results	C^X_{HF} (ppm)	52.3	45.1	0.098	0.012	0.06	0.0074	0.27	0	0
	C^X_{DS} (ppb)	*-821.0*	630.7	*-24.1*	0.46	*-1.67*	*-1.81*	*-5.53*	0	0
particulates concentration of element X in bottom seawater (ppb)		774.1	-	22.7	-	1.57	1.71	5.2	75.7	3.2

Notes: symbols and italic values refer to Table 5.2.

If the diffuse fluids were generated by conductive cooling of high-temperature hydrothermal fluids, the calculated concentrations of the elements of interest in diffuse fluids are listed in Table 5.3. Compared with the fluid mixing model, a smaller fraction of high-temperature hydrothermal fluids cooled in conductive cooling model. Therefore, the results show that in a conductive cooling model, the amount of Cu, As, Cd, Tl and Pb in the high-temperature hydrothermal fluids are not sufficient for the

precipitation amount in the crust. It is highly unlikely that all these elements are supplied by particulates in seawater, which require a large amount of these elements in seawater particulates to react with the crust. However, the end-member fluids mass ratio was adopted from MEF, and the parameters from MEF (e.g., crust permeability, fluid temperature, etc.) Lowell et al. (2013) used to constrain the model might be different from Pito Deep. Thus, if there was a larger fraction of high-temperature hydrothermal fluids cooled in conductive cooling model than the adopted data from Lowell et al. (2013), conductive cooling could also happen. Combining the mass balance calculations results and the discussion on the profile of chalcophile elements distribution (Section 5.1), a fluid mixing model is favoured by this study to generate diffuse fluids in the Pito Deep.

5.2.3. Model robustness and uncertainties

The mass ratios of fluid members in fluid mixing and conductive cooling models were adopted from the study of the EPR 9°50' and MEF areas by Lowell et al. (2013). They used Mg and vent fluid temperature as tracers of the mass fractions of the end-members for comparison, and argued that EPR 9°50' diffuse fluids are generated by conservative mixing (for temperature and Mg), whereas MEF diffuse fluids are generated by conductive cooling. There are uncertainties from simply applying their data to the Pito Deep, where the parameters that Lowell et al (2013) used to constrain their model may be different from Pito Deep.

The models used to calculate the concentrations of diffuse fluids are based on considering the fault zone as transition zone. However, the fault zone in Area A is an

area of fluid mixing between a large amount of seawater and high-temperature hydrothermal fluids (Barker et al., 2010a). Moreover, the fluid/rock ratio in the fault zone is much larger than in the transition zone outside the fault zone. Therefore, in the conductive cooling model (Table 5.3), the precipitation amount of the elements of interest was enlarged by the anomaly of the fluid mixing in the fault zone.

Amongst all the elements of interest, Tl and As have the largest uncertainties of the concentrations determined. The median Tl content of the lavas is highly uncertain due to the large range of concentrations and small number of samples analysed. The relatively high uncertainty of the As concentration in MORB glasses is a source of uncertainty in determining the depletion and enrichment amount of As in the Pito Deep samples, which in turns affects the reliability of As concentrations calculations in fluid members. As an extreme example, if the As concentration in MORB glasses was ~0.15 ppm higher (the upper limit within the As concentration uncertainty in MORB glasses), the concentration of As in diffuse fluid would be 6.31 ppb and 0.89 ppb in fluid mixing and conductive cooling models respectively.

5.3. Conclusion

The purpose of this study was to trace on-axis diffuse fluid generation by studying the abundances of the chalcophile elements and Mo in the oceanic crust. The tectonic window into fast-spreading EPR crust at Pito Deep provides an opportunity to study the upper oceanic crust. By analyzing the chalcophile elements and Mo in the samples from the Pito Deep, the profiles of the distribution of the elements of interest in the upper crust are achieved. The following are the key conclusions of this work:

- Zinc, Cu, Ag, As, Cd, Tl, and Pb are mobilized by hydrothermal fluids from dikes to lavas and/or the transition zone. This observation is consistent with previous studies (for the subset of these elements previously studied) on fast-spreading EPR crust at Hole 504B, Hess Deep, and Hole 1256D. The enrichment of these elements in lavas and/or transition zone samples suggests that cooling of high-temperature hydrothermal fluids to form diffuse fluids occurred in this area of the oceanic crust. The distribution profiles of the elements show that the decrease of the solubilities of Cd, Pb, As and Tl react to a temperature drop more slowly compared to Cu, Zn, and Ag. Molybdenum and Sb are added into the crust by downwelling seawater (possibly carrying particulates) at Pito Deep.
- Based on previous estimates of the precipitation temperatures of Cu, Zn, and Tl-bearing sulphides, hydrothermal fluids temperature decreased from >350 °C to at least <270 °C at the transition zone, and the fluids cooled to < 170 °C when they reached the boundary of the transition zone and the lava unit. The cooling of high-temperature hydrothermal fluids occurred throughout the transition zone and lava unit.
- The Cd and Pb leached from the dikes appears to almost all be precipitated in the lavas and transition zone. Zinc, Cu and Ag only precipitate in the transition zone, while diffuse fluids are generated. With the uncertainties in the As concentration in MORB glasses, and very heterogeneous Tl contents of the lavas, it is not possible to determine whether the amounts of As and Tl leached from the dikes are sufficient or not to mass balance the enrichment in the lavas and the transition zone. If the As and Tl leached from the dikes is not sufficient to mass balance the amount precipitated in

the lavas, additional sources are needed, possibly particulates carried by bottom seawater.

- Based on the distribution profiles, the concentrations of the elements of interest in the high-temperature hydrothermal fluids and diffuse fluids from Pito Deep were calculated. The results from the conductive cooling of high-temperature hydrothermal fluids model for diffuse fluids generation show that the amount of the chalcophile elements mobilized from sheeted dikes is insufficient to achieve the amount of the precipitation in transition zone and lava unit. However, the fault zone in Area A is demonstrated to be an area of fluid mixing between a large amount of seawater and high-temperature hydrothermal fluids. The conductive cooling model has uncertainties from the end-member fluids ratios and fault zone anomalies, therefore, this study favours that the results of diffuse fluids calculated from the fluid mixing model rather than from the conductive cooling model.

5.4. Future Work

In addition to the conclusions listed in Section 5.3, several questions are also raised by this study which need to be tested in future work:

- There is limited data for the composition of diffuse fluids, especially for the suite of elements studied here, making the interpretations of this study challenging. Analyzing diffuse fluids for the elements of interest is a direct approach to test the robustness of the models in this study.
- The results of this study show that the Sn content of the rocks is generally not changed by hydrothermal alteration in the upper oceanic crust of Pito Deep.

Considering the low concentration of Sn in seawater (0.476 ppt; Table 4.1), this study predicts that the hydrothermal fluids contain little Sn (close to the concentration in seawater). To test this prediction, the Sn concentration in the high-temperature hydrothermal fluids needs to be analyzed.

➢ Among the 52 samples selected for analysis in this study, only four lava samples and five transition zone samples were included, which causes large uncertainties for the evaluation of the distribution profiles of the elements. This leads to large uncertainties in the calculation of hydrothermal fluids composition and diffuse fluids composition. Future studies should analyze more lava samples and transition zone samples to evaluate the robustness of the element distribution patterns observed in this study.

➢ As discussed in Section 4.2.2.2, there is a different degree of Ag depletion in dikes from Area A and Area B. The possible reasons for this observation could be (1) the small dataset of dikes analyzed in this study, or (2) the alteration of the minerals that contain Ag is different in Area A and Area B. To test these hypotheses, suggestions for future work are proposed as follows.

- If the different degree of Ag depletion in dikes from two areas is caused by the limitation of dike samples, analyzing more dike samples from both areas will build up a more robust dataset.
- There have been few studies on Ag partitioning into minerals other than sulphides. One study suggested that a small fraction of Ag may be hosted in silicate phase in mantle peridotites (Wang and Becker, 2015). Therefore, to understand how Ag depletion in dikes is affected by hydrothermal alteration,

determining the partition coefficient of Ag into which minerals and how Ag in these minerals was leached out is needed.

- The positive correlations between As and Sb in lavas and transition zone samples indicate that the As and Sb might partition into the same metal-sulphide minerals, possibly pyrite. To test this hypothesis, analyzing As and Sb in pyrites is needed. If the concentrations of As and Sb in pyrites correlate, the hypothesis that the As and Sb in the lavas and transition zone samples is controlled by the precipitation of pyrite would be supported.
- Based on mass balance of Mo and Sb in the upper oceanic crust at Pito Deep, recharging seawater is not the only source for the enrichment of these two elements in the crust. The abundance of As and Tl in the lavas and transition zone samples also suggests that there could be an additional source of these elements other than mobilization of these elements from the dikes. This thesis hypothesize that bottom seawater carries particulates which contain at least 30 ppb of Mo, 1.21 ppb of Sb, 7.73 ppb of As, and 0.64 ppb of Tl (Table 5.2). When the seawater enters the crust, small particulates would also enter and could react with the crust. To test this hypothesis, several approaches could be used.

  - The previous study analyzed Tl and Cs in nine samples from Hole 504B (Nielsen et al., 2006), and there were no positive correlations between Cs and Tl (in Section 4.2.2.2). Analyzing Mo, Sb, As, and Tl in samples from Hole 504B, where the crust is older and underwent longer time of off-axis low-temperature alteration. If the concentrations of these elements also do not show positive correlations with Cs, Rb, or alkalis (which are added into the

crust by off-axis low-temperature alteration), the enrichment of these elements would be interpreted to be due to on-axis hydrothermal processes.

- Analyzing Mo, Sb, As, and Tl in samples from Hess Deep, where the crust is younger and underwent a shorter time of off-axis low-temperature alteration. If the abundances of these elements in Hess Deep also suggest that recharging seawater and leaching from the dikes could not mass balance the enrichment of these elements in lavas and/or the transition zone, the hypothesis that they are supplied by particulates carried by bottom seawater would be supported.
- Analyzing bulk (i.e., unfiltered) bottom seawater from the surrounding areas of hydrothermal vent axis, where the seawater might carry large amount of particulates (e.g., particulates from sediments, scavenging from seawater). If the concentration of Mo, Sb, As and Tl of these seawater samples are consistent with the calculation results from this study, the additional source for such elements is likely to be particulates in bottom seawater.

Bibliography

Abbyad, P., Tromp, J, Lam J., Salin, E., 2001. Optimization of the technique of standard additions for inductively coupled plasma mass spectrometry. Journal of Analytical Atomic Spectrometry, 16 (5), 464-469.

Alt, J.C., 1995. Subseafloor processes in mid-ocean ridge hydrothermal systems. In Humphris, S.E., Zierenberg, R.A., Mullineaux, L.S., and Thomson, R.E. (Eds.) *Seafloor hydrothermal systems: physical, chemical, biological and geological interactions*, Geophysical Monograph Series, vol. 91, pp. 85-114. Washington, DC: American Geophysical Union.

Alt, J.C., Anderson, T.F., Bonnell, L., Muehlenbachs, K., 1989. Mineralogy, chemistry, and stable isotopic compositions of hydrothermally altered sheeted dikes: ODP Hole 504B, Leg 111. In: Becker, K; Sakai, H; et al. (Eds.), Proceedings of the Ocean Drilling Program, Scientific Results, College Station, TX (Ocean Drilling Program), 111, 27-40,

Alt, J.C., Emmermann, R., 1985. Geochemistry of hydrothermally altered basalts: Deep Sea Drilling Project Hole 504B, Leg 83, in: Anderson, R.N., Honnorez, J., Becker, K., et al. (Eds.), Initial Reports of DSDP, 83. U.S. Govt. Printing Office, Washington, 249–262.

Alt, J.C., Honnorez, J., Laverne, C., and Emmermann, R., 1986. Hydrothermal alteration of a 1 km section through the upper oceanic crust. DSDP Hole 504B: Mineralogy, chemistry and evolution of seawater-basalt interactions. Journal of Geophysical Research, 91, 309-335.

Alt, J.C., Laverne, C., Coggon, R.M., Teagle, D.A.H., Banerjee, N.R., Morgan, S., Smith-Duque, C.E., Harris, M., Galli, L., 2010. Subsurface structure of a submarine hydrothermal system in ocean crust formed at the East Pacific Rise, ODP/IODP Site 1256. Geochemistry, Geophys. Geosystems 11, 1–28. doi:10.1029/2010GC00314

Alt, J.C., Laverne, C., Vanko, D., Tartarotti, P., Teagle, D.A.H., Bach, W., Zuleger, E., Erzinger, J., Honnorez, J., 1996. Hydrothermal alteration of a section of upper oceanic crust in the eastern equatorial Pacific: a synthesis of results from DSDP/ ODP Legs 69, 70, 83, 111, 137, 140, 148 at Site 504B. In: Alt, J.C., Kinoshita, H., Stokking, L.B., Michael, P.J. (Eds.), Proc. ODP, Scientific Results, vol. 148. Ocean Drilling Program, College Station, TX, pp. 417–434.

Amcoff, O., 1984, Distribution of silver in massive sulphide ores. Mineralium Deposita, 19, 63-69.

Bach, W., Bernhard, P.E., Hart, S.R., Blusztajn, J.S., 2003. Geochemistry of hydrothermally altered oceanic crust: DSDP/ODP Hole 504B-Implications for seawater-crust exchange budgets and Sr-and Pb-isotopic evolution of the mantle. Geochemistry, Geophys. Geosystems 4, 40–55. doi:10.1029/2002GC000419

Bach, W., Humphris, S.E., and Fisher, A.T., 2004. Fluid flow and fluid-rock interaction within the oceanic crust: reconciling geological, geochemical and geophysical observations. In Wilcock, W., DeLong, E., Kelley, D., Baross, J., Cary, C. (Eds.) *The Subseafloor Biosphere at Mid-Ocean Ridges.* Geophysical Monograph 144, 99-117, American Geophysical Union.

Baker, E.T., Massoth, G.J., Walker, S.L., and Embley, R.W., 1993, A method for quantitatively estimating diffuse and discrete hydrothermal discharge, Earth and Planetary Science Letters, 118, 235-249.

Barker, A.K., Coogan, L.A., Gillis, K.M., Weis, D., 2008. Strontium isotope constraints on fluid flow in the sheeted dike complex of fast spreading crust: Pervasive fluid flow at Pito Deep. Geochemistry, Geophys. Geosystems 9, Q06010, doi:10.1029/2007GC001901

Barker, A.K., Coogan, L.A., Gillis, K.M., Hayman, N.W., Weis, D., 2010a. Direct observation of a fossil high-temperature, fault-hosted, hydrothermal upflow zone in crust formed at the East Pacific Rise. Geology 38, 379–382. doi:10.1130/G30542.1

Barker, A.K., Coogan, L.A., Gillis, K.M., 2010b. Insights into the behaviour of sulphur in mid-ocean ridge axial hydrothermal systems from the composition of the sheeted dyke complex at Pito Deep. Chem. Geol. 275, 105–115. doi:10.1016/j.chemgeo.2010.05.003

Beary, E.S. and Paulsen, P.J., 1993. Selective application of chemical separations to isotope dilution inductively coupled plasma mass spectrometric analyses of standard reference materials. Analytical Chemistry, 65(11), 1602 - 1608.

Bourcier, W.L., and Barnes, H.L., 1987, Ore solution chemistry: VII. Stabilities of chloride and bisulfide complexes of zinc to 350°C. Economic Geology, 82, 1839–1863.

Bowers, T.S., Von Damm, K.L., and Edmond, J.M., 1985, Chemical evolution of mid-ocean ridge hot springs, Geochimica et Cosmochimica Acta 49, 2239-2252.

Brewer, F.M., Cox, J.D., Morris, D.F.C., 1955. The occurrence of germanium in blende. Geochimica et Cosmochimica Acta, 8, 131-136.

Bruland, K.W., Middag, R., Lohan, M.C., 2014. Treatise on Geochemistry Controls of trace metals in seawater, 2nd Ed., The Oceans and Marine Geochemistry. Elsevier. doi:10.1016/B978-0-08-095975-7.00602-1

Butterfield, D.A., Jonasson, I.R., Massoth, G.J., et al., 1997. Seafloor eruptions and evolution of hydrothermal fluid chemistry. Philosophical Transactions of the Royal Society Series A 355: 369-386.

Butterfield, D.A., Massoth, G.J., McDuff, R.E., Lupton, J.E., and Lilley, M.D., 1990, Geochemistry of hydrothermal fluids from Axial Seamount hydrothermal emissions study vent field, Juan de Fuca Ridge: subseafloor boiling and subsequent fluid-rock interaction, Journal of Geophysical Research, 95 (B8), 12895-12921.

Butterfield, D.A., and Massoth, G.J., 1994, Geochemistry of north Cleft segment vent fluids: Temporal changes in chlorinity and their possible relation to recent volcanism. Journal of Geophysical Research, 99, 4951-4968.

Cann J.R., Strens M.R., and Rice A., 1985. A simple magma-driven thermal balance model for the formation of volcanogenic massive sulphides. Earth and Planetary Science Letters, 76: 123-134

Chang, T.L., Qian, Q.Y., Zhao, M.T., and Wang, J., 1993. The isotopic abundance of Antimony. International Journal of Mass Spectrometry and Ion Processes, 123, 77-82.

Chang, T.L., Xiao, Y.K., 1991. The atomic weight of Indium. Chinese Chemical Letters, 2, 407-410.

Clarke, W.B., Beg, M.A., Craig, H., 1969, Excess ^{3}He in the sea: evidence for terrestrial primordial helium. Earth and Planetary Science Letters, 6: 213-220.

Cogley, J.G.,1984, Continental margins and the extent and number of the continents. Reviews of Geophysics and Space Physics 22, 101–122.

Constantin, M., Hékinian, R., Ackermand, D., and Stoffers, P., 1995, Mafic and ultramafic intrusions in upper mantle peridotites from fast spreading centers of the Easter Microplate (South East Pacific). In: Vissers, R.L.M., Nicolas, A. (eds.) Mantle and lower crustal exposures in Ocean Ridges and in Ophiolites, Kluwer, pp 71– 120.

Coogan, L.A., Dosso, S., 2012. An internally consistent, probabilistic, determination of ridge-axis hydrothermal fluxes from basalt-hosted systems. Earth Planet. Sci. Lett. 323-324, 92-101.

Cooper, M.J., Elderfield, H. and Schultz, A., 2000. Diffuse hydrothermal fluids from Lucky Strike hydrothermal vent field: Evidence for a shallow conductively heated system. Journal of Geophysical Research, 105: 19369-19375

Cooper, K.M., 2007. Data report: trace element analyses in whole-rock basement samples, Site 1256, ODP Leg 206. *In* Teagle, D.A.H., Wilson, D.S., Acton, G.A., and Vanko, D.A. (Eds.), *Proc. ODP, Sci. Results*, 206: College Station TX (Ocean Drilling Program), 1-11. doi: 10.2973/odp.proc.sr.206.010.2007.

Crowell, B.W., Lowell, R.P., and Von Damm, K.L., 2008. A model for the production of sulfur floc and "snowblower" events at mid-ocean ridges. Geochemistry Geophysics Geosystems 9, Q10T02, http://dx.doi.org/10.1029/2008GC002103

DeMets, C., Gordon, R.G., and Argus, D.F., 2010, Geologically current plate motions. Geophysical Geophysical Journal International 181: 1–80.

Devillers, C., Lecomte, T., and Hagemann, R., 1983. Absolute isotope abundances of Tin. International Journal of Mass Spectrometry and Ion Physics, 50, 205-217.

Donat, J.R., Bruland, K.W., 1995. Trace elements in the oceans. Trace Elem. Nat. Waters 247–281. doi:10.1007/978-94-010-9488-7_11

Edmond, J.M., Measures, C., McDuff, R.E., et al., 1979a. Ridge crest hydrothermal activity and the balances of the major and minor elements in the ocean: the Galapagos data. Earth and Planetary Science Letters 46: 1-18.

Edmond, J.M., Measures, C., Mangum, B., et al., 1979b. On the formation of metal-rich deposits at ridge crests. Earth Planetary Science Letters, 46: 19-30.

Edmond, J.M., Von Damm, K.L., McDuff, R.E., and Measures, C.I., 1982. Chemistry of hot springs on the East Pacific Rise and their effluent dispersal. Nature 297: 187-191.

Eggins, S.M., Woodhead, J.D., Kinsley, L.P.J., Mortimer, G.E., Sylvester, P., Mcculloch, M.T., Hergt, J.M., Handler, M.R., 1997. A simple method for the precise determination of ≥40 trace elements in geological samples by ICPMS using enriched isotope internal standardization. Chemical Geology, 134, 311-326.

Elderfield, H. and Schultz, A., 1996. Mid-ocean hydrothermal fluxes and the chemical composition of the ocean. Annual Review of Earth and Planetary Sciences, 24: 191-224.

Evans, H. and Giglio, J., 1993. Interferences in inductively coupled plasma mass spectrometry - A Review. Journal of Analytical Atomic Spectrometry, 8, 1–18.

Ewers, R.G. and Keays, R.R., 1977. Volatile and precious metal zoning in the Broadlands geothermal field, New Zealand. Economic Geology, 72, 1337–1354.

Fisher, A.T., 1998. Permeability within basaltic oceanic crust. Reviews of Geophysics, 36, 2, 143-182.

Fleischer, M., 1955. Minor elements in some sulfide minerals. Economic Geology, 50, 970-1024.

Fouquet, Y., Auclair, G., Cambon, P., and Etoubleau, J., 1988. Geological setting and mineralogical and geochemical investigations on sulfide deposits near 13°N on the East Pacific Rise. Marine Geology, 84, 145-178.

Fouquet, Y., Wafik, A., Cambon, P., Mevel, C., Meyer, G., and Gente, P., 1993. Tectonic setting and mineralogical and geochemical zonation in the Snake Pit sulfide deposit (Mid-Atlantic Ridge at 23°N). Economic Geology 88, 2018-2036.

Fournier, R.O., 1985. The behavior of silica in hydrothermal solutions. Reviews in Economic Geology and Society of Economic Geologist 2, 45–62.

Foustoukos, D.I., N.J. Pester, K. Ding, and W.E. Seyfried Jr. 2009. Dissolved carbon species in associated diffuse and focused flow hydrothermal vents at the Main Endeavour Field, Juan de Fuca Ridge: Phase equilibria and kinetic constraints. Geochemistry Geophysics Geosystems 10, Q10003.

Francheteau, J., Patriat, P., Segoufin, J., Armijo, R., Doucoure, M., Yelleschaouche, A., Zukin, J., Calmant, S., Naar, D. F., and Searle, R. C., 1988. Pito and Orongo fracture zones: The northern and southern boundaries of the Easter microplate (southeast Pacific), Earth and Planetary Science Letters, 89: 363–374, doi:10.1016/0012-821X(88)90123-9.

Gao, Y., Huang, J., and Casey, J.F., 2009. Data report: trace element geochemistry of oceanic crust formed at superfast-spreading ridge, Hole 1256D. *In* Teagle, D.A.H., Alt, J.C., Umino, S., Miyashita, S., Banerjee, N.R., Wilson, D.S., and the Expedition 309/312 Scientists, *Proc. IODP,* 309/ 312: Washington, DC (Integrated Ocean Drilling Program Management International, Inc.). doi:10.2204/iodp.proc.309312.202.2009.

German C.R., Livermore R.A., Baker E.T., Bruguier, N.I., Connelly, D.P., Cunningham, A.P., Morris, P., Rouse, I.P., Statham, P.J., Tyler, P.A., 2000. Hydrothermal plumes above the East Scotia Ridge: An isolated high-latitude back-arc spreading centre. Earth and Planetary Science Letters 184: 241-250

German, C.R., Bennett, S.A., Connelly, D.P., Evans, A.J., Murton, B.J., Parson, L.M., Prien, R.D., Ramirez-Llodra, E., Jakuba, M., Shank, T.M., Yoerger, D.R., Baker, E.T., Walker, S.L., Nakamura, K., 2008. Hydrothermal activity on the southern Mid-Atlantic Ridge: Tectonically- and volcanically-controlled venting at 4–5°S. Earth and Planetary Science Letters, 273, 332-344.

German, C. and Seyfried, W., 2014. Hydrothermal processes. In Holland, H. and Turekian K. (Eds.): *Treatise on Geochemistry (Second Edition), Volume 8: The Oceans and Marine Geochemistry*, 191-233. Elsevier Ltd.

Gillis, K.M., Muehlenbachs, K., Stewart, M., Gleeson, T., Karson, J.A., 2001. Fluid flow patterns in fast spreading East Pacific Rise crust exposed at Hess Deep. J. Geophys. Res. 106, 311–329.

Goldschmidt, V.M., 1937, The principles of distribution of chemical elements in minerals and rocks, Journal of the Chemical Society, 655-673.

Goldschmidt, V.M., and Peters, C., 1933. The geochemistry of Germanium. Nachrichten von der Gesellschaft der Wissenschaften zu Gottingen, Mathematisch - Physikalische Klasse, 141-166.

Hackbarth, C.J., and Petersen, U., 1984, A fractional crystallization model for the deposition of argentian tetrahedrite. Economic Geology, 79, 448-460.

Hannington, M.D., 2014, Volcanogenic massive sulfide Deposits. In: Turekian, H.D.H.K. (Ed.), Treatise on Geochemistry (Second Edition). Elsevier, Oxford, pp. 463–488. doi:http://dx.doi.org/10.1016/B978-0-08-095975-7.01120-7.

Hannington, M.D., Galley, A.G., Herzig, P.M., and Petersen, S., 1998, Comparison of the TAG mound and stockwork complex with Cyprus-type massive sulfide deposits, In Herzig, P.M., Humphris, S.E., Miller, D.J., and Zierenberg, R.A. (Eds.), Proceedings of the Ocean Drilling Program, Scientific Results, 158, 389-415. College Station, TX (Ocean Drilling Program).

Hannington, M.D., Herzig, P., Scott, S., Thompson, G., and Rona, P., 1991, Comparative mineralogy and geochemistry of gold-bearing sulfide deposits on the mid-ocean ridges. Marine Geology 101, 217–248.

Hannington, M.D., Tivey, M.K., Larocque, A.C.L., Petersen, S., and Rona, P.A., 1995. The occurrence of gold in sulfide deposits of the TAG Hydrothermal Field, Mid-Atlantic Ridge. Canadian Mineralogist 33: 1285-1310.

Hawley, J.E., 1952, Spectrographic studies of pyrite in some Eastern Canadian gold mines. Economic Geology, 47, 260-304.

Hayman, N.W., and Karson, J.A., 2009, Crustal faults exposed in the Pito Deep Rift: Conduits for hydrothermal fluids on the southeast Pacific Rise, Geochemistry, Geophysics, Geosystems, 10 (2), doi:10.1029/2008GC002319.

Haymon, R.M., 1983, Growth history of hydrothermal black smoker chimneys, Nature 301, 695-698, doi: 10.1038/301695a0.

Haymon, R.M., and Kastner, M., 1981, Hot spring deposits on the East Pacific Rise at 21°N: Preliminary description of mineralogy and genesis. Earth and Planetary Science Letters. 53, 363-381.

Heft, K.L., Gillis, K.M., Pollock, M.A., Karson, J.A., Klein, E.M., 2008. Role of upwelling hydrothermal fluids in the development of alteration patterns at fast spreading ridges: Evidence from the sheeted dike complex at Pito Deep. Geochemistry, Geophysics, Geosystems 9. doi:10.1029/2007GC001926

Heinrichs, H., Schulz-Dobrick, B., Wedepohl, K.H., 1980. Terrestrial geochemistry of Cd, Bi, Tl, Pb, Zn and Rb. Geochim. Cosmochim. Acta 44, 1519–1533. doi:10.1016/0016-7037(80)90116-7

Helgeson, H.C., 1969, Thermodynamics of hydrothermal systems at elevated temperatures and pressures. American Journal of Science, 267, 729.

Hékinian, R., Francheteau, J., Armijo, R., Cogne, J.P., Constantin, M., Girardeau, J., Hey, R., Naar, D.F., and Searle, R., 1996, Petrology of the Easter microplate region in the South Pacific. Journal of Volcanology and Geothermal Research 72(3–4): 259–289.

Honnorez, J., Alt, J.C., Honnorez-Guerstein, B.M., Laverne, C., Muehlenbachs, K., Ruiz, J., and Saltzman, E., 1985, Stockwork-like sulfide mineralization in young oceanic crust: Deep Sea Drilling Project Hole 504B, In Anderson, R.N., Honnorez, J., Becker, K., and Shipboard Science Party (Eds.), Initial Reports, Deep Sea Drilling Project, 83: Washington (U.S. Government Printing Office).

Huang, M., and Masuda, A., 1997. Measurement of the atomic weight of Ruthenium by Negative Ionization Mass Spectrometry. Analytical Chemistry, 69, 1135-1139.

Humphris, S.E., Alt, J.C., Teagle, D.A.H., and Honnorez, J.J., 1998. Geochemical changes during hydrothermal alteration of basement in the stockwork beneath the active tag hydrothermal mound. Proceedings of Ocean Drilling Program, Scientific Results, vol. 158, pp. 255-276.

Huston, D.L., Taylor, T., Fabray, J., and Patterson, D.J., 1992, A comparison of the geology and mineralization of the Balcooma and Dry River South volcanic-hosted massive sulfide deposits, Northern Queensland. Economic Geology, 87, 785-811.

Janecky, D.R., and Seyfried, W.E., 1984, Formation of massive sulfide deposits on oceanic ridge crests: Incremental reaction models for mixing between hydrothermal solutions and seawater. Geochimica et Cosmochimica Acta 48, 2723–2738.

Jenner, F.E., O'Neill, H.S.C., 2012. Major and trace analysis of basaltic glasses by laser-ablation ICP-MS. Geochemistry, Geophys. Geosystems 13, n/a–n/a. doi:10.1029/2011GC003890

Jochum, K.P., Nohl, U., Herwig, K., Lammei, E., Stoll, B., and Hofmann, A.W., 2005. GeoRem: A new geochemical database for reference materials and isotopic standards. Geostandards and Geoanalytical Research, 29 (3), 333-338.

Jochum, K.P., and Verma, S.P., 1996. Extreme enrichment of Sb, Tl and other trace elements in altered MORB. Chem. Geol. 130, 289–299. doi:10.1016/0009-2541(96)00014-9

Johnson, N.E., Craig, J.R., and Rimstead, J.D., 1986, Compositional trends in tetrahedrite. Canadian Mineralogist, 24,385-397.

Jowitt, S.M., Jenkin, G.R.T., Coogan, L.A., Naden, J., 2012. Quantifying the release of base metals from source rocks for volcanogenic massive sulfide deposits: Effects of protolith composition and alteration mineralogy. J. Geochemical Explor. 118, 47–59. doi:10.1016/j.gexplo.2012.04.005

Karson, J.A., 2002, Geologic structure of the uppermost oceanic crust created at fast- to intermediate-rate spreading centers, Annual Reviews of Earth and Planetary Sciences, 30, 347–384, doi: 10.1146/annurev.earth.30.091201.141132

Karson, J.A., 2005, Internal structure of the upper oceanic crust generated at fast to intermediate rates: the view from tectonic windows in the Pacific. In: EOS Trans AGU 86 (52), Fall Meet pp T23F-03.

Karson, J. A., Francheteau, J., Gee, J.S., Gillis, K.M., Hayman, N.W., Hékinian, R., Hey, R.N., Hurst, S.D., Klein, E.M., Naar, D.F., and Varga, R.J., 2005, Nested-Scale

Investigation of Tectonic Windows into Super-Fast Spread Crust Exposed at Pito Deep Rift, Easter Microplate, SE Pacific: InterRidge News, 14: 5–8.

Kelley, D.S., Baross, J.A., and Delaney, J.R., 2002. Volcanoes, fluids, and life at mid-ocean ridge spreading centers. Annual Review of Earth and Planetary Sciences 30: 385-491.

Large, R.R., 1992, Australian volcanic-hosted massive sulfide deposits: features, styles, and genetic models. Economic Geology, 87, 471-510.

Larson, B.I., Houghton, J.L., Lowell, R.P., Farough, A., and Meile, C.D., 2015, Subsurface conditions in hydrothermal vents inferred from diffuse flow composition, and models of reaction and transport. Earth and Planetary Science Letters, 424, 245-255.

Lowell, R.P., Crowell, B.W., Lewis, K.C., and Liu, L., 2008. Modeling multiphase, multicomponent processes at oceanic spreading centers. pp. 15–44 In R.P. Lowell, J.S. Seewald, A. Metaxas, and M.R. Perfit (Eds.) *Magma to Microbe: Modeling Hydrothermal Processes at Ocean Spreading Centers*. Geophysical Monograph Series, vol. 178, American Geophysical Union, Washington, DC.

Lowell, R. P., Farough, A., Hoover, J., and Cummings, K., 2013, Characteristics of magma-driven hydrothermal systems at oceanic spreading centers, Geochemistry, Geophysics, Geosystems, 14, 1756–1770, doi:10.1002/ggge.20109.

Lowell, R.P., and Yao, Y., 2002, Anhydrite precipitation and the extent of hydrothermal recharge zones at ocean ridge crests, Journal of Geophysical Research, 107(B9), 2183, doi:10.1029/2001JB001289.

Lowell, R.P., Yao, Y., and Germanovich, L.N., 2003, Anhydrite precipitation and the relationship between focused and diffuse flow in seafloor hydrothermal systems, Journal of Geophysical Research, 108 (B9), 2424, doi:10.1029/2002JB002371

Maris, C.R.P., Bender, M.L., Froelich, P.N., Barnes, R., Luedtke, N.A., 1984, Chemical evidence for advection of hydrothermal solutions in the sediments of the Galapagos Mounds Hydrothermal Field. Geochimica et Cosmochimica Acta, 48: 2331-2346

Martin, J.T., and Lowell, R.P., 2000, Precipitation of quartz during high-temperature, fracture-controlled hydrothermal upflow at ocean ridges: Equilibrium versus linear kinetics, Journal of Geophysical Research, 105, 869–882.

Martinez, F., Naar, D. F., Reed, T. B., and Hey, R. N., 1991, 3-dimensional Seamarc II, gravity, and magnetics study of large-offset rift propagation at the Pito Rift, Easter Microplate, Marine Geophysical Researches, 13: 255–285, doi:10.1007/ BF00366279.

McLaren, J.W., Beauchemin, D., and Berman, S.S., 1987. Application of isotope dilution inductively coupled plasma mass spectrometry to the analysis of marine sediments. Analytical Chemistry, 59 (4), 610–613.

Metz, S., and Trefry, J.H., 2000, Chemical and mineralogical influences on concentrations of trace metals in hydrothermal fluids. Geochimica et Cosmochimica Acta, 64 (13), 2267-2279.

Miller, J.W., and Craig, J.R., 1983, Tetrahedrite-tennantite series composition variations in the Cofer deposit, Mineral district, Virginia. American Mineralogist, 68, 227-234.

Mittelstaedt, E., Escartin, J., Gracias, N., Olive, J.A., Barreyre, T., Davaille, A., Cannat, M., Garcia, R., 2012. Quantifying diffuse and discrete venting at the Tour Eiffel vent site, Lucky Strike hydrothermal field. Geochemistry, Geophysics, Geosystems, 13, Q04008.

Moore, L.J., Machlan, L.A., Shields, W.R., and Garner, E.L., 1974. Internal normalization techniques for high accuracy isotope dilution analyses: application to Molybdenum and Nickel in standard reference materials. Analytical Chemistry, 46, 1082-1089.

Mosier, D.L., Singer, D.A., and Salem, B.B., 1983, Geologic and grade-tonnage information on volcanic-hosted copper-zinc-lead massive sulfide deposits. US Geological Survey Open-File Report 83–89. Denver, CO: US Geological Survey.

Mottl, M.J., 1983a. Metabasalts, axial hot springs, and the structure of hydrothermal systems at mid-ocean ridges, Geological Society of America Bulletin, 94, 161-180.

Mottl, M.J., 1983b. Hydrothermal Processes at Seafloor Spreading Centers: Application of Basalt-Seawater Experimental Results. In: Rona, P.A., Bostrom, K., Laubier, L., and Smith, K.L. (Eds.), Hydrothermal Processes at Seafloor Spreading Centers. NATO Conference Series, 199-223.

Mottl, M.J., 2003. Partitioning of energy and mass fluxes between mid-ocean ridge axes and flanks at high and low temperature. In Halbach, P.E., Tunnicliffe, V., and

Hein, J.R. (Eds.) *Energy and Mass Transfer in Marine Hydrothermal Systems*, pp. 271–287. Berlin: Dahlem University Press.

Mottl, M.J., Holland, H.D., and Corr, R.S., 1979, Chemical exchange during hydrothermal alteration of basalt by seawater: I. Experimental results for Fe, Mn, and sulfur species. Geochimica et Cosmochimica Acta 43, 869–884.

Mottl, M.J., and Wheat, C.G., 1994, Hydrothermal circulation through mid-ocean ridge flanks: fluxes of heat and magnesium. Geochimica et Cosmochimica Acta, 58: 2225-2237

Mutter, C.Z., and Mutter, J.C., 1993, Variations in thickness of Layer 3 dominated oceanic crustal structure. Earth and Planetary Science Letters 117, 295–317.

Naar, D. F., and Hey, R. N., 1991, Tectonic evolution of the Easter Microplate, Journal of Geophysical Research, 96: 7961–7993, doi:10.1029/90JB02398.

Naar, D. F., Martinez, F., Hey, R.N., Reed, T. B., and Stein, S., 1991, Pito Rift: How a large-offset rift propagates, Marine Geophysical Research, 13: 287–309, doi:10.1007/BF00366280.

Nielsen, S.G., Rehkamper, M., Teagle, D.A.H., Butterfield, D.A., Alt, J.C., Halliday, A.N., 2006, Hydrothermal fluid fluxes calculated from the isotopic mass balance of thallium in the ocean crust. Earth and Planetary Science Letters, 251: 120-133.

Nomura, M., Kogure, K., and Okamoto, M., 1983. Isotopic abundance ratios and atomic weight of Zirconium. International Journal of Mass Spectrometry and Ion Physics, 50, 219-227.

Olesik, J.W., 2014. Inductively Coupled Plasma Mass Spectrometers. Treatise on Geochemistry. Elsevier Ltd. doi:10.1016/B978-0-08-095975-7.00201-1

Patten, C.G.C., Pitcairn, I.K., Teagle, D.A.H., Harris, M., 2016. Sulphide mineral evolution and metal mobility during alteration of the oceanic crust: Insights from ODP Hole 1256D. Geochim. Cosmochim. Acta 193, 132–159. doi:10.1016/j.gca.2016.08.009

Pedersen, R.B., Rapp, H.T., Thorseth, I.H., Lilley, M.D., Barriga, F.J.A.S., Baumberger, T., Flesland, K., Fonseca, R., Früh-Green, G.L., and Jorgensen, S.L., 2010. Discovery of a black smoker vent field and vent fauna at the Arctic Mid-Ocean Ridge. Nature Communications 1: Article number: 126.

Penrose Conference Participants, 1972, Penrose field conference on ophiolites. Geotimes 17, 24–25.

Perk, N. W., Coogan, L.A., Karson, J. A., Klein, E. M., and Hanna, H. D., 2007, Petrology and geochemistry of primitive lower oceanic crust from Pito Deep: Implications for the accretion of the lower crust at the southern East Pacific Rise, Contributions to Mineralogy and Petrology, 154, doi:10.1007/s00410-007-0210-z.

Pollock, M.A., 2007. Geochemistry of dikes and lavas from tectonic windows. PhD Thesis, Duke University.

Pollock, M. a., Klein, E.M., Karson, J. a., Coleman, D.S., 2009. Compositions of dikes and lavas from the Pito Deep Rift: Implications for crustal accretion at superfast spreading centers. J. Geophys. Res. 114, B03207. doi:10.1029/2007JB005436

Ramondenc, P., Germanovich, L. N., Von Damm, K. L., and Lowell, R.P., 2006, The first measurements of hydrothermal heat output at 9°50′N, East Pacific Rise, Earth and Planetary. Science Letters, 245, 487–497, doi:10.1016/j.epsl.2006.03.023.

Rogers AD, Tyler PA, Connelly DP, et al. (2012) The discovery of new deep-sea hydrothermal vent communities in the Southern Ocean and implications for biogeography. PLOS Biology 10: e1001234.

Rona, P. A., and D. A. Trivett, 1992, Discrete and diffuse heat transfer at ASHES vent field, Axial Volcano, Juan de Fuca Ridge, Earth and Planetary Science Letters, 109,57–71, doi:10.1016/ 0012-821X(92)90074-6.

Rosman, K.J.R., Barnes, I.L., Moore, L.J., and Gramlich, J.W., 1980. Isotope composition of Cd, Ca, and Mg in the Brownfield Chrondrite. Geochemical Journal, 14, 269-277.

Rosman, K.J.R., Loss, R.D., and DeLaeter, J.R., 1984. The isotopic composition of Tin. International Journal of Mass Spectrometry and Ion Processes, 56, 281-291.

Rudnicki, M. D., and H. Elderfield, 1992, Theory applied to the Mid-Atlantic Ridge hydrothermal plumes: The finite- difference approach, Journal of Volcanology and Geothermal Research, 50, 161–172, doi:10.1016/0377-0273(92)90043-D

Schultz, A., Delaney, J.R., and McDuff, R.E., 1992. On the partitioning of heat flux between diffuse and point-source seafloor venting. Journal of Geophysical Research, 97: 12299-12314.

Schultz, A., and Elderfield, H., 1997. Controls on the physics and chemistry of seafloor hydrothermal circulation. Philosophical Transactions of Royal Society of London, 355: 387-425.

Seewald, J.S., and Seyfried Jr., W.E., 1990, The effect of temperature on metal mobility in subseafloor hydrothermal systems: Constraints from basalt alteration experiments, Earth and Planetary Science Letters, 101, 388-403.

Seyfried Jr., W.E., Berndt, M.E. and Seewald, J.S., 1988. Hydrothermal alteration processes at mid-ocean ridges: Constraints from diabase alteration experiments, hot-spring fluids and composition of the oceanic crust, Canadian Mineralogist, 26: 787-804.

Seyfried Jr., W.E., and Bischoff, J.L., 1979. Low temperature basalt alteration by seawater: an experimental study at 70°C and 150°C. Geochimica et Cosmochimica Acta, 43: 1937-1947

Seyfried, W.E. Jr., and Ding, K., 1993, The effect of redox on the relative solubilities of copper and iron in Cl-bearing aqueous fluids at elevated temperatures and pressures: An experimental study with application to subseafloor hydrothermal systems. Geochimica et Cosmochimica Acta 57, 1905-1917.

Seyfried, W.E. Jr., and Ding, K., 1995, Phase equilibria in subseafloor hydrothermal systems: A review of the role of redox, temperature, pH and dissolved Cl on the chemistry of hot spring fluids at mid-ocean ridges. In: Humphris, S.E., Zierenberg, R.A., Mullineaux, L.S., Thomson, R.E. (Eds.), Seafloor hydrothermal systems: physical, chemical, biological, and geological interactions. Geophysical Monograph 91, 248-272. American Geophysical Union.

Seyfried, W.E. Jr., Ding, K., and Berndt, M.E., 1991, Phase equilibria constraints on the chemistry of hot spring fluids at mid-ocean ridges, Geochimica et Cosmochimica Acta, 5.5, 3559-3580.

Seyfried, W.E. Jr., Seewald, J.S., Berndt, M.E., Ding, K., and Foustoukos, D.I., 2003, Chemistry of hydrothermal vent fluids from the Main Endeavour Field, northern Juan de Fuca Ridge: geochemical controls in the aftermath of June 1999 seismic

events, Journal of Geophysical Research, 108 (B9), 2429, doi:10.1029/2002JB001957.

Shank, T.M., D.J. Fornari, K.L. Von Damm, M.D. Lilley, R.M. Haymon, and R.A. Lutz. 1998. Temporal and spatial patterns of biological community development at nascent deep-sea hydrothermal vents (9°50'N, East Pacific Rise). Deep-Sea Research Part II, 45:465–515.

Sharp, T.G. and Buseck, P.R., 1993. The Distribution of Ag and Sb in Galena: Inclusions Versus Solid Solution. American Mineralogist. 78, 85–95.

Shima, M., Rees, C.E., and Thode, H.G., 1978. The isotopic composition and atomic weight of Palladium. Canadian Journal of Physics, 56, 1333-1339

Shock, E.L., and Holland, M.E., 2004. Geochemical energy sources that support the subsurface biosphere, In Wilcock, W., DeLong, E., Kelley, D., Baross, J., Cary, C. (Eds.) *The subseafloor biosphere at mid-ocean ridges*, Geophysical Monograph Series, vol. 144, pp. 153-165, AGU, Washington, DC.

Sleep, N.H., 1991, Hydrothermal circulation, anhydrite precipitation and thermal structure at ridge axes, Journal of Geophysical Research, 96, 2375–2387.

Smith, C.L., Rosman, K.J.R., and De Laeter, J.R., 1978. The isotopic composition of Tellurium. International Journal of Mass Spectrometry and Ion Physics, 28, 7-17.

Smith, R.N., and Huston, D.L., 1992, Distribution and association of selected trace elements at the Rosebery Deposit, Tasmania. Economic Geology, 87, 706-719.

Stein, C.A. and Stein, S., 1994. Constraints on hydrothermal heat flux through the oceanic lithosphere from global heat flow. Journal of Geophysical Research 99: 3081-3095.

Stewart, M. a., 2002. Geochemistry of dikes and lavas from the north wall of the Hess Deep Rift: Insights into the four-dimensional character of crustal construction at fast spreading mid-ocean ridges. J. Geophys. Res. 107, 2238. doi:10.1029/2001JB000545

Stoiber, R.E., 1940. Minor elements in sphalerite. Economic Geology, 35, 501-519.

Tao, C., Lin, J., Guo, Sh., Chen, Y.J., Wu, G., Han, X., German, C.R., Yoerger, D.R., Zhou, N., Li, H., Su, X., Zhu, J., and the DY111-19 (Legs 1-2) and DY115-20 (Legs 4-7) Science Parties, 2012. First active hydrothermal vents on an ultraslow spreading center: Southwest Indian Ridge. Geology 40 (1): 47-50.

Thomas, R.A., 2001. Beginner's Guide to ICP-MS. London, UK: CRC Press Inc, 38–42.

Tivey, M.K., Humphris, S.E., Thompson, G., Hannington, M.D., and Rona, P.A., 1995, Deducing patterns of fluid flow and mixing within the active TAG hydrothermal mound using mineralogical and geochemical data. Journal of Geophysical Research, 100, 12527-12555.

Trefry, J.H., Butterfield, D.B., Metz, S., Massoth, G.J., Trocine, R.P., and Feely, R.A., 1994, Trace metals in hydrothermal solutions from Cleft segment on the southern Juan de Fuca Ridge, Journal of Geophysical Research, 99, 4925-4935.

Tunnicliffe, V., 1991, The biology of hydrothermal vents: ecology and evolution, Oceanography and Marine Biology, An Annual Review, 29, 319-407.

Vandecasteele, C., Vanhoe, H, and Dams, R., 1993. Inductively coupled plasma mass spectrometry of biological samples. Invited lecture. Journal of Analytical Atomic Spectrometry, 8, 781-786. doi: 10.1039/JA9930800781.

Von Damm, K.L., 1983. Chemistry of submarine hydrothermal solutions at 21 °N, East Pacific Rise and Guaymas Basin, Gulf of California. Ph.D. dissertation, 240pp. Massachusetts Institution of Technology/Woods Hole Oceanography Institution. Joint Program in Oceanography.

Von Damm, K.L., 1990. Seafloor hydrothermal activity: black smoker chemistry and chimneys. Annu. Rev. Earth Planet. Sci. 18, 173–204.

Von Damm, K.L., 1995. Controls on the chemistry and temporal variability of seafloor hydrothermal fluids. In Humphris, S.E., Zierenberg, R.A., Mullineaux, L.S., and Thomson, R.E. (Eds.) *Seafloor Hydrothermal Systems: Physical, Chemical, Biological and Geological Interactions*, Geophysical Monograph Series, vol. 91, pp. 222–248. Washington, DC.

Von Damm, K.L., 2000, Chemistry of hydrothermal vent fluids from 9-10 N°, East Pacific Rise: "time zero", the immediate post-eruptive period, Journal of Geophysical Research 105: 11203-11222.

Von Damm, K.L., 2013. Controls on the Chemistry and Temporal Variability of Seafloor Hydrothermal Fluids, in: Seafloor Hydrothermal Systems: Physical, Chemical, Biological, and Geological Interactions. pp. 222–247. doi:10.1029/GM091p0222

Von Damm, K.L., Edmond, J.L., Grant, B., Measures, C.I., Walden, B., and Weiss, R.F., 1985. Chemistry of submarine hydrothermal solutions at 21 °N, East Pacific Rise. Geochimica et Cosmochimica Acta 49: 2197–2220.

Von Damm, K.L., Lilley, M.D., 2004. Diffuse flow hydrothermal fluids from 9°50'N East Pacific Rise: origin evolution and biogeochemical controls. In: Wilcock, W.S.D., Delong, E.F., Kelley, D.S., Baross, J.A., Cary, S.C. (Eds.), The Subseafloor Biosphere at Mid-Ocean Ridges. American Geophys. Union, Washington, DC, 243-266.

Wang, Z., and Becker, H., 2015. Abundances of Ag and Cu in mantle peridotites and the implications for the behavior of chalcophile elements in the mantle. Geochimica et Cosmochimica Acta, 160, 209-226.

Warren, H.V., and Thompson, R.M., 1945. Sphalerites from western Canada. Economic Geology, 40, 309-335.

Wheat, C.G., Mottl, M.J. and Rudnicki, M., 2002. Trace element and REE composition of a low-temperature ridge-flank hydrothermal spring. Geochimica et Cosmochimica Acta, 66: 3693-3705.

Wu, I., and Petersen, U., 1977, Geochemistry of tetrahedrite and mineral zoning at Casapalca, Peru. Economic Geology, 72, 993-1016.

Zierenberg, R.A., Shanks, W.C. III, and Bischoff, J.L., 1984, Massive sulfide deposits at 21°N, East Pacific Rise: Chemical composition, stable isotopes, and phase equilibria. Geological Society of America Bulletin, 95, 922-929.

Zoeller, K., 2014, Insights into the distribution and mobility of base metals in the sheeted dike complex formed at fast-spreading ridges (Pito Deep, EPR), M.Sc. thesis, University of Victoria.

Appendix A: Analysis Sequence for Standard Addition Method

The reference materials were analyzed in an order selected to minimize memory effects. A 2% HNO_3 solution was used to check the instrumental blank. A drift solution was analyzed during the analyses to monitor the drift in the instrument sensitivity. 2% HNO_3 and the drift solution were analyzed after every set of six spiked reference material solutions. The published concentrations of Mo in BCR-2 are about 250 ppm, which is much higher than the other six reference materials due to contamination of this reference material during its original preparation. To avoid a memory effect in the instrument, BCR-2 was analyzed at the end of the run along with the single element solutions. The analyses sequence is listed in Table A.1

Table A.1. Running Sequence for Standard Addition Method

Sequence	Sample	Sequence	Sample	Sequence	Sample
1	2% HNO_3 solution	…	…	86	2% HNO_3 solution
2	Drift	20	PBK2+5	87	Na-4900 ppb
3	Drift	21	2% HNO_3 solution	88	Na-10000 ppb
4	Drift	22	Drift	89	P-5000
5	2% HNO_3 solution	23	2% HNO_3 solution	90	P-10000 ppb
6	PBK1+0	24	AGV-1+0	91	K-4600 ppb
…	…	…	…	92	K-10000 ppb
11	PBK1+5	29	AGV-1+5	93	2% HNO_3 solution
12	2% HNO_3 solution	30	2% HNO_3 solution	94	Drift
13	Drift	31	Drift	95	2% HNO_3 solution
14	2% HNO_3 solution	32	2% HNO_3 solution	96	Co-20 ppb
15	PBK2+0	…	…	…	…

Note:
Drift is the drift solution prepared by mixing all the reference material solutions;
PBK is procedure blank solutions prepared by the same steps as preparing the reference materials, without any reference materials in;
Number 0 to 5 is the spike numbers of increasing concentration of the spike solution.

Appendix B: Analytical Raw Data and Data Reduction of Standard Addition Method

Standard addition method for determining the concentrations of As, Ag, Cd, Mo, Sn, and Tl in 7 reference materials (AGV-1, BIR-1, BHVO-2, JG-2, JGb-1, DNC-1, and BCR-2) can be found in electronic spreadsheet Appendix B. This appendix contains the raw count rate data and data reduction process.

Appendix C: Description of Samples and Reference Materials Preparation

Rock powder dissolution followed a method adapted from Eggins et al. (1997). The procedure is as follows:

1. Weight out ~0.1 g of each powdered sample (M_R) into a separate vial (to +/- 0.0001).

2. Add 5 mL of concentrated Environmental Grade HF and 0.5 mL of concentrated Environmental Grade HNO_3 using pipettes. Cap the vials tightly, and place on the hotplate at ~150 to ~180°C overnight, until samples are totally dissolved.

3. After the vials have cooled down, remove the lids and return them to the hotplate and evaporate the HF-HNO_3 mix until almost completely dry.

4. Add 4 mL of 8N Environmental Grade HNO_3, cap the vials and return to the hotplate at ~150°C overnight.

5. Remove vials from hotplate, and wait till the vials cool down. Remove the lids, and dry the solution until they are nearly dried down. Add 4 mL of 8N Environmental Grade HNO_3. Cap the vials and return to the hotplate at ~80°C overnight. Prepare labeled, pre-weighed (tare weight M_T), clean 125 mL high-density polyethylene (HDPE) bottles, and transfer the contents of each vial into separate bottles. Make up each to ~100 mL with 18.2 MΩ DI water. The acid concentration of the final solution is ~2%. Record the final weight (M_F) of the solution (to +/- 0.1 g). So the dilution factor is ~ 0.001.

Appendix D: Data Reduction Processes of the Pito Deep Samples

The process of data reduction of the Pito Deep samples in this study is described in the following steps.

Step 1: Internal standardization

The internal standard elements spiked online into all the analyzed solutions were ^{103}Rh, ^{115}In, and ^{185}Re. The raw signal for each internal standard has a smooth drift over the run. The elements of interest that were analyzed have an atomic mass range of 75-205. In this case, the choice of the internal standard was ^{115}In, for it is the most similar in mass to the elements of interest. Internal standardization removes the primary drift in the raw data. For each sample, the raw signals (counts per second) for the analyte elements i (CPS_{RAW}^{i}) is divided by the signals of internal standard element (^{115}In for this study) in that same sample (CPS_{RAW}^{In}), and times the signals of internal standard element in the first drift solution analyzed in the run (CPS_{DR}^{In}):

$$CPS_{In}^{i} = \left(\frac{CPS_{RAW}^{i}}{CPS_{RAW}^{In}}\right) CPS_{DR}^{In} \qquad \textit{Equation D.1}$$

Step 2: Blank correction

Blank correction allows us to estimate the contamination occurring during sample preparation. During the dissolution of the samples, the procedure blanks were prepared identically.

The signals of the blanks are constant and negligible (<< 1% of the lowest sample value). Thus the average of the corrected and normalized blank signal was subtracted from the samples analyses (Equation D.2),

$$CPS_{BLANK}^{i} = CPS_{In}^{i} - CPS_{APBK}^{i} \qquad \textit{Equation D.2}$$

where CPS_{BLANK}^{i} is the blank corrected signal for element i; CPS_{In}^{i} is the internal standard normalized corrected signal for element i; and CPS_{APBK}^{i} is the average signal for element i in the procedure blanks.

Step 3: Interference correction

For elements like As, Mo, Ag and Cd which have polyatomic interferences, the calculation of interference correction factor (INF) is described in Section 2.5.1. The interference corrected signal (CPS_{INF}^{i}) is:

$$CPS_{INF}^{i} = CPS_{BLANK}^{i} - INF \times CPS_{BLANK}^{int} \qquad \textit{Equation D.3}$$

where CPS_{BLANK}^{int} is the blank corrected signal of the interference source element of the target element (As, Mo, Ag and Cd) from analyzing the single element solutions.

Step 4: Dilution factor correction

The signals corrected by previous data reduction steps must be corrected for the variable masses of rock and HNO_3. Dilution factor for rock powders in HNO_3 solutions is:

$$\mathrm{DF} = M_r / M_f \qquad \textit{Equation D.4}$$

where M_r is the weight of rock sample, and M_f is the final weight of sample solution.

For element i in each sample, the dilution factor corrected signal (CPS_{DF}^{i}) is:

$$CPS_{DF}^{i} = CPS_{BLANK}^{i} / DF \qquad \textit{Equation D.5}$$

For elements like As, Mo, Ag and Cd that have been corrected for interferences,

the dilution factor corrected signal (CPS_{DF}^{i}) is:

$$CPS_{DF}^{i} = CPS_{INF}^{i}/DF \qquad \textit{Equation D.6}$$

Step 5: Secondary drift correction

As introduced in Section 2.2.3, a mixed sample solution is used as a drift monitor to correct for secondary drift. Secondary drift is the drift that not been corrected for by internal standardization.

For a drift that is linear, a best-fit line of the ratios of counts to the first drift solution counts (y=mx+c) was calculated, where y is the correction factor and x is the analysis number. Drift corrected signal (CPS_{SECD}^{i}) can be calculated as:

$$CPS_{SECD}^{i} = CPS_{DF}^{i}/y \qquad \textit{Equation D.7}$$

where y is the secondary drift correction factor. Alternatively, for non-linear drift the polynomial lines were used for calculating the secondary drift correction factor.

Step 6: Calibration

Reference materials (AGV-1, BCR-2, BIR-1, BHVO-2, DNC-1, JG-2, and JGb-1) are analyzed for calibration. For each element, use the reference materials to calculate linear fits of the signal corrected from previous steps (as x-axis) versus recommended value (or the value determined by standard addition method in this study; as y-axis). The linear fits of the calibration line should pass through the origin (y=mx). The coefficient m of element i times the signal corrected by previous steps (CPS_{SECD}^{i}) gives the concentration of element i in each sample.

Appendix E: Assessment of ICP-MS Data Accuracy

Accuracy of ICP-MS data was assessed by comparing with the published data of the same samples, which were also analyzed by ICP-MS method from previous studies. The comparison includes the concentrations of elements Zn, Cu, Yb, and Pb (Fig. E.1) from Pollock et al. (2009), Barker et al. (2008), Heft et al. (2008), and Barker et al. (2010a). The intercepts of the best-fit lines are set to origin, and the equations are displayed as follow:

$$y = ax \qquad \textit{Equation E.1}$$

if a $>$ 1, it means the data of this study is higher than the previous study; if a $<$ 1, it means the data from this study is lower than the previous study. The R-squared value represents how close the data are to the fit line, that is that the closer the number to 1 the better the data fit to the regression line. Over 90% of the analyses of Zn and Yb lie within 20% deviation from the best-fit lines; over 80% of the analyses of Cu lie within 20% deviation from the best fit lines (except for the data from Pollock et al., 2009); over 90% of the analyses of Pb lie within 10% deviation from the best fit line of Barker et al. (2010a), but the data from Pollock et al. (2009) and Heft et al. (2008) are not consistent with the data of this study. Overall, the data published by Barker et al. (2010a) is more consistent with the data from this study.

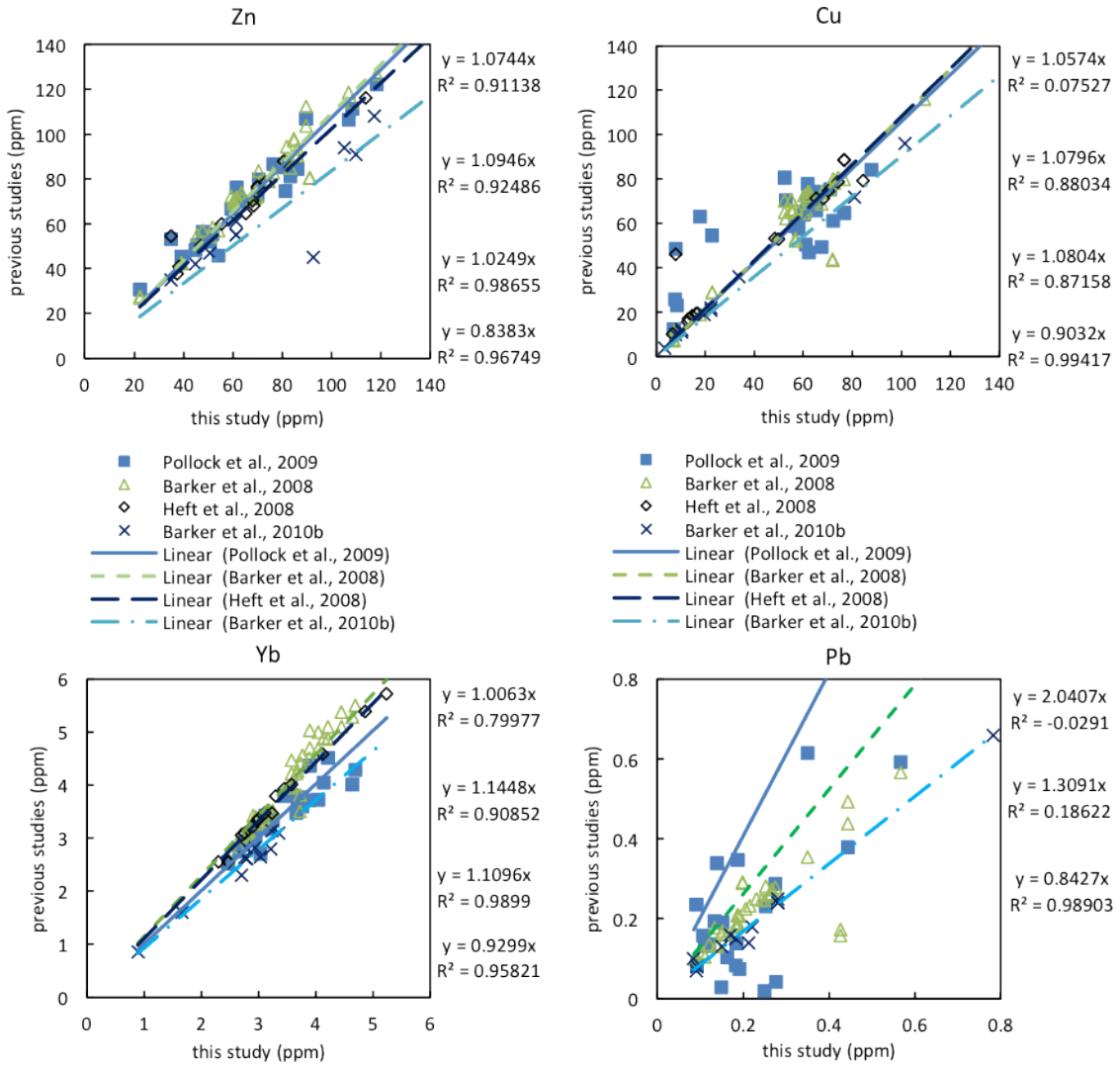

Figure E.1. The assessment of data accuracy by comparing with previous studies. The best fit-line equations are in the sequence of Pollock et al. (2009), Barker et al. (2008), Heft et al. (2008), and Barker et al. (2010a). Heft et al. (2008) did not have data of Pb concentration.

Appendix F: Analytical Results of Pito Deep Samples and Previous Data on Other Fast-Spreading Ridges

Raw data and data reduction process of the trace element concentrations for 52 whole rock samples from Pito Deep can be found in electronic spreadsheet Appendix F. This appendix also contains data from previous studies on the Pito Deep (Heft et al., 2008; Barker et al., 2008; Barker et al., 2010a and 2010b), as well as the data on other areas at fast-spreading ridges, Hole 504B (Bach et al., 2003; Emmermann, 1983; Alt and Emmermann, 1985; Alt et al., 1989), Hess Deep (Stewart et al., 2002; and Gillis et al., 2001), and Hole 1256D (Gao et al., 2009; and Cooper, 2007).